Sedimentation behaviour of a ferro-metal slag for the conceptual design of a CCD process

D Matthee

orcid.org/ 0009-0001-4979-8207

Dissertation accepted in fulfilment of the requirements for the degree *Master of Engineering in Chemical Engineering* at the North-West University

Supervisor:	Prof QP Campbell
Co-supervisor:	Prof M le Roux
Co-supervisor:	Mr DJ van der Westhuizen

Graduation: May 2026

PREFACE

Declaration of authorship

I, Daniel Matthee, declare that this is my own work and all sources used are properly acknowledged. I declare that this work has not been submitted to this or any other institution.

D Matthee

Signed on the 28th day of November 2025

Declaration of the use of artificial intelligence

I**,** Daniel Matthee**,** declare that this dissertation is my own work. Artificial intelligence tools (ChatGPT, Gemini and Grammarly) were used only for language editing and improving readability. The author conducted all research design, analysis, and interpretation under supervision.

D Matthee

Signed on the 28th day of November 2025

Conference papers and presentations

D. Matthee, Q.P. Campbell, D. van der Westhuizen, M. le Roux, “Sedimentation behaviour of an oxide slag for the conceptual design of a CCD process,” submitted for presentation and publication at the International Mineral Processing Conference, 2026.

Acknowledgements

I would firstly like to thank my Heavenly Father for granting me the strength, wisdom, and perseverance to complete this work successfully.

Secondly, I would like to express my sincere gratitude to my supervisors, Prof. Q.P. Campbell, Mr D. van der Westhuizen, and Prof. M. le Roux, for their invaluable guidance, encouragement, and continuous support throughout the course of this study.

I would also like to thank Ms René Becker and Mr Sean Mashimbyi for their assistance in the laboratory. In addition, I would like to thank Mr Marcus Keulder for providing valuable insights into the leaching procedures and Ms Nompumelelo Maduna for her continuous help with elemental analysis techniques.

Furthermore, I wish to acknowledge the North-West School of Chemical and Minerals Engineering, RFA: Chemical Resource Beneficiation (CRB) and Tharisa Minerals for their support and contributions towards this Master's research.

Lastly, I would like to express my heartfelt appreciation to my parents for their unwavering love, patience, and encouragement throughout my studies.

ABSTRACT

The need for sustainable waste management and the rising global demand for raw materials have necessitated the recovery of valuable metals from metallurgical by-products such as ferrous metal oxide slag. These slags contain substantial amounts of the base metal from which they originate and trace quantities of valuable metals. The effective use of hydrometallurgical processes, such as leaching, depends not only on the leach recovery but also on the solid-liquid separation and washing steps that follow. These steps must be efficient to maximise lixiviant recovery and reduce loss due to entrainment.

Challenges in settling the leach residue arise from slurry properties such as solution viscosity and surface chemistry. Furthermore, in a continuous countercurrent decantation (CCD) process, sedimentation occurs under continuously changing conditions, including particle size distribution, solution viscosity, and solid-liquid ratio. To design a CCD system, the influence of these conditions on the solids settling flux must be understood and quantified. This project explores the sedimentation behaviour of a ferrous metal oxide slag during various simultaneous settling and leaching stages for the conceptual design of a CCD demonstration process. Key objectives included fully characterising the ferrous metal oxide slag, identifying an appropriate flocculant and dosage to improve settling rate, simulating the settling conditions of a CCD and conceptually sizing a CCD demonstration process.

The ferrous metal oxide slag was first characterised, using XRD to identify the crystal structure, SEM-EDX to analyse surface elemental composition and morphology, XRF and microwave digestion combined with ICP-OES to assess the bulk elemental composition, and laser diffraction to measure particle size distribution. Then, a flocculant study was conducted to determine the flocculant type and dosage needed to improve settling of the leached slurry. Finally, a laboratory-scale simulation of the CCD process was performed, involving a primary leaching step followed by a series of interconnected batch settling tests designed to mimic the conditions during a continuous washing process. The lixiviant at each stage was analysed to determine the recovery of the target metals.

The results identified an effective flocculant capable of functioning in harsh acidic conditions. The simulation demonstrated that the three-stage CCD performed well as a washing step, achieving 84% washing recovery at a solid-liquid ratio of 10 wt% and 98% at 5 wt%. However, as a secondary leaching process, the CCD showed limited ability to recover additional target metals. Analysis revealed that this step removed residual surface materials and leached considerable amounts of non-target elements, including silicon, aluminium, and calcium. As a secondary leaching stage, the CCD only recovered an additional 3.62% at a solid-liquid ratio of 10 wt% and

1.35% at 5 wt%. The settling fluxes determined in the laboratory-scale simulation of the CCD process were successfully used to size a CCD demonstration process.

Keywords: *Ferrous metal oxide slag, Hydrometallurgy; Leaching; Continuous countercurrent decantation; Solid-liquid separation; Flocculant; Metal recovery; Sedimentation.*

TABLE OF CONTENTS

LIST OF TABLES

LIST OF FIGURES

LIST OF ABBREVIATIONS

ASTM	American Society for Testing and Materials
CCD	Continuous countercurrent decantation
EDX	Energy dispersive X-ray spectroscopy
FMO	Ferrous metal oxide
ICDD	International Centre for Diffraction Data
ICP-OES	Inductive Coupled Plasma Optical Emission Spectroscopy
ISO	International Organisation for Standardisation
LOI	Loss on ignition
PLS	Pregnant leach solution
PSD	Particle size distribution
SAG	Semi-autogenous grinding
SEM	Scanning electron microscopy
XRD	X-ray diffraction
XRF	X-ray fluorescence

NOMENCLATURE

v_t	terminal velocity of the particle, m/s
ρ_p	density of the particle, kg/m^3
ρ_f	density of the fluid, kg/m^3
g	gravitational acceleration, m/s^2
d	diameter of the particle, m
μ	viscosity of the fluid, $Pa.s$
v	hindered settling velocity, m/s
v_0	single particle settling velocity, m/s
$\emptyset$	solid volume fraction
n	exponent dependent on flow regime
G_s	solid flux, kg/m^2s
C	solid concentration, kg/m^3
$v(C)$	settling velocity, m/s
ΔH	change in height, m
Δt	change in time, s
C_0	initial solid concentration, kg/m^3
H	current interface height, m
H_0	initial interface height, m
$F(C)$	flux at concentration C, kg/m^2h
C_{max}	maximum solid concentration, kg/m^3
K	proportionality constant, kg/m^2h
m	fitting exponent
A	unit area, m^2/tpd
C_0	initial solid concentration, kg/L
C_u	underflow solid concentration, kg/L
v_0	initial settling rate, m/d

t_u	settling time, $days$
R	fraction of dissolved value in the feed which is recovered in the overflow liquor of the first thickener
O	overflow liquor volume per unit weight of underflow solids
U	underflow liquor volume per unit weight of underflow solids
N	number of stages

Chapter 1: Introduction

This chapter introduces the background and motivation for the research, outlining the study's aim, objectives, and scope.

1.1 Background and motivation

Ferrous metal oxide (FMO) slag, a by-product of smelting processes, often contains valuable metals that can be extracted using leaching methods. Although heap leaching is a common approach due to its simplicity and the absence of solid-liquid separation requirements, it is often inefficient and slow, prompting researchers to explore alternative methods [1]. Continuous leaching and solid-liquid separation through settling, such as continuous countercurrent decantation (CCD), have been considered more effective options [2] [3]. Despite heap leaching's potential, its drawbacks, including lower metal recovery rates and longer processing times than methods that require solid-liquid separation, such as tank, agitated, and vat leaching, highlighting the need for more efficient techniques [1]. In Table 1, heap leaching is compared to other leaching methods that also require solid-liquid separation [4].

Table 1: Comparison of traditional leaching methods concerning leach time and metal recovery [4]

Leaching method	Leaching time	Metal recovery
Heap leaching	Months to years	Low
Tank leaching	Minutes to hours	Moderate
Agitated leaching	Minutes to hours	Moderate to high
Vat leaching	Days	Moderate

In leaching methods that require solid-liquid separation, the slurry produced is typically sent to a thickener [3]. One issue with this approach is that the solids discharged from the thickener still contain a significant amount of lixiviant, which holds valuable dissolved metals [2]. To recover these metals, a washing step can be added. This step removes the excess lixiviant, allowing it to be further processed, while the washed solids can be safely discarded without causing environmental harm. Additionally, washing improves overall metal recovery by diluting the PLS, with CCD being a standard method used for this purpose [2].

In each CCD stage, the washing liquid and slurry enter the feed well of a sedimentation thickener, and the slurry is washed. During this process, the solid particulates settle to the bottom of the vessel while the solution rises to the top [5]. Thickeners with conical-bottom stirring rakes are used to enhance solid-liquid interaction. The settled pulp is pumped to an upstream stage of the CCD, and the clarified solution is pumped to a downstream stage [5]. In the last CCD stage, fresh washing liquid, which has not passed through any CCD stages and thus has the highest acid concentration, meets partially depleted ore, which has already passed through all the previous CCD stages. On the opposite end of the cascade, in the first CCD stage, partially depleted washing liquid, which has passed through all the CCD stages, is contacted with the fresh ore feed. In the intermediate CCD stages, some degree of partially depleted ore and partially depleted washing liquid meet. Implementing a countercurrent flow of ore and washing liquid results in a concentration gradient. This concentration gradient acts as a driving force, ensuring efficient pulp washing. It is possible to add as many stages as necessary to improve the washing efficiency [5].

Two standard methods for improving metal recovery include multi-stage leaching and CCD systems. [6] [3]. In a multi-stage leaching process, the pulp from one leaching stage is sent to additional stages where fresh lixiviant is added. This continues until the desired recovery is achieved [6]. In the CCD system, acid is added to the washing liquid, turning the process into a combined washing and leaching step. Increasing the number of CCD stages can help improve leaching efficiency and reach the targeted recovery [2] [3]. A comparison between multi-stage leaching and CCD systems is drawn in Table 2.

Table 2: CCD systems vs multi-stage leaching [2] [6]

Factor	CCD systems	Multi-stage leaching
Extraction Efficiency	Higher (85–99%)	Moderate to High (75–90%)
Capital Cost	Higher	Lower
Operational Cost	Moderate	Higher (due to reagent use)
Water/Reagent Use	More efficient (low loss)	Higher consumption

Between these two methods, a CCD system is preferred due to its higher extraction efficiency and lower operating costs. This project will investigate the efficiency of a CCD system to determine whether a traditional leach combined with a CCD system is sufficient in recovering the

required metals. Alternatively, although capital-intensive, both the multistage leach and a CCD system can be employed.

To design a CCD circuit, it is necessary to thoroughly understand the sedimentation properties of the slag [3] [7]. The motivation of this project is to determine the sedimentation characteristics of the FMO slag and to design and construct a laboratory-scale CCD system to leach certain metals from the FMO slag. The sizing of a CCD thickener requires quantifying the necessary settling flux of the material under different conditions [3] [7]. These conditions include particle size distribution, solid-liquid ratio, and fluid viscosity, which will be determined in this project.

1.2 Problem statement, aim and objectives

1.2.1 Problem statement

Little is known about the settling characteristics of this particular ferrous metal oxide slag, especially in viscous acid solutions. Additionally, in a CCD process, sedimentation steps occur with continuously changing conditions, including particle size distribution, solution viscosity, and solid-liquid ratio. The effect of these conditions on the solid settling flux is investigated so that it can be understood and quantified for the design of a CCD system.

1.2.2 Aim

The aim of this study is to investigate the sedimentation behaviour of a ferrous metal oxide slag for the conceptual design of a CCD demonstration plant.

1.2.3 Objectives

- To study the settling behaviour of intermediate leached solids in intermediate-loaded lixiviants, simulating various inter-stage settling conditions;
- To determine the ideal conditions for simultaneous sedimentation and leaching of the slag (lixiviant acid concentrations, particle size distribution and solid-liquid ratio);
- To conceptually design a demonstration model CCD process.

1.3 Work-plan section

This section summarises the project work-plan:

- To conduct a literature survey on sedimentation, thickeners, parameter determination and simulation;

- To conduct a literature survey on the design of CCD systems from settling and leaching kinetic data;
- To perform the preparatory processing of an industry-sourced ferrous metal oxide slag, like crushing, milling and magnetic separation;
- To characterise slag feed material;
- To prepare sufficient solids and lixiviant samples, some of which are partially leached for subsequent tests;

1.4 Scope

This study focuses on the characterisation, leaching behaviour, and sedimentation performance of an industry-sourced FMO slag to develop a conceptual design for a three-stage CCD process. The work begins with characterisation of the slag using XRD, SEM-EDX, XRF, and ICP-OES analyses to determine its mineralogical composition, surface morphology, and elemental distribution. The effect of leaching at various conditions is tested to determine its impact on settling and metal recovery. A flocculant screening and optimisation study is performed to identify a suitable polymer and dosage for stable settling in acidic conditions. Batch settling and simulated CCD experiments are then conducted to evaluate the sedimentation behaviour, settling flux, and washing efficiency of the slag at different solid loadings. The data obtained from these experiments are used to design a conceptual CCD system, including a process flow diagram, mass balances for each stage, and a preliminary thickener sizing based on the Wilhelm–Naide method. The design represents a demonstration-scale process at an estimated feed rate of 100 $kg \cdot h^{-1}$.

1.4.1 Limitations of this study

This study will be limited to laboratory-scale sedimentation testing and conceptual process design. The smelting process, leaching, leaching kinetics, continuous pilot-scale operation, downstream hydrometallurgical recovery, and long-term environmental evaluation of residues fall outside the scope of this research.

1.5 Report Outline

This report is divided into six chapters: Introduction, Literature Review, Materials and Methods, Results and Discussion, Conclusion and Recommendations. The introduction gives an overview of the project, including the background, motivation, aims, and objectives. The literature review

provides further information and discussion on the key topics in the report, including sedimentation, thickeners, CCD, particle breaking, leaching, flocculation, and process modelling. The methods and materials section provides a more comprehensive description of the provided slag and the experimental design, including the particle-breaking procedure, flocculant tests, determination of the ideal weight percentage, production of intermediate leached slag and intermediate loaded lixiviates, and CCD sedimentation. The results and discussion present the findings on the characterisation of the material, leaching tests, flocculant tests, determination of ideal settling conditions, and theoretical size determination of the CCD system. The conclusion summarises and evaluates the main results of this study. Further, the last chapter provides recommendations for future studies on CCD systems using FMO slag.

Chapter 2: Literature review

The following section examines slags, covering their definition, origin, types, and uses. The section is followed by an explanation of the basics of settling and how particle properties influence separation, followed by an overview of leaching techniques and their dependence on solid-liquid separation. The discussion includes the role and design of thickeners, as well as the use of flocculants to enhance settling. The principle of CCD is also introduced, illustrating how these concepts are applied to design a CCD system for the FMO slag conceptually.

2.1 Slag

Slag is a waste product generated during the smelting of metallic ore [8]. It is removed from the top of the furnace as either molten or solid residue. It is estimated that more than 400 Mt of slag are produced annually worldwide, and this quantity is increasing steadily [8]. Approximately 0.25–0.3 tonnes of slag are produced per tonne of crude or pig iron, 0.6 tonnes per tonne of lead, and 2.2 tonnes per tonne of copper [9] [10] [11]. The environmental behaviour and potential reuses of slag are studied.

2.1.1 Smelting

Smelting is the high-temperature phase in the pyrometallurgical extraction of metals. The primary purpose of smelting is to separate the ore into valuable metals and gangue minerals and impurities [12]. This process exploits the components' reactivity and density differences at high temperatures [8] [12].

During the smelting process, the ore is heated to a molten state in the presence of fluxes, reducing agents, and sometimes oxidising gases [13] [14] [15]. Fluxes such as limestone, dolomite, and silicon oxide are added to react with the gangue components in the slag, forming oxides or silicates. These reactions help remove impurities from the molten metal and produce slag [8] [13]. Reducing agents such as carbon are added to reduce metal oxides to their metallic form [14]. The reduction reaction is shown:

$$MO + C \rightarrow M + CO \qquad \text{(R-1)}$$

where MO is a metal oxide, and M represents the metal.

Oxidising gases such as air or oxygen are sometimes added to smelting when processing sulphide ores. The gas oxidises any sulphides to oxides before the reducing process [15]. The oxidation reaction is shown:

$$MS + O_2 \rightarrow MO + SO_2 \quad \text{(R-2)}$$

where MS is a metal sulphide and MO is the metal oxide.

Slag mainly consists of silicate and oxide by-products formed during high-temperature processes; its composition varies depending on the feed material, smelting conditions, and added fluxes [8] [16]. This section further details the different types of slag and recycling methods.

2.1.2 Slag properties

Slag is classified into two main categories, ferrous and non-ferrous, depending on the metal production process from which it originates [8]. The slag's properties are also influenced by the cooling method used [17].

2.1.2.1 Ferrous slag

Ferrous slag is produced as a by-product during the recovery and smelting of ores and recycled materials in the production of iron, steel and ferrous alloys [8]. In iron manufacturing, iron ore is added to the blast furnace and melted. The iron oxides are reduced to iron by adding fluxes such as limestone or dolomite, along with a fuel and a reductant such as coke [8]. Molten iron ore is combined with alloys in steel manufacturing to produce the desired steel grade. The steel-making process also generates a slag by-product [17]. In producing ferrous alloys like ferrous-chrome, ferrous-silicon, and ferrous-manganese, the same fluxes, fuel, and reductants as iron are used [18].

Ferrous slag can be cooled using various methods depending on its intended application. These include slow cooling under atmospheric conditions, moderate cooling with controlled amounts of water, quick cooling in air, and quenching with high-volume, high-pressure sprays of water [19]. The different ferrous slag cooling methods and their impact on slag properties and commercial uses are summarised in Table 3.

Table 3: Ferrous slag cooling methods and their effect on slag properties and commercial use [8] [18] [19]

Cooling method	Resulting slag type	Physical characteristics	Commercial use
Slow-cooled under atmospheric conditions	Air-cooled slag	Crystalline and vesicular (dense and hard)	Construction aggregate
Moderate cooling with controlled amounts of water	Expanded or foamed slag	Porous crystalline and glassy material	Lightweight aggregate
Quick cooling with water	Pelletised slag	Glassy and crystalline pellets	Lightweight aggregate or cementitious material
Quenching with high-volume, high-pressure sprays of water	Granulated slag	Vitrified granules (cementitious properties)	Cementitious material

2.1.2.2 Non-ferrous slag

Non-ferrous slag is produced as a by-product during the smelting of non-ferrous ores when extracting non-ferrous metals [20]. Common non-ferrous sulphide ores include copper, nickel, and lead [21]. During the smelting process, the oxides are reduced using various fluxes, such as silicon oxide, limestone, or iron, along with a fuel and a reductant, such as coke [8].

Non-ferrous slags have fewer commercial uses compared to their ferrous slag counterparts. As a result, these slags are often cooled slowly under atmospheric conditions, forming a crystalline porous material. Quenching is a less common method, which produces a glassy product [8].

2.1.3 Slag environmental impact, uses and recycling

The reuse of slag depends on its chemical composition and mineralogical structure. When slag is stored in tailings piles, it undergoes weathering, leaching, and oxidation, which release metals and influence the pH of water and soil [8]. Therefore, the environmental impact and potential uses of these slags are investigated.

Ferrous slags contain significant amounts of calcium and silicon and tend to produce alkaline leachates [22]. The alkaline nature of these slags enables their use in various environmental applications such as acid mine drainage treatment, phosphate removal, and wastewater treatment [23] [24] [25]. Ferrous slags are also broadly utilised in construction, for example, as additives in cement and concrete, and as aggregates in road construction [26] [27] [28].

Non-ferrous slags contain sulphides and heavy metal oxides, which can produce acidic leachates. These slags may therefore cause the mobilisation of toxic metals during weathering [8]. Non-ferrous slag also includes large amounts of base metals that can be recovered. These base metals are retrieved by reprocessing the slag through secondary smelting or hydrometallurgical leaching, transforming the waste material into a valuable resource [29] [30]. A summary of the main constituents, environmental behaviour, and reuse potential of both slag types is provided in Table 4.

Table 4: Environmental aspects of ferrous and non-ferrous slag [26] [28] [29] [30]

Slag type	Main constituents	Environmental behaviour	Reuse potential
Ferrous slag	Ca, Si, Al and Mg	Acid neutralisation capabilities Does not release significant amounts of trace elements	Construction, environmental applications and secondary metal recovery
Non-ferrous slag	Si, Fe, Al and Ca	May generate acid Releases trace elements when weathered	Secondary metal recovery and waste pile

2.2 Sedimentation

Sedimentation is the process by which particles settle out of a fluid, forming a solid bed, due to gravity, resulting in the separation of solids from liquids [31] [7]. Several key elements influence sedimentation behaviour: particle shape, solid concentration, particle size, density differences, the impact of additives or chemicals, temperature, rheology, and pH [32]. This section discusses single particle settling, hindered settling, experimental collection of settling data, interpretation of settling data, and factors affecting settling.

2.2.1 Single particle settling

The theoretical foundation of solid-liquid separation stems from the concept of a single solid particle settling in a liquid suspension. Under these conditions, the particle is not influenced by the presence of other particles or the container wall [33]. The movement of a settling body is affected by only three forces: gravitational, buoyant, and drag force [34]. Gravitational force is the downward force acting on the particle due to gravity and is proportional to its mass. Buoyant force is the upward force exerted by the fluid on the particle and equals the weight of the fluid displaced [34]. The drag force is the force opposing a particle's motion due to fluid resistance. The forces on a solid body are shown in Figure 1.

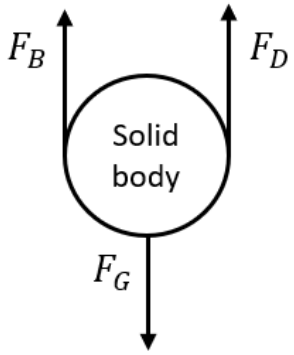

Figure 1: Forces on a body

Stokes' law describes the movement of a perfectly spherical particle at a low Reynolds number (Re < 0.3) [33] [34]. The Reynolds number is the ratio between the inertial and viscous forces. At low Reynolds numbers, particles are small, move at low velocities, and the fluid around the particle flows laminarly [35]. Under these conditions, the particle's drag force is directly proportional to the particle's velocity and diameter. Stokes' law quantifies this relationship by defining the terminal velocity as:

$$v_t = \frac{(\rho_p - \rho_f) g d^2}{18\mu} \quad (1)$$

Where,

v_t = terminal velocity of the particle, m/s

ρ_p = density of the particle, kg/m^3

ρ_f = density of the fluid, kg/m^3

g = gravitational acceleration, m/s^2

d = diameter of the particle, m

μ = viscosity of the fluid, $Pa.s$

Stokes' law relies on several idealised assumptions [33]:

- No interaction between particles
- Perfectly spherical particles
- Constant fluid properties (density and viscosity)
- Fluid that is infinite, still, and unbounded by walls

The assumptions made for Stokes' law in real-world slurry systems are not entirely accurate. Particle-particle interactions lead to a decrease in settling velocity, a phenomenon known as hindered settling [36] [37]. Hindered settling will be discussed further in section 2.1.2. In real slurries, the particles are also non-spherical and vary in particle size. Slurries' properties, including density and viscosity, also inherently change in a settling system [37]. During the settling of a slurry, solids settle to the bottom, thus causing a decrease in density and viscosity at the top of the slurry and an increase in density and viscosity at the bottom.

Although Stokes' law has limitations, it still provides an essential theoretical foundation. It establishes a relationship between particle characteristics (size and density) and fluid properties (viscosity and density). Single particle settling theory thus forms the link between particle size, density differences, and fluid viscosity, forming a basis for more complex settling phenomena such as hindered settling [37].

2.2.2 Hindered and zone settling

Real-world slurries have high solid concentrations, which cause hindered settling. Hindered settling occurs when particles are so close that they block each other's movement, leading the suspension to settle as a whole rather than individually [36] [38]. Unlike free settling, which involves minimal interaction, hindered settling involves strong hydrodynamic interactions between neighbouring particles. In free settling, only the drag force from relative motion through the fluid acts [36]. As a result, the collective settling velocity of the slurry is much lower than the terminal velocity predicted by Stokes' law for an isolated particle. Richard and Zaki (1954) first quantified hindered settling with the empirical relationship [38]:

$$v = v_0(1 - \emptyset)^n \quad (2)$$

Where,

v = hindered settling velocity, m/s

v_0 = single particle settling velocity, m/s

$\emptyset$ = solid volume fraction

n = exponent dependent on flow regime

Zone settling is hindered settling, in which all particles, regardless of size and density differences, settle at nearly the same velocity [36] [39]. Zone settling occurs when the slurry has a high particle concentration or when flocculants are used. This behaviour was described by Kynch (1952), who related solid flux to solid concentration and settling velocity [39]. His theory provided the basis for interpreting batch settling tests and estimating the limiting flux conditions critical for thickener design [39].

$$G_s = Cv(C) \quad (3)$$

Where,

G_s = solid flux, kg/m^2s

C = solid concentration, kg/m^3

$v(C)$ = settling velocity, m/s

2.2.3 Experimental collection of settling data

Thickener sizing typically begins with the analysis of settling data to determine critical parameters. Settling data is interpreted using a wide range of mathematical methods, theories, and models to determine the thickener's area and depth [40]. These include the Coe and Clevenger method, the Kynch theory, the Talmage and Fitch method, the Wilhelm-Naide model, and the Yosioka and Hassett model [40]. Settling tests are conducted on pulp samples with varying solids concentrations, enabling the calculation of settling rates and area values [32] [40].

There are three basic approaches for testing sedimentation properties [32] [7]:

1. Continuous Piloting: This method employs a scaled-down version of the equipment, such as a small-diameter thickener or clarifier, in conjunction with the full-scale equipment configuration. By running this pilot setup continuously, its performance can be monitored over time.

2. Semi-Continuous Bench Scale Tests: This method involves using laboratory pumps to feed slurry and flocculant solution into settling cylinders. These cylinders continually collect overflow liquor and underflow slurry, providing a more controlled testing environment than continuous piloting.

3. Batch Bench Scale Settling Tests: The traditional method entails placing a sample into graduated cylinders and allowing it to settle. This method uses a relatively small amount of sample material and is an inexpensive method of evaluating sedimentation characteristics. However, scaling up from batch testing necessitates consideration of several factors, including application experience and proven scale-up methods.

Factors such as sample size can have an impact on the testing scale used. Batch bench-scale tests are appropriate for smaller sample amounts, whereas semi-continuous bench-scale and pilot tests require larger sample volumes [32]. The costs of tests differ, with continuous piloting tests being the most expensive, followed by semi-continuous bench scale tests, and batch bench scale settling being the least costly [32]. Accuracy is critical, and while bench-scale testing provides acceptable accuracy, scale-up factors are still necessary, especially in uncertain applications where pilot-scale testing may be required. Furthermore, observing clear overflow or heavy underflow from pilot equipment that resembles the full-scale design reduces ambiguity [31] [32].

2.2.4 Interpreting settling test data

The Coe & Clevenger (1916) method is one of the original techniques used to determine the settling rate of a slurry necessary to calculate the thickener area [41]. This method involves conducting a series of batch settling tests with varying initial solid concentrations. In each test, the slurry-liquid interface is measured, and the data is used to produce a height versus time graph, which helps to determine the settling rate and the required thickener area [40] [41]. Kynch (1952) then developed a theoretical model that links the batch settling curve to a solid flux function [39]. This approach assumes that the slurry's local settling velocity depends only on the local solid concentration [39] [40]. The Kynch method enables users to conduct a single batch settling test, conserving time and sample material. However, several assumptions are made [39]:

- The settling velocity only depends on the solid concentration
- The slurry has a uniform solid concentration below the slurry-liquid interface
- Negligible wall effects

If these assumptions fail, the interpretation becomes less accurate.

2.2.4.1 Height vs time

The height-time curve construction used by both Coe & Clevenger (1916) and Kynch (1952) is illustrated in Figure 2. The batch settling test involves adding slurry to a settling column, ensuring a uniform solid distribution, and allowing the solid particles to settle under gravity [41]. The graph is created by noting the slurry-liquid interface at various intervals and plotting the collected data [41]. These graphs are used to determine the initial settling rate, when hindered settling transitions into compression, and to gather solid flux data [39] [40] [41].

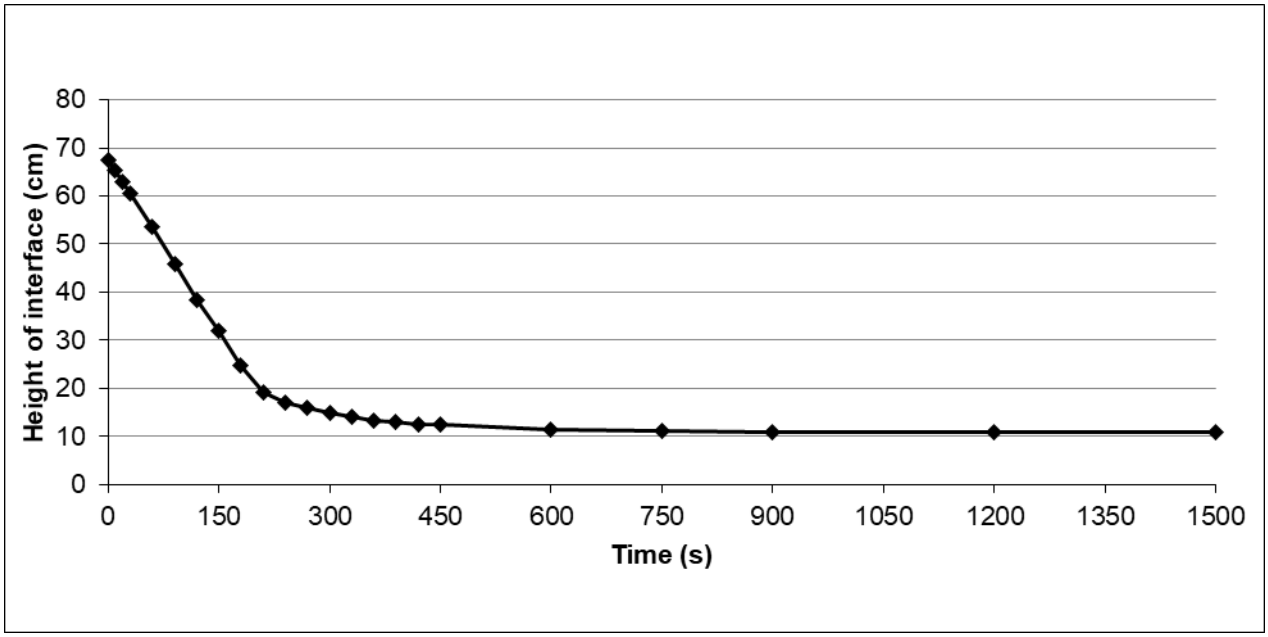

Figure 2: Height vs time graph [39]

2.2.4.2 Flux vs concentration

Kynch (1952) further explained how to construct a flux-concentration curve from the data collected in the height-time curve [39]. The settling velocity for any time interval can be obtained from the slope of the height-time relationship and is expressed as:

$$v = \frac{\Delta H}{\Delta t} \tag{4}$$

Where,

v = settling velocity, m/s

ΔH = change in height, m

Δt = change in time, s

The solid concentration within the settling zone can be determined by performing a mass balance between the initial and current slurry heights over the interval [39]. This relationship is expressed as:

$$C = C_0 \frac{H_0}{H} \tag{5}$$

Where,

C = current solid concentration, kg/m^3

C_0 = initial solid concentration, kg/m^3

H = current interface height, m

H_0 = initial interface height, m

The solid flux can be calculated by multiplying the local settling velocity by the solid concentration within an interval, as Kynch (1952) described in equation 3. The solid flux and concentration over a series of time intervals can be used to construct a flux-concentration curve [39] [40].

2.2.4.3 Model fitting

A mathematical model is fitted to the flux-concentration curve to improve accuracy when working with this data. The model is an empirical flux function inspired by phenomenological approaches such as those of Bustos & Concha (1999). It was developed to characterise the hindered settling and compression settling regimes in batch settling tests using a flocculant [42] [43]. The model describes the relationship between solid flux and concentration as:

$$F(C) = K(\frac{C}{C_{max}})(1 - \frac{C}{C_{max}})^m \tag{6}$$

Where,

$F(C)$ = flux at concentration C, kg/m^2h

C_{max} = maximum solid concentration, kg/m^3

K = proportionality constant, kg/m^2h

m = fitting exponent

The model is presented using a general example as illustrated in Figure 3. This model shows the characteristic increase in flux as the concentration rises from zero, followed by a decline at higher concentrations where hindered settling occurs. The model is used to simplify the calculation of a limiting flux required for thickener design.

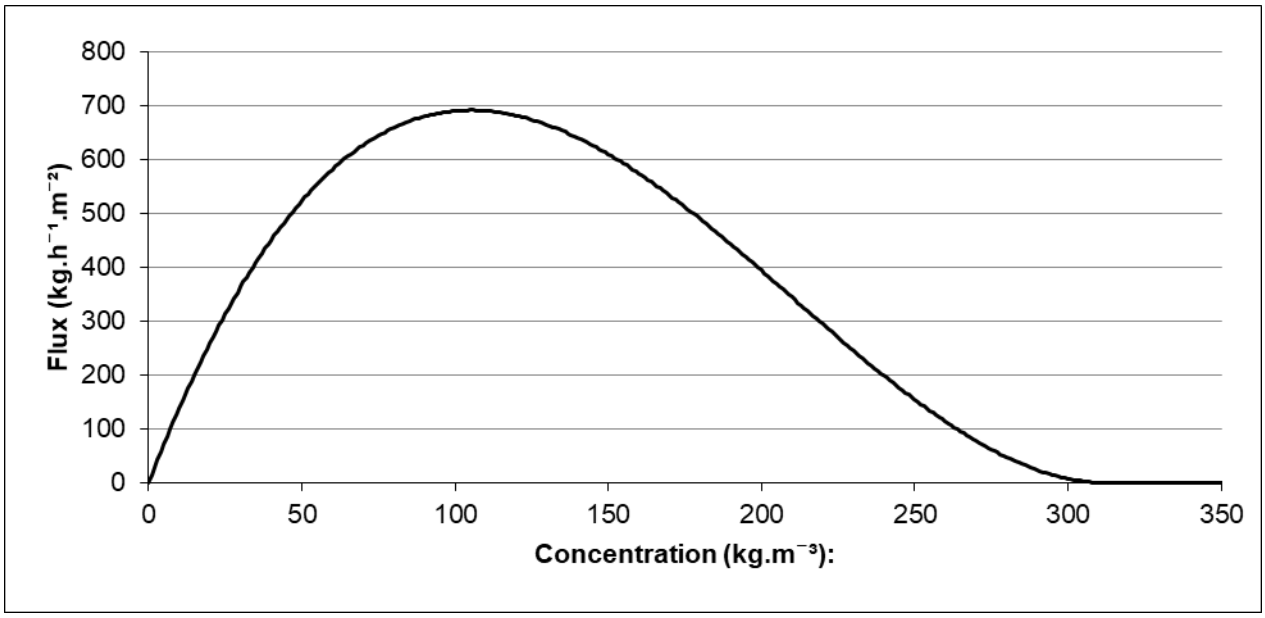

Figure 3: Flux vs concentration graph with the model fitted [40]

2.2.5 Factors influencing settling behaviour

Firstly, the particle size distribution within the slag determines the sedimentation kinetics, with larger particles settling faster than smaller ones due to their greater mass, leading to stratification inside settling tanks [32]. Secondly, sedimentation depends on density differences between solid particles and the surrounding liquid, which is influenced by chemical composition variations [32]. Furthermore, the addition of additives or chemicals, such as flocculants and coagulants, can alter sedimentation behaviour by promoting particle aggregation, thereby increasing settling rates and separation efficiency [44]. Temperature changes affect slurry viscosity, which in turn influences sedimentation rates, but the slurry's rheological properties, such as flow behaviour and deformation resistance, also influence sedimentation behaviour. The shape of the particles affects

how they settle. Particles with long, irregular, or spherical shapes settle more slowly, while particles with irregular shapes may face more resistance during sedimentation [32]. Furthermore, the concentration of solids in the slurry and the pH of the solution are important considerations, with higher solid concentrations and pH fluctuations influencing sedimentation rates via impacts on particle aggregation and settling behaviour. The large number of variables affecting the settling behaviour of a slurry supports the need for experimental work to determine the design parameters for a settling system [45].

2.3 Thickeners

The main goal of a thickener is to maximise separation efficiency and underflow density while maintaining a clear liquid overflow [32]. This section examines the techniques and factors used to determine the appropriate size of thickeners for specific applications [7]. These include analysing settling data, applying theoretical models, and understanding the effect of compression on thickener sizing. A sketch of a thickener is displayed in Figure 4.

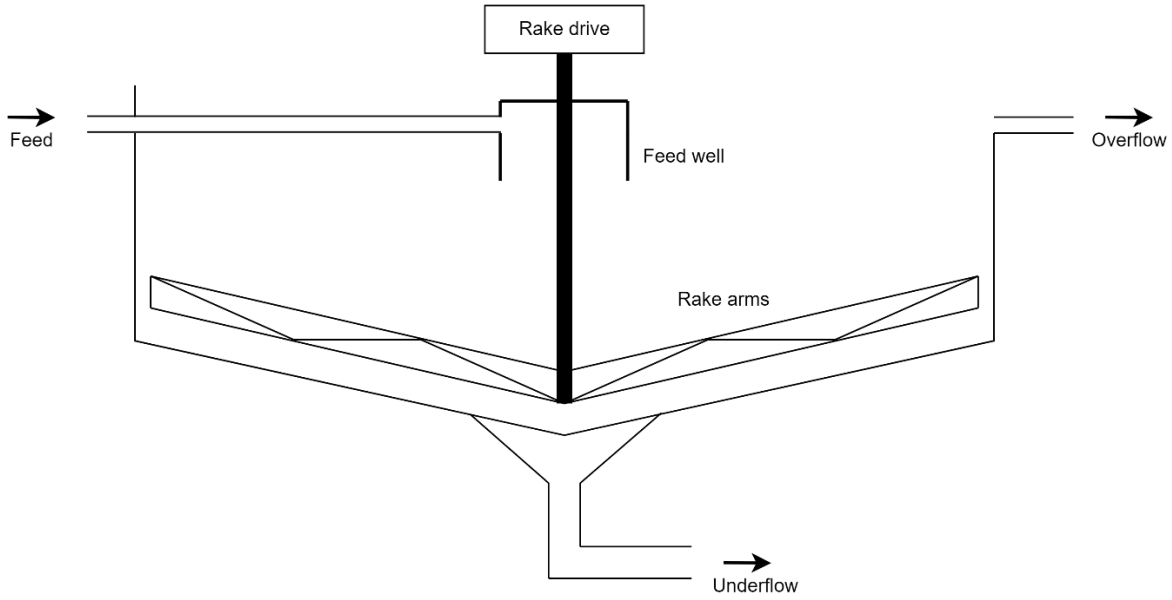

Figure 4: Basic thickener design

The feed of a thickener consists of a slurry mixture containing fine low-grade waste or ore and a solution. The feed is fed to the feed well where the slurry is evenly distributed across the area of the thickener allowing the settling process to occur uniformly [7]. The rake arms function is to move settled solids at the bottom of the tank to the centre of the thickener, this prevents solid build-up and allows for a more uniform particle distribution [7]. The sedimented particles, called

underflow, are collected from the bottom of each tank and subsequently sent for additional processing. The clarified liquid, known as overflow, is collected from the upper part of each tank via overflow launders and can be reused or directed to later stages of the processing plant [5] [32].

2.3.1 Evaluating Settling Data

2.3.2 Methods for Non-Flocculated Pulps

Coe and Clevenger developed a method in 1916 to size thickeners without flocculation [41]. This approach, based on zone sedimentation, is useful in scenarios where slurries do not require flocculation or contain reagents such as lime, resulting in minimal differences in floc size and dewatering characteristics [40] [41]. The sizing method's basic assumption is that the pulp's settling rate is only dependent on solids concentration, as demonstrated by the zone settling regime [41]. The equation is:

$$A = \frac{\left(\frac{1}{C_0} - \frac{1}{C_u}\right)}{v_0} \tag{7}$$

Where,

A = unit area, m^2/tpd

C_0 = initial solid concentration, kg/L

C_u = underflow solid concentration, kg/L

v_0 = initial settling rate, m/d

The Coe Clevenger equation is frequently used to calculate the ideal thickening area [32]. This is accomplished by doing sedimentation tests at various solid concentrations, determining the overflow and underflow concentrations, and calculating the area value for each concentration [41].

2.3.3 Methods for Flocculated Pulps

When polymers are introduced for flocculation, dilute suspensions yield larger flocs, necessitating different sizing methods [40]. Techniques derived from Kynch theory, such as the Talmage and

Fitch method, use settling curve data to determine unit area [39] [46]. Another approach, the Oltmann method, considers the onset of compression and its extension to the underflow line [32].

When employing polymers to flocculate suspensions, it's notable that dilute suspensions yield larger flocs than higher concentrations [32]. Hence, it's advisable to conduct a single test at the anticipated feed solids concentration. Methods derived from Kynch theory offer valuable tools for determining the unit area. The Talmage and Fitch method, utilizing Equation (8), stands prominent [46].

$$A = \frac{t_u}{C_0 H_0} \tag{8}$$

Where,

t_u = settling time, $days$

H_0 = initial height of pulp in test, m

Another method developed to address problems related to the use of modern flocculants is the Wilhelm-Naide model [47]. This model is preferred over the Talmage & Fitch method when working with modern flocculants [32] [7]. This model is adapted from the Yosioka & Hassett models, utilising the total thickener flux, settling flux, and withdrawal flux to define unit area [47] [48].

$$A = \frac{(\frac{b-1}{b})^{b-1}}{ab}\, C_u^{b-1} \tag{9}$$

With coefficients a and b calculated by equation 10:

$$v = aC_0^{-b} \tag{10}$$

Tangents to the settling curve extrapolated to the vertical axis, as demonstrated by Kynch, facilitate the determination of solids concentration (C_0). Plotting velocity versus solid concentration on log-log paper yields "a" and "b" values, which are then utilised in the Wilhelm-Naide equation (equation 9) to obtain the unit area value at the required underflow solids [32] [47].

2.4 Leaching

Leaching involves the selective dissolution of specific metals from a solid matrix into a solvent [49]. The solvent is typically acidic or alkaline. The effectiveness of leaching depends on the chemical dissolution rate and the contact duration between the solid particles and the solvent [49]. This section discusses and compares several leaching methods to identify a technique that balances leaching rate, efficiency, and cost. The CCD and multi-stage leaching techniques are further explored to enhance leaching efficiency.

2.4.1 Traditional leaching methods

Traditionally, three leaching techniques are used in hydrometallurgy, each with advantages and limitations: heap leaching, vat leaching, and agitated leaching [4]. Heap leaching involves placing crushed ore in a heap and irrigating it with a lixiviant [50]. The lixiviant then flows through the heap and is collected at the bottom. This method is very straightforward and cost-effective but is significantly limited by poor lixiviant contact and slow leaching kinetics [50]. Heap leaching is typically employed with lower-grade materials [50] [51]. Vat leaching involves submerging crushed ore in a solution within a large tank. The solution then percolates through the ore bed and is collected at the bottom of the vessel [52]. This method enhances leaching efficiency and recovery rates compared to heap leaching but also requires larger equipment and incurs higher operating costs [4]. Agitated leaching involves mixing finely ground ore with solvent in a tank and stirring the solution. This process achieves a higher recovery rate and faster leaching kinetics due to improved lixiviant contact and reduced diffusion limitations compared to vat leaching [53]. However, this method entails higher crushing and milling equipment costs and the need for additional processes for solid-liquid separation [4].

2.4.2 Methods of improving leaching recovery

Multi-stage leaching and CCD are two methods used to improve the recovery of traditional leaching techniques further [54]. Multi-stage leaching involves contacting the solid material with fresh lixiviant multiple times. The technique is thus implemented by contacting the solids with fresh lixiviant and allowing leaching to proceed. The spent lixiviant is removed, and fresh lixiviant is added to the remaining solid residue [55]. This method can be repeated until the desired leaching recovery is achieved.

After leaching, the slurry is divided into the overflow, comprising a clear pregnant leach solution, and a thickened slurry, consisting of remaining solids and pregnant leach solution [3]. CCD is a traditional washing method used after leaching and pre-thickening to recover the remaining

pregnant leach solution in the thickened slurry [56]. The CCD involves several thickeners with leached solids flowing countercurrently from the first thickener, while washing liquid enters the last [57]. This method can further enhance leaching recovery by adding a dilute acid to the washing liquid [3]. The CCD technique is explained in more detail in section 2.5.

2.5 Flocculants in mineral processing

Flocculants promote the aggregation of fine particles into larger clusters known as flocs, which settle more rapidly than individual particles and are composed of inorganic salts or polymers [58] [59]. Flocculants increase the settling rate and improve the clarity of the overflow liquid, enabling the design of more compact thickeners [59]. The mechanism of flocculation is illustrated in Figure 5.

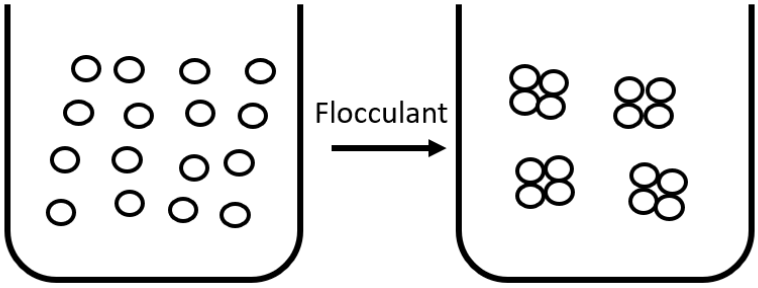

Figure 5: Flocculant mechanism

2.5.1 Types of flocculants

The flocculants used in mineral processing are classified by their ionic nature: anionic, cationic, and non-ionic [59] [58]. Anionic flocculants possess a negatively charged functional group that enables them to interact effectively with positively charged particle surfaces, typically under acidic or neutral conditions. Cationic flocculants feature a positively charged functional group that allows them to interact effectively with negatively charged particle surfaces, usually in basic conditions. The use of cationic flocculants in acidic media and metal-rich solutions is limited due to polymer degradation. Non-ionic flocculants are employed in situations where surface charge effects are less significant [58]. Generally, anionic flocculants are preferred in hydrometallurgical circuits because of the effectiveness of their negatively charged functional groups in acidic and metal-rich solutions [58].

2.5.2 Factors influencing flocculant performance

Flocculant performance depends on several factors: pH, flocculant dosage, mixing energy, and solid concentration. The pH of the slurry affects particle surface charge and can influence the

functional groups of the flocculant [58]. The flocculant dosage must be optimised to prevent over-flocculation and to ensure sufficient flocculant is used [58]. Over-flocculation occurs when too much flocculant is added, forming large flocs that trap water, decreasing settling rate and overflow clarity. Conversely, adding too little flocculant results in incomplete aggregation of solid particles, reducing the settling rate and overflow clarity [60]. Mixing energy is necessary to facilitate particle-polymer contact, but excessive shear can break the formed flocs [61]. The slurry's solid concentration affects the flocculant's distribution and should be considered when determining the appropriate dosage. Based on these slurry properties and mixing methods, the optimal flocculant type and dose must be identified through experimental testing [58].

2.6 Continuous countercurrent decantation (CCD)

After leaching, the slurry mixture of pregnant leach solution and remaining solid residue is sent to a thickener for solid-liquid separation. The overflow, pregnant leach solution, is then directed for further downstream processing, while the underflow, thickened slurry, still contains large amounts of pregnant leach solution. CCD is a washing step commonly used in hydrometallurgy and mineral processing facilities to recover the remaining pregnant leach solution [2] [62] [57]. A CCD circuit comprises a series of thickeners operating in a countercurrent flow configuration, in which the pulp and lixiviant streams flow in opposite directions [3].

2.6.1 Development and industrial application of CCD

CCD was initially developed for gold cyanidation circuits and was adopted in hydrometallurgical processes due to its high recovery efficiency. CCD is utilised in various applications, including gold cyanidation, aluminium, and copper recovery [3] [63] [64]. In each of these processes, a series of thickeners is used to wash the residual leachate and recover the remaining pregnant leach solution. The theoretical washing efficiency of a CCD system can be calculated using equation 11 [57]:

$$R = \frac{\frac{O}{U}\left[\left(\frac{O}{U}\right)^{N} - 1\right]}{\left[\left(\frac{O}{U}\right)^{N+1} - 1\right]} \tag{11}$$

Where,

R = fraction of dissolved value in the feed which is recovered in the overflow liquor of the first thickener

O = overflow liquor volume per unit weight of underflow solids

U = underflow liquor volume per unit weight of underflow solids

N = number of stages

2.6.2 Principle of CCD operation

The CCD system consists of thickeners operating in continuous countercurrent flow. The solid residue settles to the bottom of each thickener and is pumped to the next in the series, which is contacted with progressively cleaner washing liquid. The overflow is pumped back to the previous thickener, gradually increasing the dissolved metal concentration [57] [65].

The thickened slurry, comprising solid residue and the remaining pregnant leach solution along with washing liquid from the second CCD thickener, enters the first CCD thickener through the feed well. The solid residue settles to the bottom of the first CCD thickener, displacing clear lixiviant to the top. The thickener overflow contains the pregnant leach solution and is directed for further downstream processing. The underflow, which includes the solid residue and the remaining lixiviant, is sent to the second CCD thickener. Similar to the first, the second CCD thickener receives thickened slurry from the first CCD thickener mixed with washing liquid from the third CCD thickener, allowing it to settle. The overflow then proceeds to the first CCD thickener, while the underflow moves to the third CCD thickener. This countercurrent operation principle remains consistent regardless of the number of thickeners in a CCD system. In the final CCD thickener, clean washing liquid is added, and the solid residue is removed as waste. Flocculants aid particle aggregation and improve settleability at each CCD stage. Figure 6 shows the layout for a three-stage CCD system.

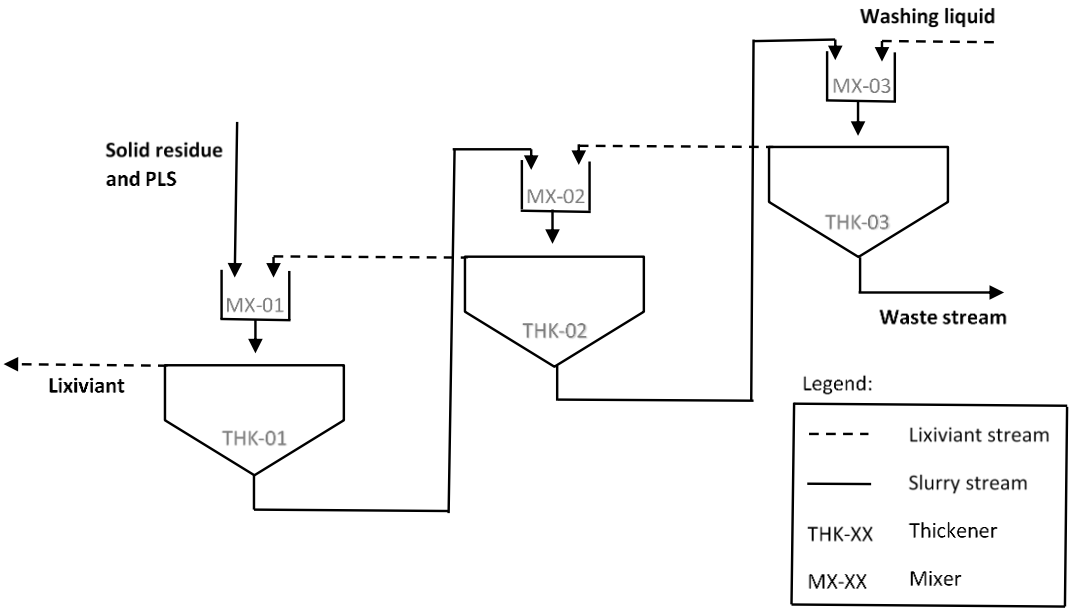

Figure 6: CCD layout

2.6.3 CCD as a secondary leaching step

The primary goal of a CCD system is to recover the remaining PLS mixed with the solid residues from the leaching stage. The CCD system can also serve as a secondary leaching stage by adding a dilute acid instead of the washing liquid to the final thickener in the series [3].

A concentration gradient is formed in each of the thickeners by adding a dilute acid to the last thickener in the CCD series. At each CCD stage, the lixiviant passing through causes the acid to be consumed, reducing its leaching capacity in subsequent stages. Additionally, with each CCD stage, the slurry passing through decreases the amount of target metal available for leaching on the particles' surface. In the first CCD thickener, the slurry from the leaching stage is contacted with washing liquid that has passed through two previous CCD thickeners. In the second CCD thickener, the slurry from the first CCD thickener is contacted with the lixiviant that has passed through one CCD thickener. In the third CCD thickener, the slurry from the two previous CCD thickeners is contacted with fresh lixiviant. This concentration gradient, created at each CCD stage, acts as a driving force, increasing the recovery of the target metals [66].

However, adding a dilute acid to the washing liquid directly influences the slurry's settling behaviour. The dilute acid changes the slurry's pH and ionic strength, affecting the surface charge of the particles [36] [67]. These changes in surface charge influence the settling characteristics by altering the flocculation properties of the slag, such as floc size and density [36] [67]. In practical applications of CCD systems, there is a trade-off between leaching and settling within the system.

2.6.4 CCD design parameters

Several factors influence the performance of a CCD system: the number of stages, washing ratio, and settling behaviour [3] [57]. The number of thickener stages within the CCD system determines the theoretical washing efficiency; more stages improve the displacement but also increase initial capital and operational costs [57]. The wash ratio indicates the proportion of fresh lixiviant added during the washing step relative to the lixiviant removed from the slurry before washing. A higher wash ratio means adding larger amounts of fresh lixiviant, which improves the displacement of entrained liquor. This results in more efficient washing and greater recovery of the entrained liquor [3]. However, increasing the wash ratio also raises operational costs, as more lixiviant must be added, creating a more dilute solution that is sent for downstream processes such as ion exchange and solvent extraction, further elevating costs [3]. The slurry's settling behaviour affects the thickener's sizing and the underflow's density. The particle settling rate determines the cross-sectional area required for the thickener; slurries that settle slowly need larger thickeners to handle higher throughput. In contrast, faster-settling slurries can manage the same throughput with a smaller cross-sectional area [59].

2.7 Summary of literature review

This literature review has examined slag generation and properties, sedimentation theory, thickener design, leaching techniques, flocculation, and continuous countercurrent decantation within the context of hydrometallurgical processing. Slag characteristics were shown to depend on smelting conditions and cooling methods, which influence environmental behaviour, leaching performance, and reuse potential. Ferrous slags are commonly reused due to their alkaline nature, while non-ferrous slags present greater environmental challenges but contain recoverable metal values.

The review outlined the theoretical basis of sedimentation through single-particle, hindered, and zone settling theories, which are used to interpret settling tests and support thickener design. Classical models such as Stokes' law and Kynch theory provide a useful framework but rely on idealised assumptions that limit their direct application to industrial slurries. As a result, experimental settling tests and empirical models are typically required to inform design. The use of flocculants was discussed in relation to their effect on settling behaviour and overflow clarity, with performance influenced by slurry chemistry, pH, dosage, and mixing conditions.

Leaching methods and recovery strategies, including CCD, were reviewed to illustrate the interaction between leaching efficiency and solid–liquid separation. CCD is widely applied for washing and solution recovery and may also function as a secondary leaching step. However,

changes in slurry chemistry during CCD, particularly pH and ionic strength, can affect settling behaviour and introduce design trade-offs.

Although substantial literature exists on slag processing and solid–liquid separation, gaps remain. In particular, there is limited information on the settling and flocculation behaviour of leached non-ferrous slag slurries under CCD conditions. In addition, many existing models do not fully account for the combined effects of slag mineralogy, slurry chemistry, and operating conditions. These limitations support the need for experimental investigation to inform CCD design and optimisation for slag-based systems.

Chapter 3: Methods and materials

This chapter provides a comprehensive overview of the FMO slag used in the following experiments, along with a summary of the methods employed, including the characterisation of the FMO slag, sample preparation, flocculant testing, production of lower-grade FMO slag and lixiviant, and batch sedimentation procedures.

3.1 Materials

Due to confidentiality issues, the source of the FMO slag used in this study and the nature of the operation cannot be disclosed. It can be characterised by its chemical composition, which includes Al, Ca, Fe, Li, Mn, and Si. The slag originates from a metal smelting process and is the unwanted by-product that forms on the top of the furnace. Images of the FMO slag particles before and after sample preparation are shown in Figure 7.

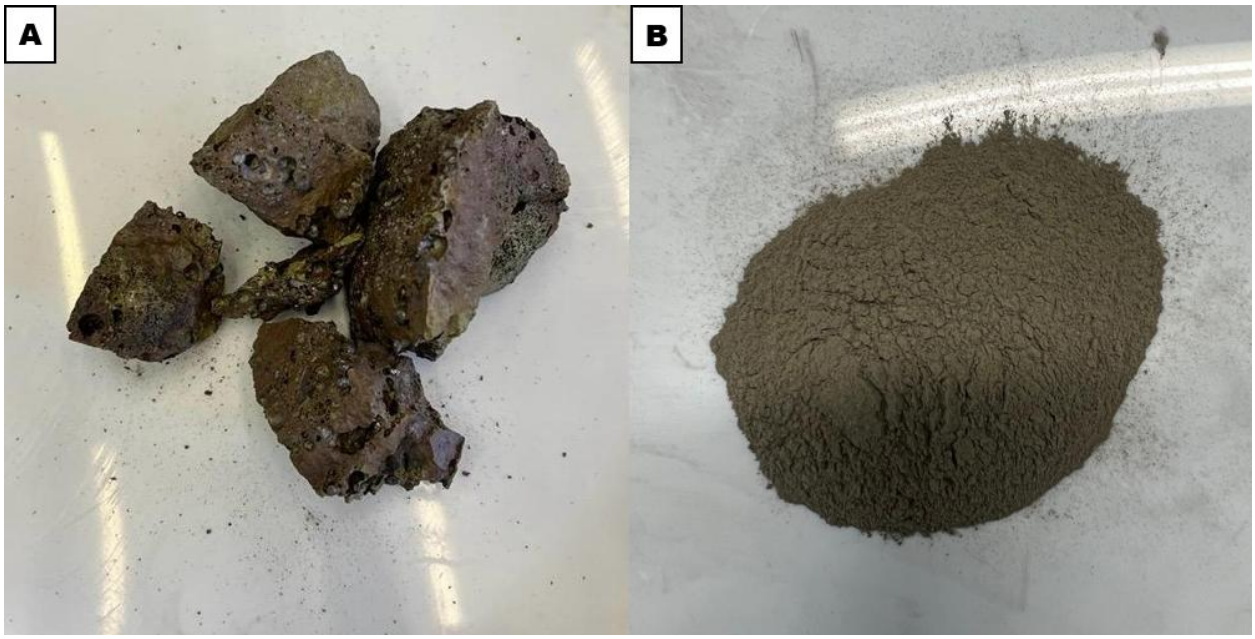

Figure 7: A) Large FMO slag pieces as received, B) FMO slag after sample preparation

3.1.1 Characterisation

The various physical properties and chemical composition measurement techniques are summarised in Table 5 and Table 6, respectively. The three physical properties of FMO slag examined were particle size distribution, particle surface properties, and particle density. Four methods were used to determine the chemical composition of FMO slag: microwave digestion, XRF, XRD, and SEM-EDX analysis.

3.1.1.1 Particle size distribution

The particle size distribution (PSD) of the FMO slag was measured using a Malvern Mastersizer 2000 instrument. The Malvern was operated by launching the Mastersizer 2000 software, which defines the parameters, including the dispersant type, refractive index, and air pressure settings. Next, running the system with an empty and clean chamber conducts a system background check. The sample was then loaded into the feeder, and the instrument was started. The software automatically generated a PSD with d_{10}, d_{50}, and d_{90} values. The International Organisation for Standardisation (ISO) outlined the procedure for PSD measurements in standard 13320 of 2009.

3.1.1.2 Surface properties

The surface properties of the FMO slag were determined by scanning electron microscopy (SEM). The initial step involved preparing the sample by depositing a small amount of FMO slag onto conductive carbon tape mounted on an aluminium stub. The sample was then coated with a thin layer of carbon using a vacuum sputter coater to improve its conductivity. The SEM analysis was carried out with a FEI Quanta 250 FEG scanning electron microscope, in conjunction with xT microscope Server and xT microscope Control software, following the manufacturer's guidelines. The scanning electron microscope captures images at various magnifications in a vacuum.

3.1.1.3 Density

A material's true density is the mass of the sample divided by its volume, excluding pores [18]. The true density of the FMO slag was measured using a Micrometrics AccuPyc II 130 Gas Pyrometer. The measurements involved weighing a 10 cm^3 cup filled halfway with the FMO slag, then placing it in the helium pyrometer. The instrument performed six measurements and provided each measurement's density result and standard deviation. The density tests followed the American Society for Testing and Materials (ASTM) standard ASTM D2638. A summary of the physical property measurement techniques, instruments and standards is provided in Table 5.

Table 5: Physical property measurement techniques for FMO slag

Slag property	Characterisation method	Instrumentation	Standard
Particle size distribution	Laser diffraction	Malvern Mastersizer 2000	ISO13320 (2009)
Surface properties	SEM	FEI Quanta 250 FEG	[Manufacturer's guidelines]
True density	Helium pycnometer method	Micrometrics AccuPyc II 130 Gas Pycnometer	ASTM D2638

3.1.1.4 Microwave digestion and ICP-OES

Microwave digestion was performed to dissolve the slag in preparation for elemental analysis using ICP-OES. The slag sample was prepared by weighing 0.2 g into a Teflon digestion vessel. The sample was digested with a mixture of 5 ml nitric acid, 1 ml hydrofluoric acid, and 4 ml distilled water, and placed in an Anton Paar Multiwave 5000 microwave reaction system. The digester was set to operate for 60 minutes at a temperature of 60 °C and a maximum pressure of 60 bar. After cooling, 6 ml of saturated boric acid was added to complex fluoride ions. This step was carried out in a microwave operating at 130 °C and a maximum pressure of 16.4 bar. The sample was then cooled again and filtered to confirm complete digestion. Any undissolved residue was collected and measured. The clear filtrate was transferred to a volumetric flask and diluted. The diluted sample was finally sent for ICP-OES analysis.

Inductive Coupled Plasma Optical Emission Spectroscopy (ICP-OES) is an analytical technique used to determine the elemental composition of a solution. The analysis was carried out using an Agilent 5800 instrument. First, the instrument was calibrated using a certified multi-element standard, De Bruyn, with concentrations ranging from 10 ppm to 250 ppm. Next, the samples were prepared for ICP-OES analysis by being diluted to fall within the calibration concentration range. Finally, the samples were analysed using the calibrated instrument, with quality control samples strategically included throughout the run to verify the accuracy and precision of the results.

3.1.1.5 X-ray fluorescence

X-ray fluorescence (XRF) is an analytical technique used to determine the concentrations of various chemical elements in a sample. First, the different elements within the samples were identified using a PANalytical Axios XRF instrument. The sample was prepared for XRF analysis using sample flux (Lithium Tetraborate: Lithium Metaborate (66:33)) and then fused on an RJM system XRFuse instrument at 1100 °C. This process created fused beads or glass pellets, which were placed into an Axios Max XRF instrument. This instrument measured the percentage of each element by comparing against a set of WROXI and AMIS standards. The samples were subsequently irradiated using an Rh X-ray tube. Finally, the results were presented as percentages for the major oxides and as parts per million (ppm) for trace elements. The XRF analysis was conducted in accordance with the guidelines outlined in ISO 12677:2011.7:2011.

3.1.1.6 X-ray diffraction

X-ray diffraction (XRD) is an analytical technique used to identify and quantify crystalline phases in a sample. Initially, a broad range identification was performed to characterise the crystal structure of the crystalline material using a PANalytical X'Pert Pro instrument. Subsequently, the sample was prepared for XRD analysis using a black-loading technique. The samples were then loaded onto the spinner stage inside the XRD. They were scanned using an X-ray generated by a Co X-ray tube with an Fe filter. An X'Celerator operating at 45kV and 40mA produced a diffractogram for each sample. From the diffractogram, the different phases and their respective concentrations within the sample were identified. The peak position determines the phase present, while the peak height indicates concentration. The different phases were identified by comparing the diffractogram to the International Centre for Diffraction Data (ICDD)(PDF 4+) database, which contains over 300,000 crystalline phases. A Rietveld refinement was then performed to determine the weight percentage of each mineral in the sample. There is currently no standard method for the XRD analysis of slag; the procedure used is based on the manufacturer's guidelines.

3.1.1.7 Energy dispersive X-ray spectroscopy

Energy dispersive X-ray spectroscopy (EDX) analysis determines the distribution of different metals on a sample's surface. The EDX analysis was performed in combination with the previously mentioned SEM analysis. It used the same FEI Quanta 250 FEG instrument in combination with an X-Max SDD 20mm^2, Oxford Instruments Inc. detector and Aztec software. EDX analysis mapped and displayed the chemical composition on the SEM images. A summary

of the chemical composition measurement techniques, instruments and standards is provided in Table 6.

Table 6: Chemical composition measurement techniques for FMO slag

Characterisation method	Instrumentation	Standard
Microwave digestion and ICP-OES	Anton Paar Multiwave 5000 microwave reaction system Agilent 5800 ICP-OES	[Widely accepted method] [Widely accepted method]
XRF	PANalytical Axios XRF instrument RJM system XRFuse instrument Axios Max XRF instrument Rh X-ray tube	ISO 12677:2011
XRD	PANalytical X'Pert Pro instrument X'Celerator	[Manufacturer's guidelines]
EDX	FEI Quanta 250 FEG X-Max SDD 20mm^2, Oxford Instruments Inc.	[Manufacturer's guidelines]

3.2 Methods

The methods section is divided into six steps: sample preparation, production of leached FMO slag, flocculant testing, production of an intermediate product for CCD settling, batch sedimentation, and CCD-condition batch settling.

3.2.1 Sample preparation

FMO slag was received in large chunks, between 5mm and 1000mm, and had to undergo size reduction to be suitable for sedimentation. The sample preparation process is divided into six

main steps: crushing, magnetic separation, sample splitting, milling, sieving and rotary splitting. The sample preparation methods used in this section are illustrated in Figure 8.

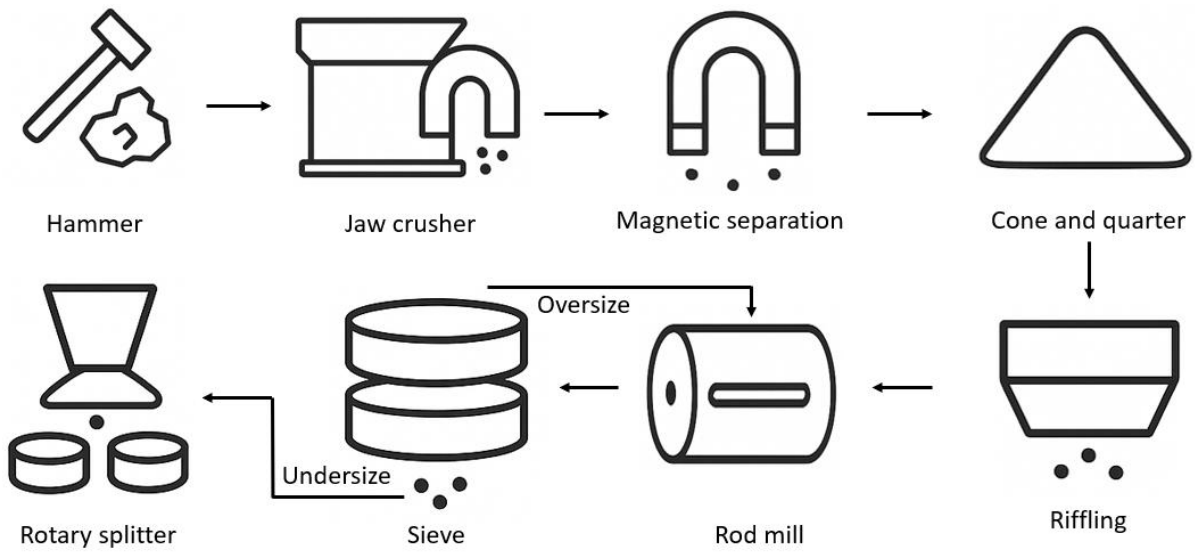

Figure 8: Sample preparation methods used

During the crushing phase, particles were reduced in size through two crushing steps: impact crushing with a hammer and jaw crushing. A hammer was initially used to reduce particles to below 200mm for processing in a jaw crusher. The jaw crusher was operated at various settings to reduce the particle size below 3mm. At a size below 3 mm, most of the hard magnetic material trapped within the slag was released [68]. A permanent magnet was then used to remove any hard magnetic material liberated from the crushing process. These ferro-metallic fragments are shown in Figure 9 and are believed to be trapped ferro-metal droplets that did not settle through the slag during smelting.

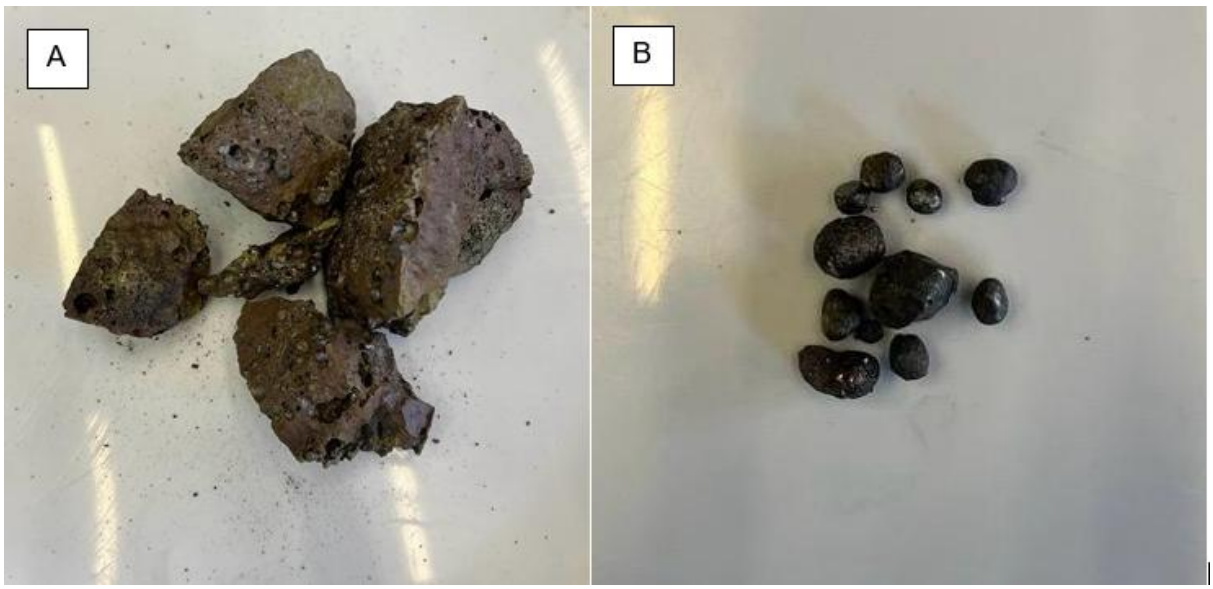

Figure 9: A) Large FMO slag pieces received, B) Hard magnetic material removed from FMO slag

After magnetic separation, the sample was split. The sample was first thoroughly mixed using a coning-and-quartering technique. This involved pouring the sample onto a tarp to create a cone-shaped pile [68]. The pile was then flattened and divided into four quarters. Opposite quarters were mixed, and finally, the two piles were combined [68]. This process was repeated to ensure the sample was homogeneous. Sample splitting of the homogeneous sample was carried out using a riffler. The riffler comprised a splitter with equal-width chutes and two collection pans beneath it. The sample was carefully poured into the centre of the splitter. It was then divided into two sub-samples, which were subsequently split again using the riffler. This process was repeated until the desired sample size was obtained.

The milling process used a dry rod mill. Samples from the splitting stage were poured into the rod mill and operated for 30 minutes. The samples were then sieved for 5 minutes. The undersized particles were removed, and any oversized material was returned to the rod mill for another 30-minute run. This cycle repeated until the entire sample reached the desired maximum particle size of 125 µm. The remaining hard magnetic material from the samples was removed from the larger sieves. Finally, a rotary splitter divided the samples into smaller subsamples suitable for laboratory testing. The rotary splitter comprised a hopper, a discharge spout, and a turntable. The sample was placed in the hopper. When the rotary splitter was activated, the turntable rotated at a steady rate, and the hopper and discharge spout vibrated to maintain a continuous flow of the sample. The sample was then discharged onto a turntable with six collection bins arranged in a circle.

3.2.2 Producing leached FMO slag

Leached FMO slag was produced by mixing crushed FMO slag with a 1% sulphuric acid solution to form a 5 or 10 wt% solids mixture. The mixture was then placed in a laboratory bottle, which was subsequently placed inside a laboratory shaker. The shaker was set to 170 rpm to ensure a homogeneous solution, and the sample was shaken for 24 hours. The resulting product was then divided into two outputs: the FMO slag bed (notation: FMO[0], where the number in brackets refers to the number of CCD stages slag as passed through) and the pregnant leach solution (PLS). The FMO[0] was sent to a CCD system for washing to improve dissolved metal recovery, and the PLS was sent for further processing.

3.2.3 Flocculant test

The flocculant test was carried out according to the standard of the Marlyn Laboratory. This section outlines the experimental design, setup, and data collection methods.

3.2.3.1 Experimental design

This part of the study aimed to evaluate the performance of various flocculants on the settling characteristics of FMO slag leach residue. Only two variables were tested during this phase: flocculant type and dosage. The following variables were fixed: particle size, solid-liquid ratio, and leaching conditions. The flocculant test was divided into three sections: the screening study, the variable dosage study, and the optimisation study.

In the screening study, a standard flocculant dosage of 20 g/ton was selected, as recommended by Marlyn Laboratory, with the only variable being the type of flocculant used. In the variable dosage study, the flocculants from the screening study were retested at half or double the original dosage, depending on the initial settling rate. The best-performing flocculant from the screening and variable dosage study was then selected based on settling rate, lixiviant turbidity, and bed solid percentage. Finally, the optimisation study tested the best-performing flocculant at 10 different dosages to determine the optimal dosage. The variables measured as evaluation metrics were the settling rate, the lixiviant's turbidity, and the bed's solid percentage. The experiment was repeated three times to ensure data reliability.

3.2.3.2 Experimental setup

The leached FMO slurry was prepared as described in section 3.2.2. The sample was then treated with a diluted flocculant at 0.05% and shaken at 120 rpm for 2 minutes. The shaker ensured the flocculant was evenly distributed within the slurry, creating a uniform mixture. The sample was

then transferred to 500 ml settling columns, inverted five times, and left to settle for 10 minutes. During settling, the slurry-liquid interface was monitored. After settling, turbidity, pH, and bed height measurements were taken. This process was carried out in a fume hood to vent any hydrogen sulphide gas that forms during leaching. The experimental setup for the flocculant test is shown in Figure 10.

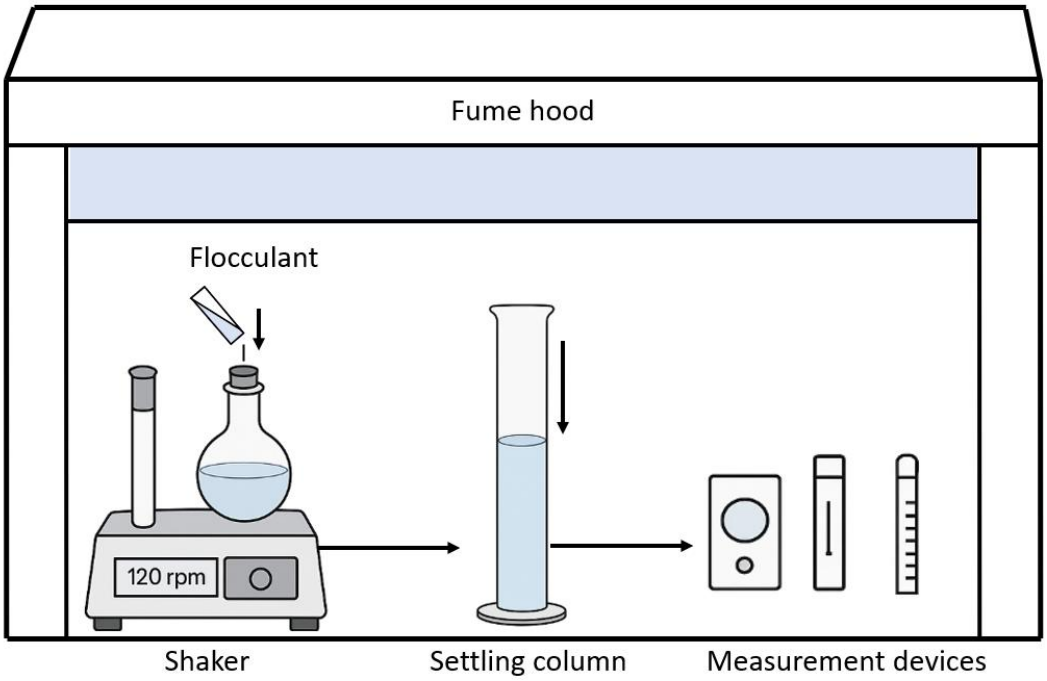

Figure 10: Laboratory setup for flocculant testing experiments

3.2.3.3 Data acquisition

During the settling phase, the height of the slurry-to-liquid interface was measured every 5 seconds for the first minute, every 10 seconds between the first and third minutes, and finally every 30 seconds after three minutes. The final bed height was noted and used to calculate the final bed density. A video was also recorded during the settling phase to confirm the measurements. After the settling phase, some lixiviant was decanted from the top of the settling column and used to measure the turbidity and pH. Turbidity was measured with a HATCH 2100Q portable turbidimeter, and pH was measured with a HANNA HI5521 pH meter. The measurement techniques and their instruments are summarised in Table 7.

Table 7: Analytical measuring technique used for data acquisition during flocculant tests

Measurement	Instrument
Turbidity	HATCH 2100Q portable turbidimeter
pH	HANNA HI5521 pH meter
Bed density	Measuring tape

3.2.4 Method for producing intermediate products for CCD settling

During CCD operation, the lixiviant is moved in one direction while the FMO slag pulp flows in the opposite direction. This created a concentration gradient between tanks and facilitated effective particle leaching. Thus, during batch sedimentation, CCD conditions had to be simulated. This was achieved by producing intermediate leached solids and intermediate loaded lixiviants. Figure 11 shows the CCD setup, demonstrating how the concentration gradient between tanks was maintained using different intermediate leached solids and intermediate loaded lixiviants.

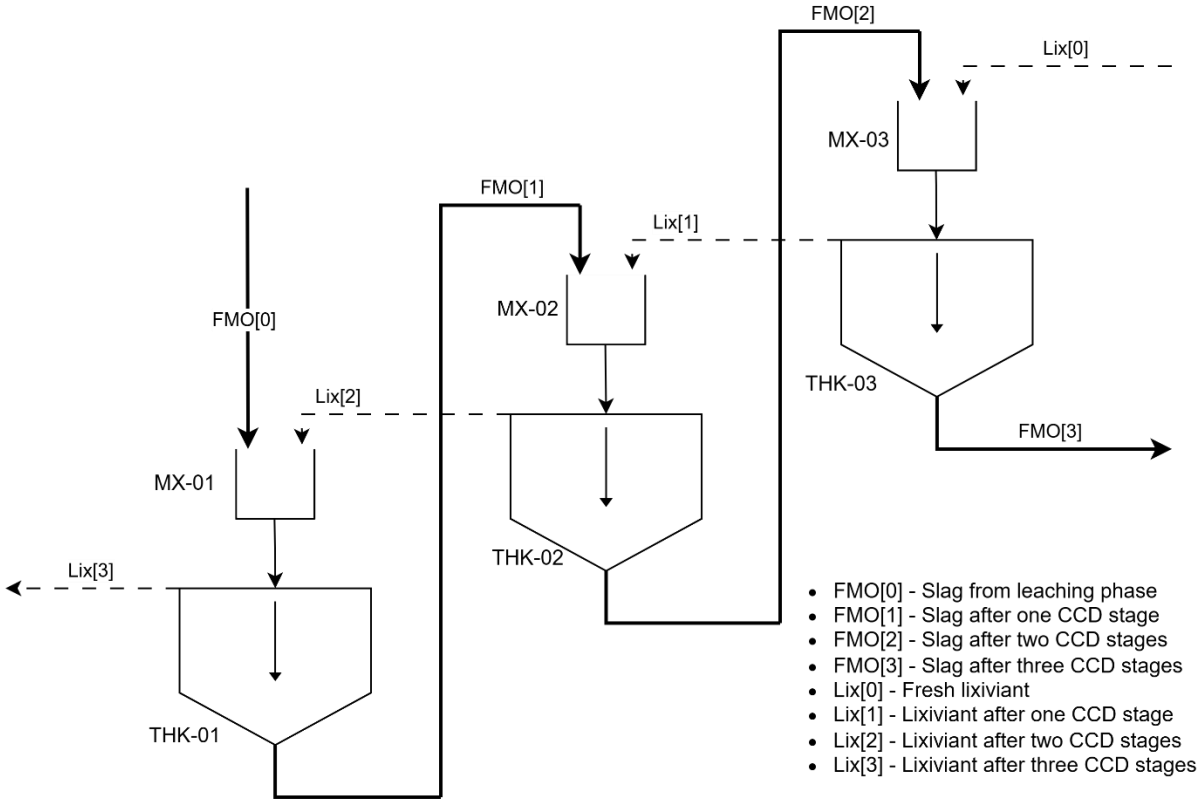

Figure 11: CCD setup illustrating concentration gradient

During batch sedimentation, a three-stage CCD system was simulated by conducting three different runs:

- Lix[0] with FMO[2]
- Lix[1] with FMO[1]
- Lix[2] with FMO[0]

Where FMO[0] was produced as described in section 3.2.2, and Lix[0] was prepared by diluting a 98.8% sulphuric acid solution.

The challenge involved producing the intermediate products FMO[1], FMO[2], Lix[1], and Lix[2] from only FMO[0] and Lix[0]. This was achieved by reacting FMO[0] and Lix[0] to form the intermediate products FMO'[1] and Lix'[2]. Next, reacting FMO'[1] with Lix[0] produced the intermediate products Lix'[1] and FMO'[2]. These intermediates, Lix'[1] and Lix'[2], were then used to produce the final products. By reacting FMO[0] with Lix'[2] yielded FMO[1]' and Lix[3]', while reacting FMO[1]' with Lix'[1] produced FMO[2]' and Lix[2]'. Finally, FMO[2]' reacted with Lix[0] to form FMO[3]' and Lix[1]'. Table 8 summarises the intermediate and final CCD products.

Table 8: Summary of reactions used to produce intermediate and final CCD products

Intermediate products

Settling reactions	Product	By-product
FMO[0] + Lix[0] → FMO'[1] + Lix'[2]	Lix'[2] and FMO'[1]	-
FMO'[1] + Lix[0] → FMO'[2] + Lix'[1]	Lix'[1]	FMO'[2]

Final products

Settling reaction	Product	By-product
FMO[0] + Lix'[2] → FMO[1]' + Lix[3]'	FMO[1]'	Lix[3]'
FMO[1]' + Lix'[1] → FMO[2]' + Lix[2]'	FMO[2]' and Lix[2]'	-
FMO[2]' + Lix[0] → FMO[3]' + Lix[1]'	Lix[1]'	FMO[3]'

The reactions to produce the final and intermediate products described in Table 8 were performed in 2-litre volumetric flasks. The FMO samples, which consist of the bed of a pre-leached solution, were mixed with the corresponding washing liquid as shown in Table 8. The FMO slag and lixiviant were then left to react for 30 minutes. The lixiviant was then separated from the FMO slag by allowing the solids to settle to the bottom, and most of the clear lixiviant was poured out. Each sample was then decanted with a decanter to remove the remaining lixiviant and to form an FMO bed with 30 wt% slag. The 30 wt% slag in the bed was kept constant across all experiments by decanting the same amount of lixiviant in each stage. As described in Table 8, this process was repeated for all five reactions to produce the final products that were used to simulate CCD settling, namely Lix[1]' and Lix[2]'. All intermediate products produced for CCD settling were used the same day they were produced.

3.2.5 Batch sedimentation

3.2.5.1 Experimental design

This part of the study aimed to determine the settling characteristics of FMO slag. First, baseline data were collected by performing settling tests under various conditions. These conditions include settling in water, settling after leaching, and settling after leaching with a flocculant as a settling aid. These tests were conducted at the pre-selected particle size, solid-liquid ratio, flocculant type, and dosage.

The baseline data helped quantify the effects of flocculants, leaching, and the continuously changing acid medium on the settling rate. The settling after leaching with a flocculant test was also used to design a pre-thickener, the first step after leaching, to separate most of the pregnant leach solution. Finally, the influence of a continuously changing acid medium (CCD conditions) on the settling characteristics of FMO slag was assessed. This was tested by performing settling tests with the intermediate leached solids and intermediate loaded lixiviants, as described in section 3.2.4.

3.2.5.2 Experimental setup

The settling rig comprised three standard 2-litre settling columns linked by a metallic framework and a light bar. The metallic framework enabled the columns to rotate 360 degrees, thereby improving the mixing consistency of the slurry before settling. The light bar was positioned behind the settling rig before settling began to provide a visible liquid slurry interface. The settling rig is depicted in Figure 12.

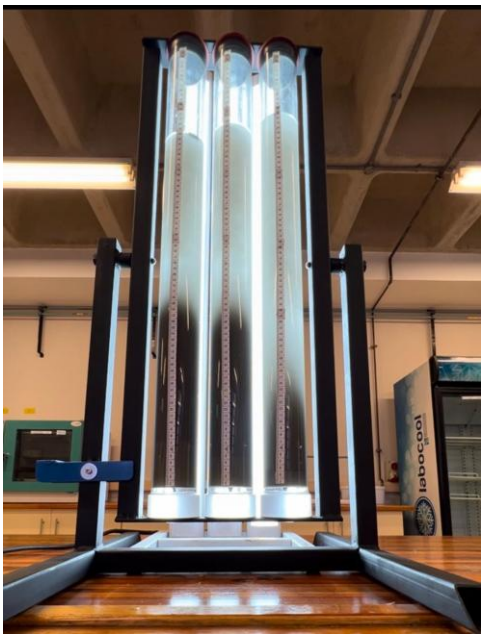

Figure 12: Experimental set-up for batch settling

3.2.5.3 Baseline data batch settling

During the initial settling tests, baseline data were collected by settling FMO slag in water. The FMO slag was mixed with water in 2-litre Erlenmeyer flasks. The mixture was then lightly stirred and poured into the 2-litre settling columns. The settling columns were sealed and rotated using the metal framework. The mixture was rotated until a uniform blend of solids and liquid was

achieved. It was then allowed to settle under the influence of gravity. A light bar was positioned behind the settling rig to improve the visibility of the liquid slurry interface.

The second and third sets of baseline data were conducted similarly, with the only difference being the addition of a flocculant in the third set of settling tests. These tests involved settling a leached FMO slag solution, both with and without a flocculant. FMO slag was leached as described in section 3.2.2 of this report. Similar to the first set of settling tests, the leached FMO slag solution was placed into 2-litre Erlenmeyer flasks. A flocculant was added only for the third set of baseline data. The mixture was then gently stirred and poured into 2-litre settling columns. The columns were sealed and rotated using the metal structure until a homogeneous blend of solids and liquids was achieved. The mixture was then left to settle under gravity. A light bar was positioned behind the settling rig to improve visibility of the liquid slurry interface.

After settling, a 50ml sample of the clear lixiviant was collected from each settling column. This sample was then used to measure the lixiviant's turbidity. Additionally, once settling was complete, a height versus time graph was created for each run. The turbidity and height versus time graph served as baseline data for comparison with settling in a changing acidic medium.

3.2.5.4 CCD condition batch settling

The final set of settling tests involved a mixture of intermediate leached solids and intermediate loaded lixiviants, as described in section 3.2.4 of this report. Batch settling of these materials was carried out to simulate the concentration gradient within a CCD system. The settling reactions used to simulate CCD interactions are shown in Table 9.

Table 9: Settling reactions used in CCD simulation

Settling reaction	Product	By-product
FMO[0] + Lix[2]' → FMO[1] + Lix[3]	FMO[1]	Lix[3]
FMO[1] + Lix[1]' → FMO[2] + Lix[2]	FMO[2] and Lix[2]	-
FMO[2] + Lix[0] → FMO[3] + Lix[1]	Lix[1]	FMO[3]

Batch settling followed a process similar to that described in section 3.2.5.3 of the report. The intermediate leached solids and intermediate loaded lixiviants were mixed in an Erlenmeyer flask, then dosed with a flocculant, gently mixed, poured into the settling columns, inverted until a uniform mixture forms, and then allowed to settle under gravity.

After settling, the clear lixiviant was decanted until a 30 wt% solids bed remained. Then, a 33 ml (approximately 10 g slag) sample of the solid bed was taken, along with a 50 ml sample of the lixiviant for further analysis. The remaining slag bed and lixiviants were used in the next settling test, as shown in Table 9.

The slurry samples underwent vacuum filtration, which removed most of the remaining lixiviant from the solid samples. The solids were then washed with deionised water to remove any acids or flocculants on the slag surface. The slag was then separated again by vacuum filtration and dried in an oven. The dried samples were subsequently sent for two analyses: PSD and helium pycnometry. PSD analysis determined whether particle size changes due to leaching and settling. Helium pycnometry was used to determine whether the true density of the FMO slag changes during leaching and settling.

The lixiviant samples were then prepared for further analysis by undergoing syringe filtration. The samples were sent for four analyses: turbidity, pH, viscosity, and ICP-OES analysis. Turbidity was measured before filtration to determine the amount of suspended material still in the lixiviant. pH was measured to assess acid consumption at each CCD stage. Viscosity was measured to evaluate its impact on the settling velocity. The samples were also sent for ICP-OES analysis to determine the chemical composition of the lixiviant and calculate the degree of dissolution at each CCD stage.

Chapter 4: Results and discussion

This section presents and analyses the results obtained through slag characterisation, flocculant, leaching, and settling experiments. The outline of this result section is displayed in Figure 13.

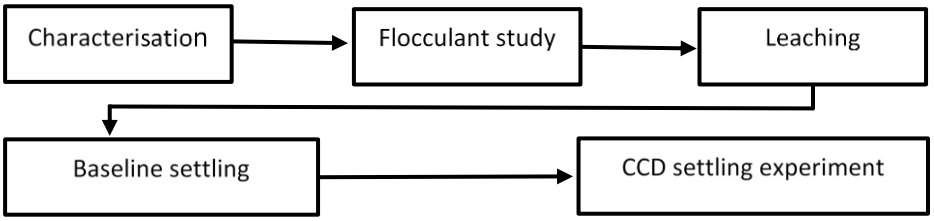

Figure 13: Results section outline

4.1 Characterisation of material

The FMO slag used to produce the slurry for the settling experiments was analysed for different physical and chemical properties. This analysis required several analyses, including XRF, XRD, microwave digestion and ICP-OES, SEM-EDX, PSD, and density. The results provide information that helps understand the results of the leaching and settling experiments and are used to size a CCD system.

4.1.1 Elemental composition of the FMO slag

X-ray fluorescence (XRF) analysis was used to determine the elemental composition of the FMO slag. The XRF results of the FMO slag are compared to those of a similar slag characterised by Rai (2002). The XRF results for major elements present are shown in Table 10. A summary of the main elements present is shown in Table 11.

Table 10: XRF of major elements present in slag compared with high MnO and low MnO slag [18]

Constituent	FMO slag (wt%)	High MnO slag (wt%)	Low MnO slag (wt%)
SiO2	24,92	28,32	39,00
CaO	8,84	11,00	14,00
Al2O3	23,37	10,50	9,63
MnO	25,35	26,00	15,00
MgO	4,02	14,90	11,50
Na2O	0,26	2,65	2,54
K2O	0,95	5,06	4,12
Fe2O3	2,65	0,31	0,23

Table 11: Summary of major elements present in FMO slag

Element	**%wt. of slag** [% g element/g total]
Mn	19.63%
Al	12.22%
Si	11.65%
Ca	6.32%
Mg	2.42%
Fe	1.85%
Oxygen	36.49%
LOI	5.55%
Other elements < 1%	3.48%
SUM	99.62%

The XRF results in Table 10 and Table 11 reveal that the FMO slag consists primarily of manganese oxide, silicon dioxide, and aluminium oxide. These three components account for 73.37 wt% of the total slag mass. Other major constituents include calcium oxide, magnesium oxide, ferric oxide, sulphur trioxide, and titanium dioxide, which together comprise 18.34 wt%. The minor components, potassium oxide, sodium oxide, vanadium pentoxide, and chromium oxide, account for an additional 1.3 wt% of the FMO slag. Other trace elements detected contribute 1.06 wt%, as shown in Appendix C. The loss on ignition (LOI) accounts for 5.55 wt% of the slag and represents volatile components such as moisture, carbonates, and organic matter. The XRF data will aid in understanding the settling and leaching characteristics of the FMO slag and establish a baseline chemical composition to determine leaching efficiency.

4.1.2 Crystal structure of the FMO slag

X-ray diffraction (XRD) was used to determine and study the crystal structure of FMO slag. The results obtained from using a Malvern Panalytical Aeris diffractometer with a PIXcel detector are summarised in Figure 14.

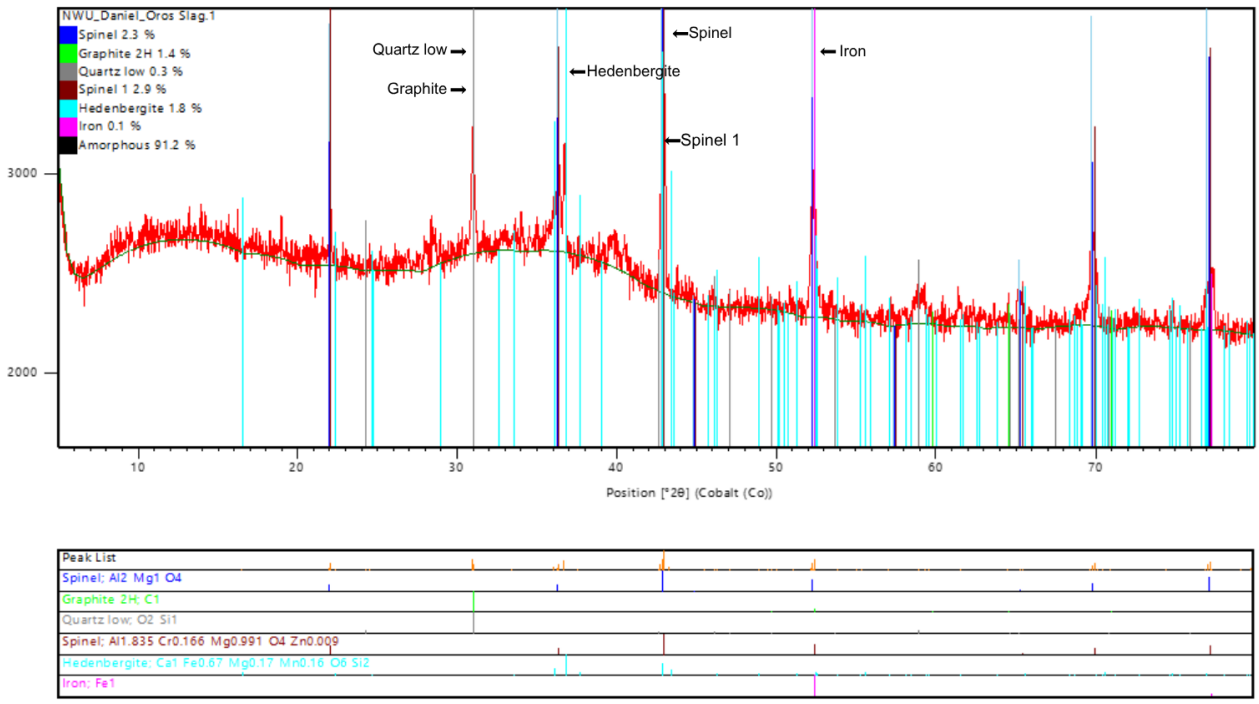

Figure 14: XRD diffractogram

The XRD diffractogram was analysed using X'Pert Highscore plus software to identify the phases present and the Rietveld method to quantify the relative amounts of each present phase. The identified phases and their quantities are summarised in Table 12.

Table 12: XRD phases and quantities identified

Phase	Quantity (wt%)
Amorphous	91,2%
Spinel 1 (Al, Cr, Mg, Zn, O4)	2,9%
Spinel (Al2, Mg, O4)	2,3%
Hedenbergite (Ca, Fe, Mg, Mn, O6, Si2)	1,8%
Graphite 2H (C)	1,4%
Quartz low (O2, Si)	0,3%
Iron (Fe)	0,1%

The high amount of amorphous phase suggests that the FMO slag cooled quickly, preventing widespread crystallisation. This may result from rapid cooling or quenching, which produces a glassy matrix [8]. The spinal phases are commonly found in slag containing iron and aluminium. These phases could originate from early-formed oxide crystallites embedded within the glassy amorphous matrix. The presence of hedenbergite in the slag indicates localised crystallisation of calcium, iron, and silicon, possibly due to added calcium during melting [8]. The small quantity of graphite present could indicate incomplete combustion during smelting. Trace amounts of iron could point to tiny metal droplets formed under locally reducing conditions. This is further

supported by the presence of hard ferromagnetic materials, which were removed by magnetic separation.

The high amorphous content in this slag will affect its breakage, settling, and dissolution properties. The breakage behaviour of a glassy material that breaks irregularly differs from that of crystalline materials, which tend to break along lattice planes, producing a material that is easier to break but uncontrolled, resulting in a broad particle size distribution. The irregular particle shape and wide particle size distribution resulting from the milling process negatively affect the setting properties. The dissolution kinetics of the glassy phase are faster than those of the crystalline phase due to its bonds being less stable.

4.1.3 Microwave digestion and ICP-OES

Microwave digestion was used to break down the solid FMO sample into a homogeneous liquid. ICP-OES then analysed the homogeneous liquid for accurate elemental analysis. The results from the ICP-OES analysis are summarised in Table 13.

Table 13: Summary of ICP-OES analysis

Element	%wt. of slag [% g element/g total]
Si	20,51%
Mn	16,11%
Al	9,22%
Ca	7,68%
Mg	2,01%
Fe	1,76%
Na	0,86%
K	0,81%
Li	0,30%
Measured elements < 0,1%	0,04%
Slag not dissolved	6,45%
Other	34,25%

The ICP-OES results show that silicone and manganese are the most abundant elements in the FMO slag, with 20,51 wt% and 16,11 wt%, respectively. Other significant elements include aluminium and calcium at 9.22 wt% and 7.68 wt%, respectively. Additional elements with smaller concentrations include magnesium, iron, sodium, potassium, and lithium. Trace elements such as cobalt, copper, and nickel comprise another 0,04 wt% of the slag mass. The slag contains a component not dissolved during microwave digestion, accounting for 6,45 wt%. Furthermore, a

portion labelled " other " makes up 34,25 wt% of the slag, primarily consisting of oxygen and a small number of trace elements not measured during the ICP-OES analysis.

The microwave digestion and ICP-OES method results for determining the elemental composition of the FMO slag are used in the data processing. This is to maintain accuracy as the lixiviants produced in the CCD test work stages are also analysed using ICP-OES. XRF elemental analysis was performed to verify the accuracy of the ICP-OES analysis.

4.1.4 Surface images, topography (morphology), and elemental composition of the FMO slag

Scanning electron microscopy with energy-dispersive x-ray spectroscopy (SEM-EDX) was used to produce high-resolution images and to provide elemental analysis of the FMO slag. The data gathered provides insight into the slag's particle shape and elemental distribution. SEM images of two samples, namely the -2 mm sample as received and the -125 µm sample used in settling, are displayed in Figure 15. The EDX data gathered for the two samples are shown in Table 14. Finally, the EDX mapping of the two samples is depicted in Figure 16.

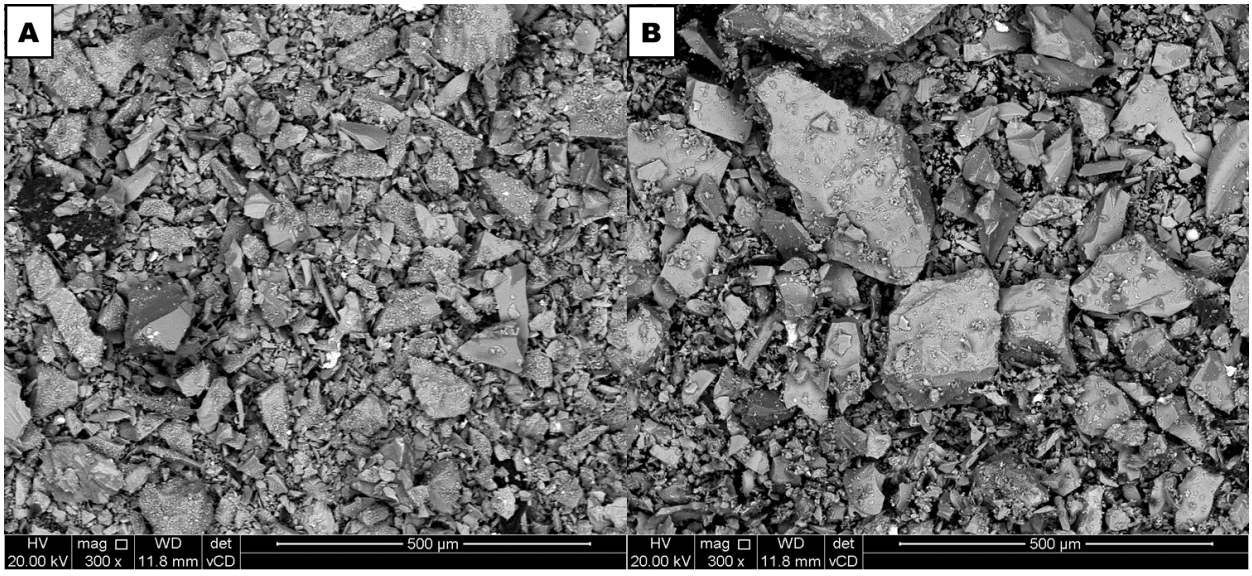

Figure 15: SEM images gathered of FMO slag A) -125 µm, B) -2 mm

The SEM images in Figure 15 reveal a broad particle size distribution, with some particles just below the maximum size of the distribution and others much smaller. The particles exhibit highly irregular morphology, with particles in the same sample characterised by angular, cuboidal and flaky shapes. The irregular shape may be due to grinding and milling processes or to the material's predominantly amorphous nature. The irregular shape and wide particle size distribution will influence the settling and leaching characteristics.

Table 14: EDX data of FMO slag gathered for -125 µm and -2 mm samples

Sample	-125 µm (wt%)	-2 mm (wt%)
O	38.3	38.8
Mn	23.0	24.9
Al	10.1	9.1
Ca	10.0	9.9
Si	9.8	9.5
Mg	2.2	1.3
F	1.5	1.3
Ba	1.1	1.2
Fe	1.0	0.8
K	0.8	1.0
Ti	0.7	0.7
W	0.6	0.4
S	0.6	0.5

EDX analysis provides information about approximately 1 to 3 microns of the slag sample's surface. Table 14 shows that the elemental composition of the first 1 to 3 microns of slag does not change significantly by milling from -2 mm to -125 µm. This proves that the FMO slag is fairly homogeneous and that very little phase liberation happens during the milling process.

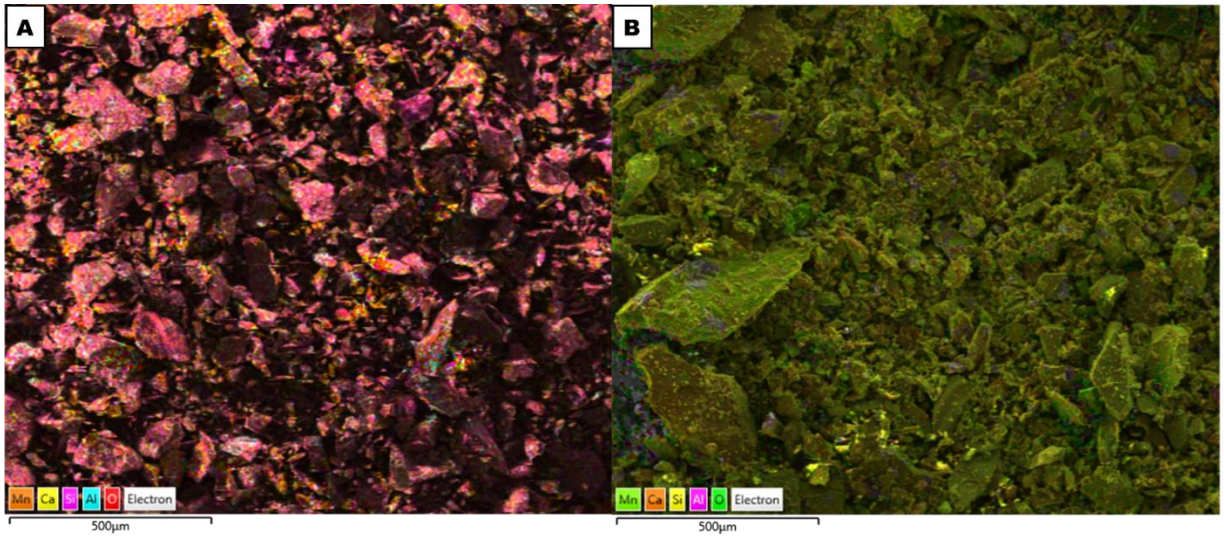

Figure 16: EDX mapping of FMO slag A) -125 µm, B) -2 mm

The EDX mapping is displayed in Figure 16. It shows that the samples generally have a homogeneous elemental distribution with some silicon and calcium hotspots in both the -2 mm and -125 µm samples.

4.1.5 Particle size distribution results

The PSD of the sample was determined using the Malvern Mastersizer 2000 instrument. The PSD of the -125 µm sample is shown in Figure 17, and the percentile values of d_{10}, d_{50}, d_{90} and $d_{[4,3]}$ are shown in Table 15.

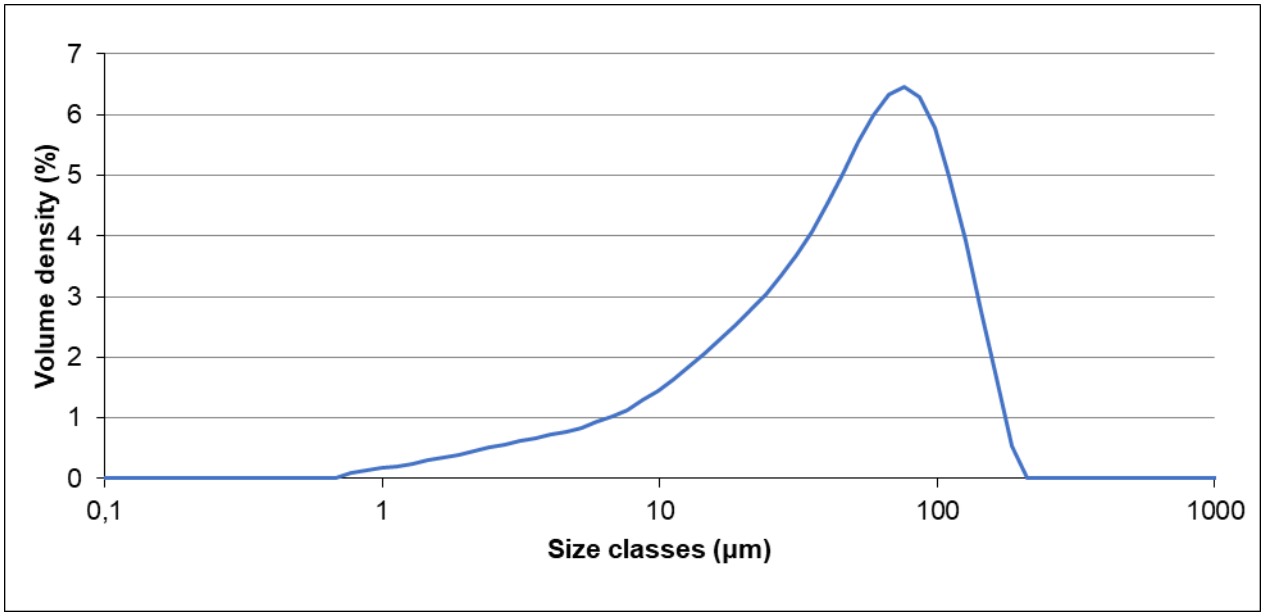

Figure 17: PSD of -125 µm FMO slag sample

Table 15: d_{10}, d_{50}, d_{90} and $d_{[4,3]}$ percentile values of FMO slag

FMO slag sample	d_{10} (µm)	d_{50} (µm)	d_{90} (µm)	$d_{[4,3]}$
-125 µm	8.48	52	123	59.7

From the data shown in Table 15, the span of the distribution can be calculated:

$$Span = \frac{Dv(90) - Dv(10)}{Dv(50)} = \frac{123 - 8.48}{52} = 2.20$$

A span of 2.20 indicates a broad particle size distribution around the median and, as such, includes both finer and coarser particles. This wide distribution can affect the settling and leaching of the FMO slag. Concerning settling, coarser particles tend to settle quickly, while finer particles take longer [33]. Concerning leaching, finer particles offer a larger surface area, enhancing leaching kinetics, and remain in contact with the lixiviant for extended periods during settling. In

contrast, coarser particles may face diffusion limitations and shorter contact times with the lixiviant during settling. As a result, an incomplete dissolution of manganese can be expected.

4.1.6 Density

The true density of the FMO slag sample was measured using the Micrometrics AccuPyc II 130 Gas Pycnometer. The helium pycnometer performed six measurements and calculated an average true density of 3.29 g/cm³ with a standard deviation of 0.0013 g/cm³. According to the XRF analysis, the slag mainly contains MnO, SiO_2, Al_2O_3, and CaO, with smaller amounts of other metal oxides. The initial density measurement will serve as a reference point as components dissolve during leaching and washing. Changes in density are also expected to affect settling.

4.2 Flocculant study

This section presents and discusses the results from the flocculant study, divided into two sub-sections: the flocculant screening study and the flocculant optimisation study. Marlyn Laboratory provided the flocculants and methods used in this section.

4.2.1 Flocculant screening study

The flocculant screening study was used to identify the most promising flocculant. Four of the eight flocculants provided by Marlyn Laboratory were selected based on their recommended pH ranges. The four flocculants, K6633, K300NH, K305A and K310A, were tested. The screening study was conducted at two flocculant dosages, 20 g/ton and 40 g/ton, and a control sample without a flocculant. Height-time profiles and turbidity measurements from the settling runs conducted at 20 g/ton are shown in Figure 18 and Figure 19, respectively. Height-time profiles and turbidity measurements from the settling runs conducted at 40 g/ton are shown in Figure 20 and Figure 21, respectively.

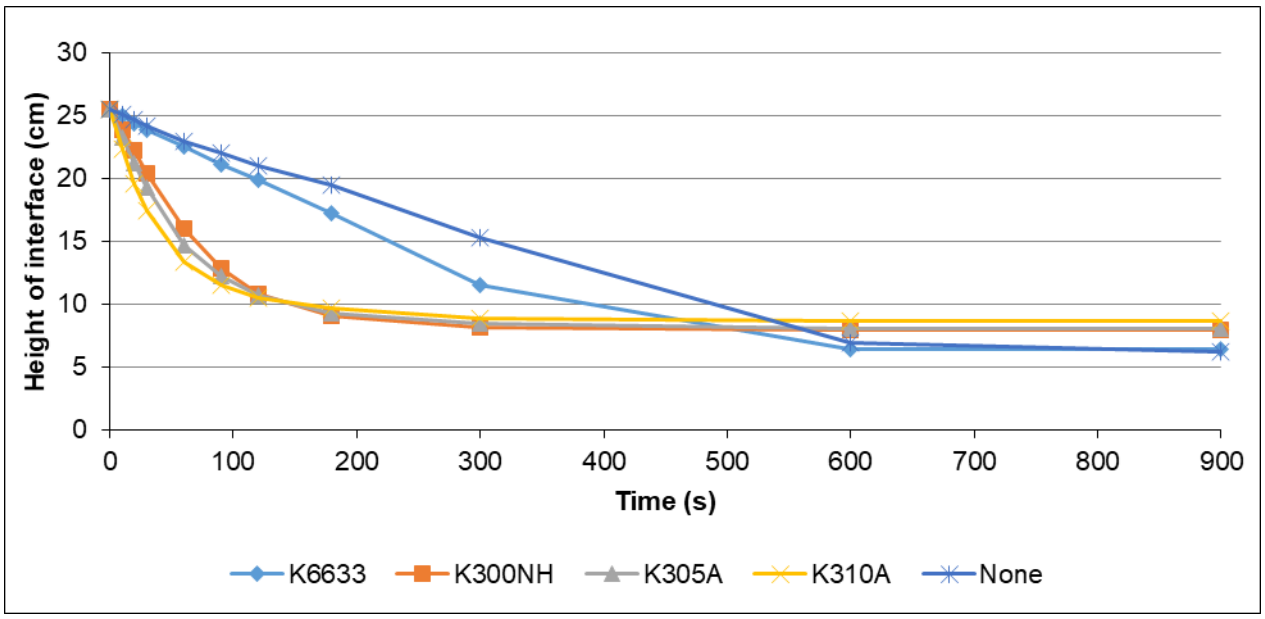

Figure 18: Height-time profiles by various flocculants at a dosage of 20 g/ton

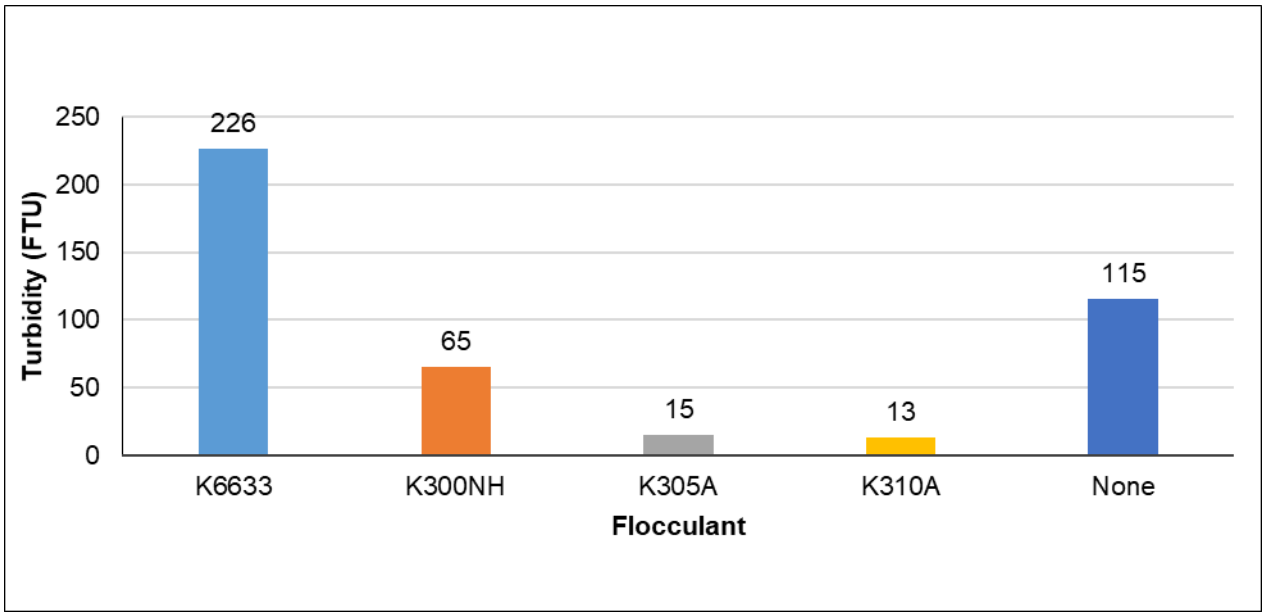

Figure 19: Turbidity measured after settling by various flocculants at a dosage of 20 g/ton

As shown in Figure 18, at a flocculant dosage of 20 g/ton, all flocculants demonstrated an improvement in slurry settling rate compared to the sample without a flocculant. Flocculant K310A slightly outperformed flocculants K305A and K300NH in settling rate and performed significantly better than flocculant K6633. As shown in Figure 19, flocculant K310A produces a lixiviant with a marginally lower turbidity of 13 FTU compared to flocculant K305A, which has a turbidity of 15 FTU. Flocculants K6633 and K300NH exhibit higher turbidity levels of 226 FTU and 65 FTU, respectively.

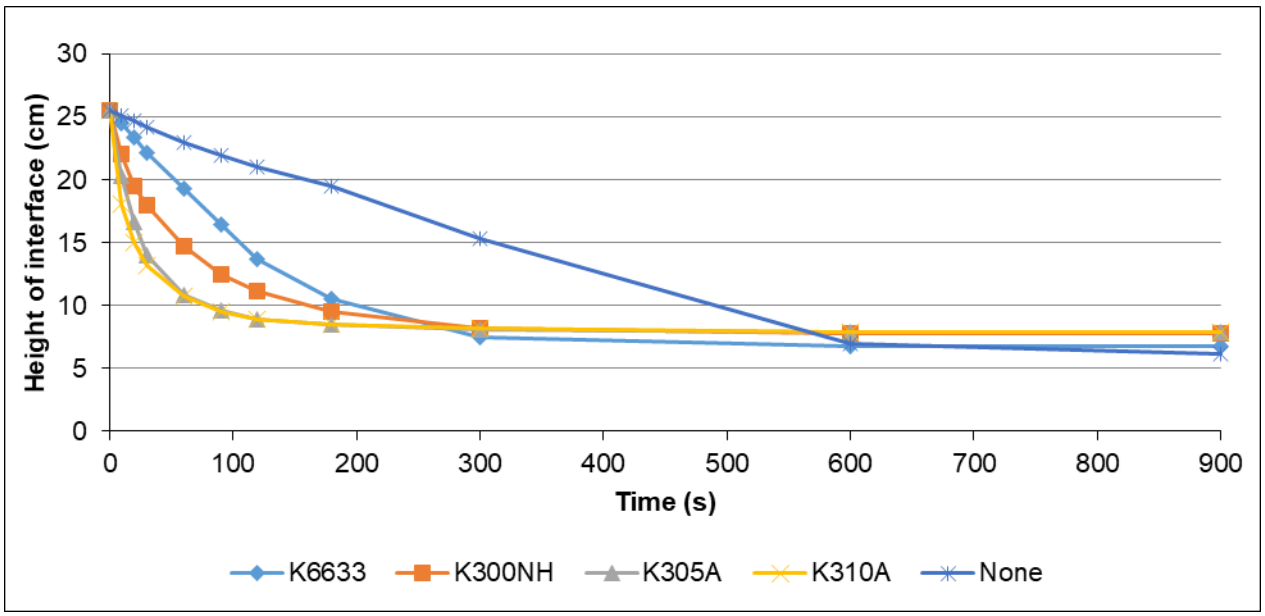

Figure 20: Height-time profiles by various flocculants at a dosage of 40 g/ton

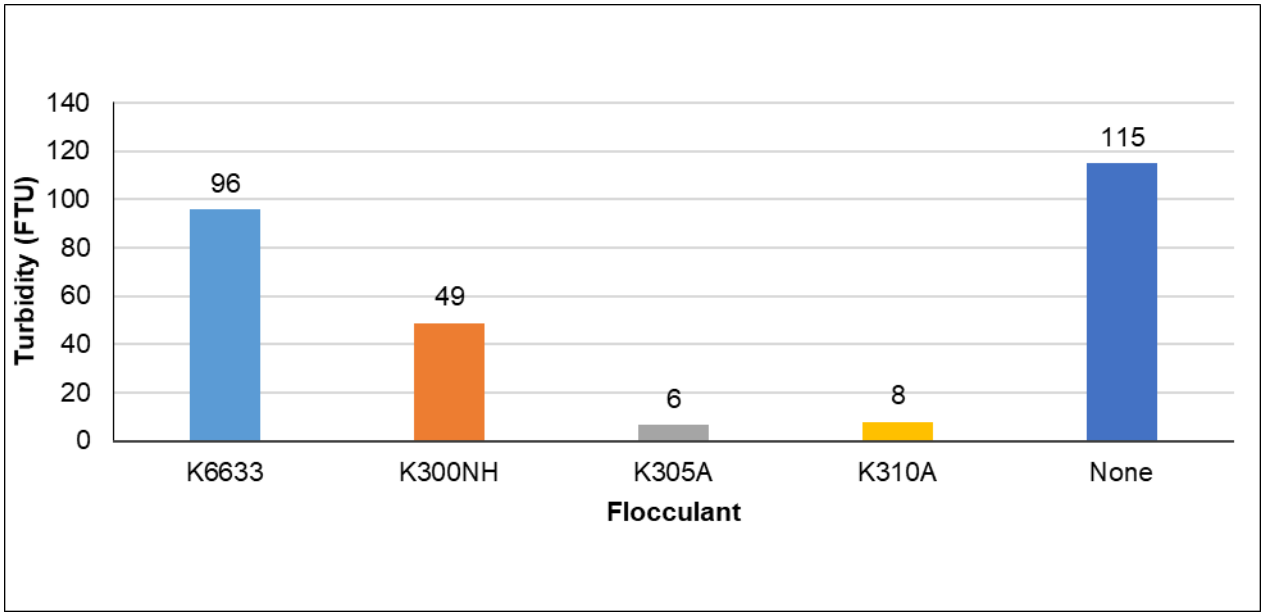

Figure 21: Turbidity measured after settling by various flocculants at a dosage of 40 g/ton

As shown in Figure 20, the overall settling rate of all four flocculants increased at a flocculant dosage of 40 g/ton compared to the 20 g/ton dosage. Flocculant K310A slightly outperformed flocculant K305A in settling rate and performed significantly better than flocculants K6633 and K300NH. As shown in Figure 21, a noticeable decrease in turbidity across all four samples is observed. Flocculant K305A produces a lixiviant with a marginally lower turbidity of 6 FTU compared to flocculant K310A, which has a turbidity of 8 FTU. Flocculants K6633 and K300NH exhibit higher turbidity levels of 96 FTU and 49 FTU, respectively.

Based on settling rate and turbidity, flocculant K310A was chosen for testing in the optimisation study. The screening results showed similar performance between flocculants K305A and K310A. Flocculant K310A slightly outperformed flocculant K305A with a marginally higher settling rate at both dosages. It also produced lower turbidity than K305A at the first dosage of 20 g/ton, but K305A produced lower turbidity at the second dosage of 40 g/ton. This reduction in turbidity caused by flocculant K305A was not considered significant enough to outweigh the increased settling rate achieved with flocculant K310A. Both flocculants K6633 and K300NH showed a considerably lower settling rate and higher turbidity at both dosages compared to flocculants K305A and K310A. The success of the anionic flocculants K305A and K310A indicates that the particles are positively charged, and this is confirmed by the acidic nature of the lixiviants.

4.2.2 Flocculant optimisation study

As identified in the flocculant screening study, flocculant K310A was the most promising candidate. In this section, an optimisation study was conducted using flocculant K310A to determine the ideal dosage. The optimisation involves ten dosages ranging from 5 g/ton to 50 g/ton, increasing in 5 g/ton steps, along with a control sample without flocculants. The initial settling rate (first 60 seconds), final bed height, and final turbidity measurements, as shown in Figure 22, Figure 23, and Figure 24, were used to identify the optimal flocculant dosage.

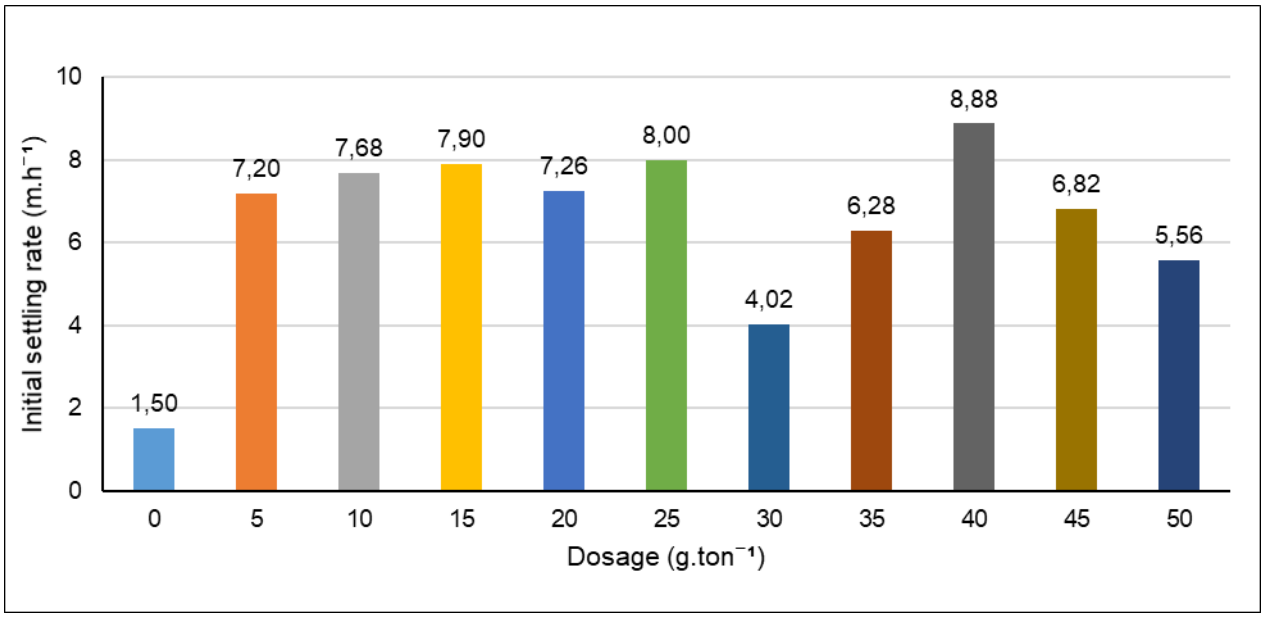

Figure 22: Initial settling rate (first 60 seconds) by flocculant K310A at various dosages (g/ton)

Figure 22 shows that the initial settling rate increases with flocculant dosage and peaks at 25 g/ton. The rate then decreases significantly at 30 g/ton and begins to rise again, attaining a new peak at 40 g/ton, after which it decreases once more as the flocculant dosage increases. The

sharp drop in the initial settling rate, followed by fluctuations after 25 g/ton, indicates over-flocculation [69].

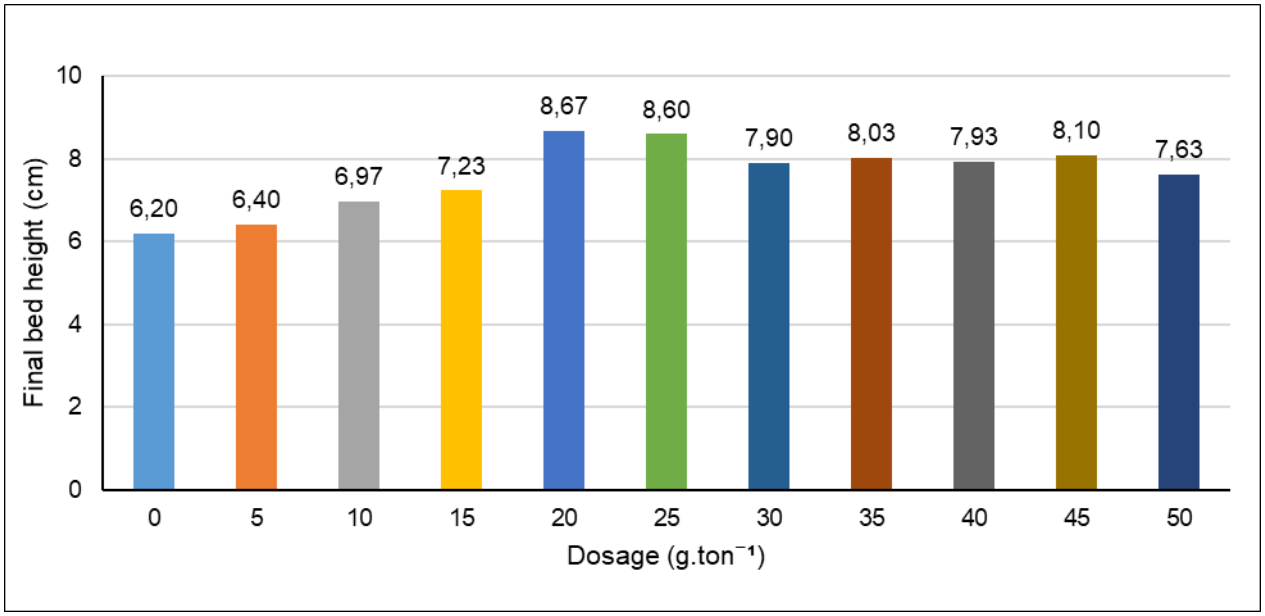

Figure 23: Final bed height by flocculant K310A at various dosages (g/ton)

As shown in Figure 23, the final bed height achieved by each settling run increased with an increase in flocculant dosage, and peaks at a flocculant dosage of 20 g/ton. The final bed height then shows an alternating trend with each increase in flocculant dosage. This inconsistent result could be attributed to over-flocculation. From the settling rate and final bed height data, it is clear that a higher settling rate results in a higher final bed height for the samples dosed with 0 to 25 g/ton flocculant.

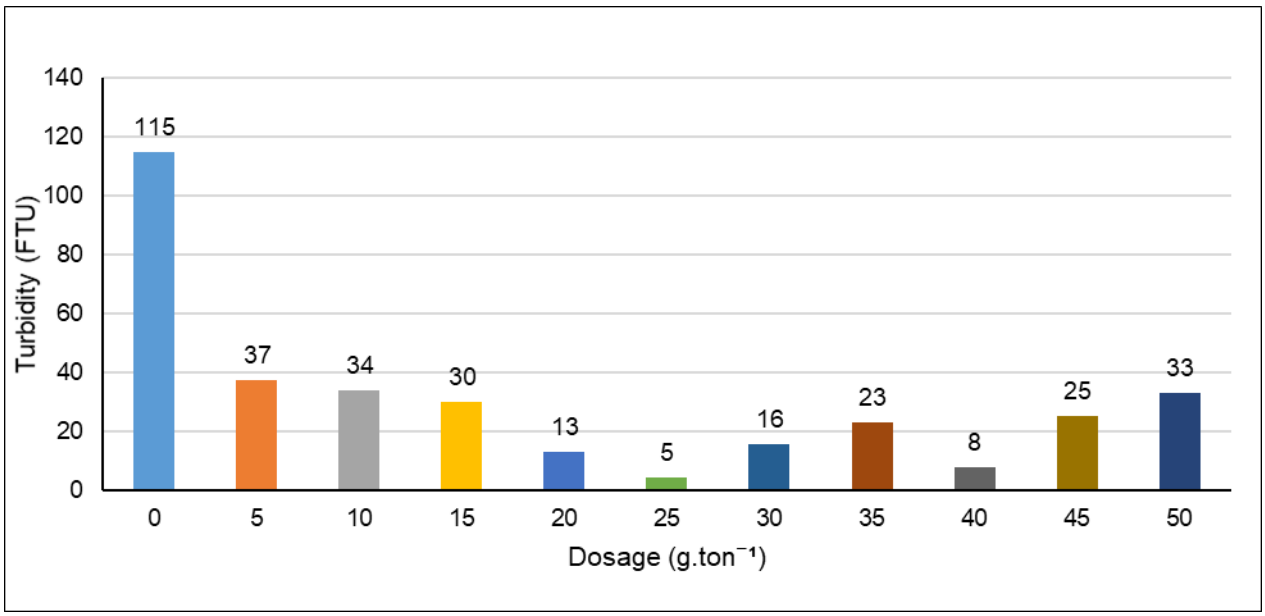

Figure 24: Turbidity measured after settling by K310A at various dosages (g/ton)

Figure 24 shows that turbidity decreases as the flocculant dosage increases, reaching its lowest value at 25 g/ton. Beyond this point, turbidity rises with further increases in flocculant dosage, with 40 g/ton acting as an outlier, having the second-lowest turbidity after 25 g/ton. The rising turbidity at higher dosages also indicates over-flocculation [69].

Considering both the initial settling rate and the final turbidity across all dosages, it is determined that 25 g/ton of flocculant K310A is ideal. At this level, a high initial settling rate and low turbidity are achieved without risking over-flocculation.

4.3 Leaching

This section presents the results of experiments conducted to determine the leaching and settling conditions for FMO slag by varying the sulphuric acid concentration and solid-liquid ratio. It also identifies optimal leaching recovery whilst ensuring suitable settling properties for subsequent tests.

4.3.1 Effect of sulphuric acid concentration on leaching and settling

The initial leaching experiments were performed at a solid-liquid concentration of 10 wt% and with sulphuric acid concentrations of 1, 2, 3, and 4%. The settling behaviour after 90 minutes is shown in Figure 25, and the leaching results of the target metals, manganese and lithium, are shown in Table 16.

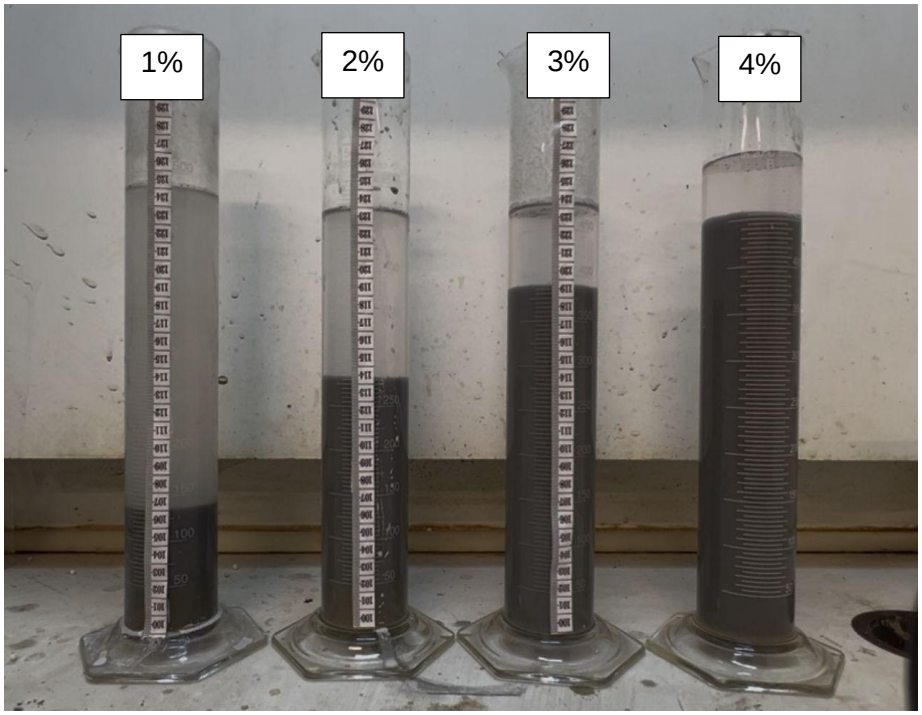

Figure 25: Visual assessment of the settling behaviour of FMO slag at 1, 2,3 and 4% H_2SO_4 solutions after 90 minutes

Table 16: H_2SO_4:Mn ratio, Mn recovery, and Li recovery from FMO slag leached with varying acid concentrations

H_2SO_4 (v/v)	H_2SO_4:Mn (mol/mol)	Mn recovery (%)	Li recovery (%)
1%	0.55:1	31,13%	31,17%
2%	1.11:1	59,57%	63,57%
3%	1.66:1	81,04%	85,07%
4%	2.22:1	87,61%	96,12%

The visual assessment in Figure 25 showed a correlation between increased sulphuric acid concentration and the formation of a gel-like phase, which significantly hindered settling. The slurry treated with a 1% sulphuric acid solution settled, reaching a final bed concentration of 43.9 wt%. This indicated that settling was less impeded than the slurries treated with 2, 3, and 4% sulphuric acid solutions, which achieved final bed concentrations of 16.6 wt%, 12.4 wt%, and 11.5 wt%, respectively.

Despite its superior settling performance, leaching with a 1% sulphuric acid solution results in limited recovery of manganese and lithium. As shown in Table 16, the decrease in sulphuric acid concentration results in a lower recovery. The 1% sulphuric acid solution can leach only 55% of

the manganese from the FMO slag sample, stoichiometrically. As a result, only a 31.13% manganese recovery was achieved. The 1% sulphuric acid solution only recovered 31.17% of the lithium. Since increasing the sulphuric acid concentration is not possible due to gel formation, changing the solid-liquid ratio was investigated.

4.3.2 Effect of solid-liquid ratio on leaching and settling

The poor manganese recovery at a solid-liquid ratio of 10 wt% and a sulphuric acid concentration of 1% prompted the investigation of varying the solid-liquid ratio while maintaining the 1% sulphuric acid solution. Decreasing the solid-liquid ratio increased the amount of sulphuric acid per manganese atom. The solid-liquid ratios tested were 10, 5 and 3.3 wt%, which have a H_2SO_4: Mn ratio of 0.55:1, 111:1 and 1.66:1, respectively. The manganese and lithium recovery using the three different solid-liquid ratios is shown in Table 17.

Table 17: H_2SO_4: Mn ratio, Mn recovery, and Li recovery from FMO slag leached with 1% H_2SO_4 at varying solid-liquid ratios

S/L ratio	H_2SO_4:Mn (mol/mol)	Mn recovery (%)	Li recovery (%)
10 wt%	0.55:1	31,13%	31,17%
5 wt%	1.11:1	57,29%	60,61%
3.3 wt%	1.66:1	78,48%	82,57%

As shown in Table 17, manganese and lithium recovery improved as the solid-liquid ratio decreased. After the leaching step, the slurry's settling properties were evaluated, both with and without a flocculant. The height-time graphs of the three slurries, with a solid-liquid ratio of 3.3, 5 and 10 wt%, without a flocculant and with a flocculant, are shown in Figure 26 and Figure 27, respectively.

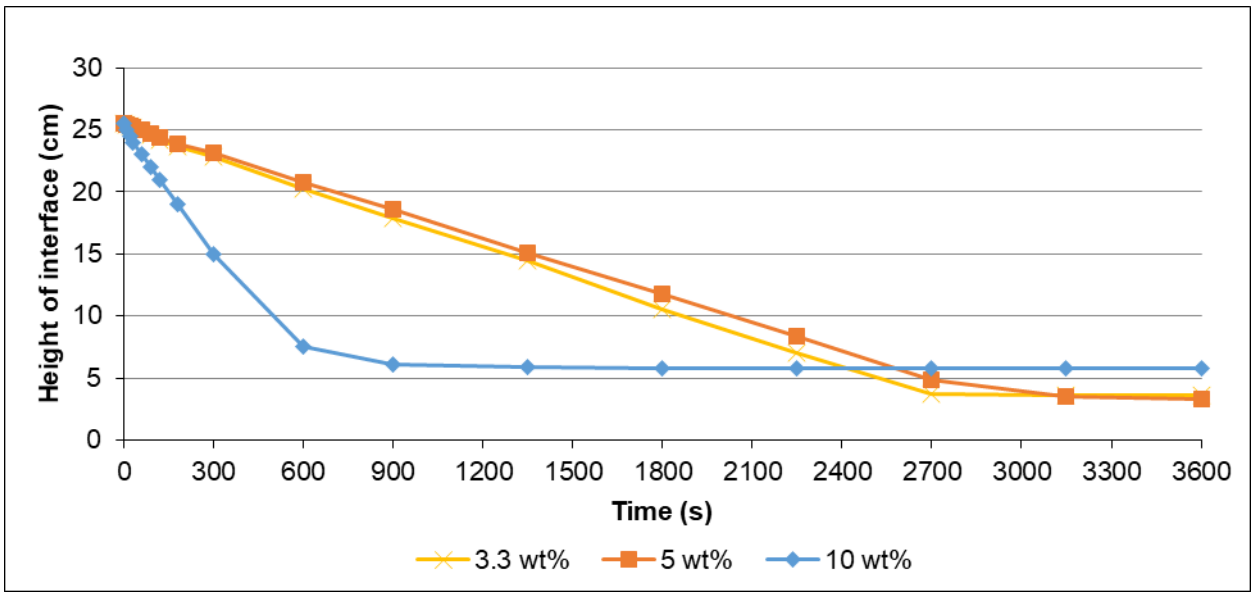

Figure 26: Height-time profile of leached FMO slag at varying solid-liquid ratios in 1% H_2SO_4 solution

Figure 26 shows that without using a flocculant, all three solid-liquid ratios settle without a gel-like phase. However, the 5 wt% and 3.3 wt% solid-liquid ratio slurries settle at a considerably slower rate than the 10 wt% solid-liquid ratio slurry. The three solid-liquid ratios 3.3, 5 and 10 wt% achieved a final bed concentration of 23.4, 38.6 and 43.9 wt%, respectively.

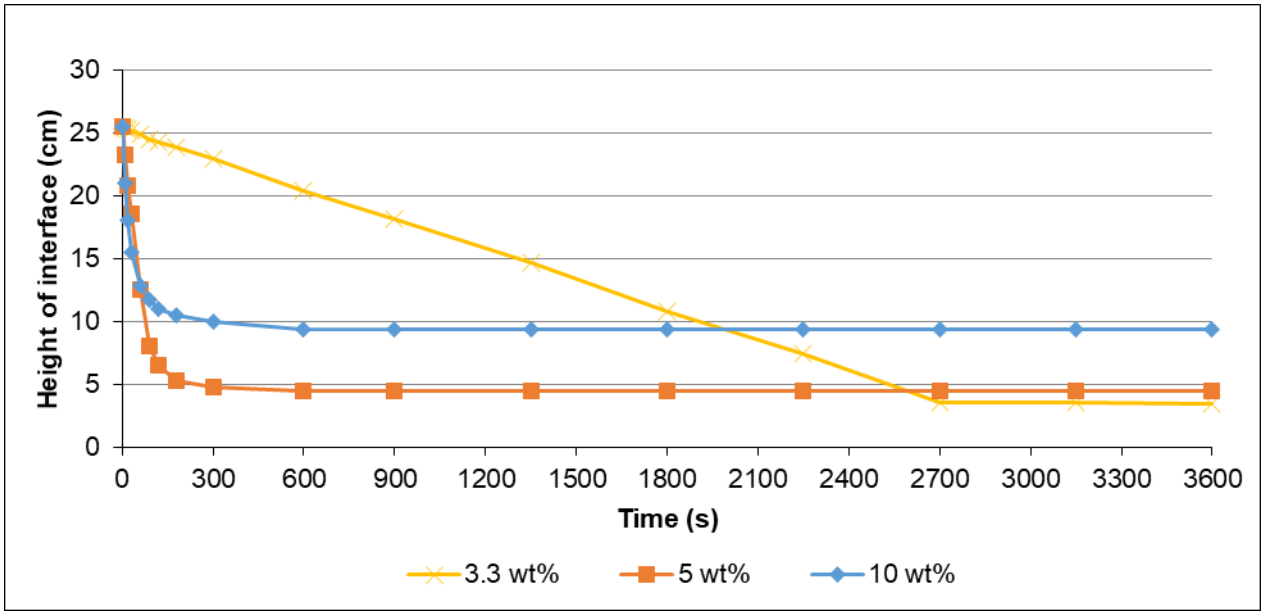

Figure 27: Height-time profile of leached FMO slag at varying solid-liquid ratios in 1% H_2SO_4 solution with 25 g/ton K310A flocculant

As shown in Figure 27, after adding flocculant K310A, the settling rate of the slurries with 10 wt% and 5 wt% solid-liquid ratios improved significantly. The slurry with a 10 wt% solid-liquid ratio increased its initial settling flux from 162.3 kg/h/m² to 1203.1 kg/h/m². Similarly, the slurry with a

5 wt% solid-liquid ratio increased from 16.5 kg/h/m² to 1115.6 kg/h/m². However, the 3.3 wt% solid-liquid slurry showed no significant change in settling rate; its initial settling flux increased slightly from 12.4 kg/h/m² to 13.8 kg/h/m². The three solid-liquid ratios- 3.3 wt%, 5 wt%, and 10 wt%- achieved final bed concentrations of 24.0, 28.3, and 27.1 wt%, respectively. It is concluded that adding a flocculant significantly enhances the settling rate but reduces the final bed concentration of the 10 wt% and 5 wt% slurry. Conversely, adding a flocculant had little to no effect on the settling rate and final bed concentration of the 3.3 wt% slurry.

Accounting for both the leaching and settling characteristics, the 5 wt% solid-liquid ratio slurry was selected for the following experimental work. This solid-liquid ratio provides increased manganese recovery of 59.27% compared to the original 31.13% and increased lithium recovery of 60.61% compared to the original 31.17% for the 10 wt% solid-liquid ratio, and maintains good settling characteristics when a flocculant is added.

4.3.3 EDX analysis of different settling layers

During the initial settling tests, four distinct settling layers were observed, as illustrated in Figure 28. EDX analysis was used to determine the surface chemistry of the four layers.

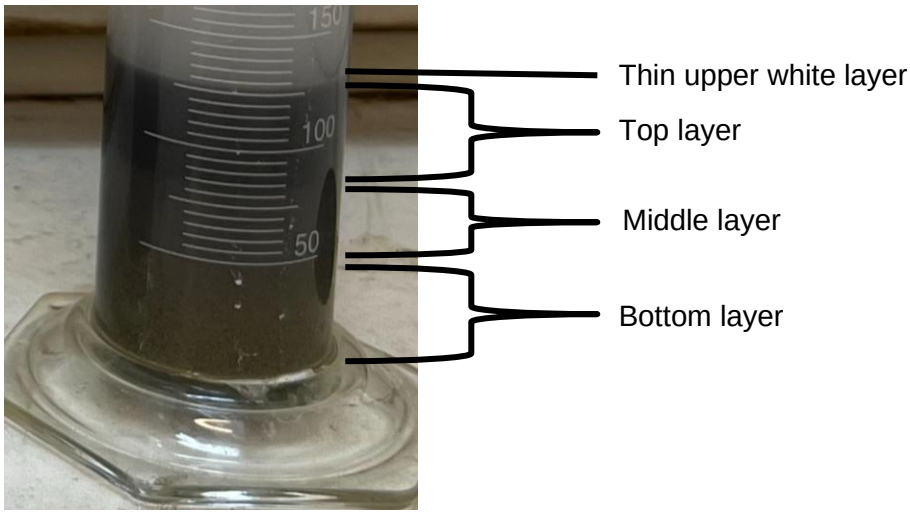

Figure 28: Four layers formed by settling

The bottom layer was dark green, consisted of larger particles, and settled in the bed with the highest solid-liquid ratio. The middle layer was dark green/grey and appeared to be a mixture of the top and bottom layers, composed of large to mid-sized particles. The top layer was a dark grey, consisted of smaller particles, and settled in the bed with a lower solid-liquid ratio than the bottom layer. The thin, upper white layer was distinct, white/grey, and formed on top of the bed.

After decantation, the four layers were washed and dried, and EDX analysis was performed. The EDX data for the four samples and the original slag sample are shown in Table 18.

Table 18: EDX analysis of 4 settling layers compared to original slag

Element	Original sample (%)	Bottom layer (%)	Middle layer (%)	Top layer (%)	Thin upper white layer (%)
O	40.8	53.7	53.5	59.1	59.7
Mn	24.9	10.5	9.8	1.3	0.7
Ca	10.3	6.7	7.9	1.2	29.9
Si	10.3	15.6	15.3	25.6	6.4
Al	10.1	12.5	12.4	12.3	3.1
Mg	2.0	1.0	1.1	0.5	0.0
Fe	1.6	0.0	0.0	0.0	0.0

EDX analysis provides information about approximately 1 to 3 microns of the slag sample's surface. Table 18 shows that the EDX analysis of the bottom and middle layers showed similar results. The manganese content was significantly lower in both layers than in the original slag sample. In contrast, silicon and aluminium showed a slight increase, indicating resistance to dissolution. The calcium content in both layers also decreased slightly. The top layer's manganese and calcium content were very low, indicating almost complete dissolution of these elements. The top layer also contained a higher proportion of the whole of silicon and aluminium than the original sample, indicating resistance to dissolution. The thin upper white layer mainly comprises calcium, with small amounts of silicon and aluminium. The white colour and high proportion of calcium suggest that this layer is a precipitate.

Several conclusions can be drawn from this section. Smaller particles in the top layer exhibit nearly complete dissolution of manganese and calcium. Larger particles in the middle and bottom layers show partial dissolution of manganese and calcium, limited by diffusion constraints. Additionally, it can be concluded that manganese and calcium undergo significant dissolution, whereas silicon and aluminium show resistance to dissolution under these conditions. Calcium also tends to precipitate out.

4.4 Settling tests

This section presents and discusses the results obtained from various settling experiments aimed at understanding the settling behaviour of FMO slag. Settling tests were conducted under four different conditions relevant to the CCD process. These conditions include settling in water, settling after leaching, settling after leaching with a flocculant, and settling at CCD conditions. Both 5 wt% and 10 wt% solid-liquid ratios were examined in all experiments. The 5 wt% ratio was

selected for its good leaching properties, while the 10 wt% ratio was chosen for its excellent settling characteristics.

4.4.1 Settling in water

In this section, the inherent settling characteristics of FMO slag were established by settling it in deionised water. Settling under these conditions allows characterisation of settling without changes in density, viscosity, particle shape, particle size, chemical composition, ionic strength, or surface charge.

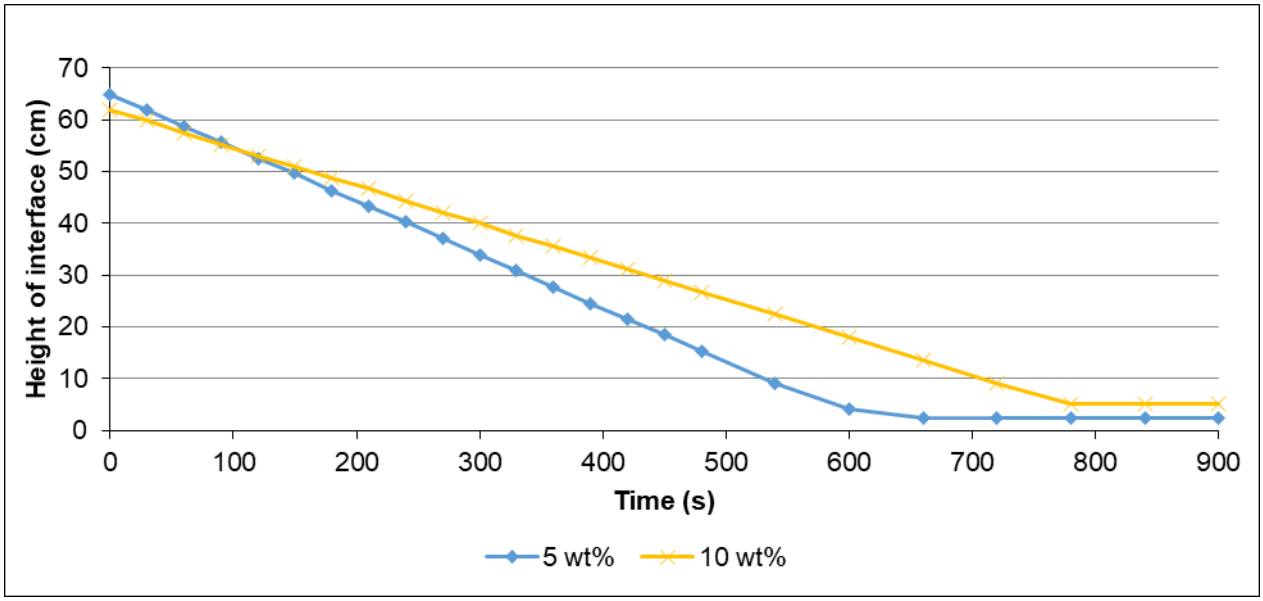

Figure 29: Height-time profile of FMO slag settling in water at 5 wt% and 10wt%

The settling behaviour of the two slurries with different solid-liquid ratios is as expected. As shown in Figure 29, the 5 wt% solid-liquid ratio slurry settled with the faster initial settling rate of 3.72 m/h compared to the 10 wt% slurry with an initial settling rate of 2.65 m/h. The 5 wt% slurry reached a final bed height of 2.3 cm, approximately half the 10 wt% slurry final bed height of 5.1 cm.

4.4.2 Settling after leaching

In this section, the settling behaviour of FMO slag after leaching was investigated without the aid of a flocculant. This data serves as a baseline and can be referenced if settling is compromised in a continuous process, which could indicate flocculant inhibition. The slurries used in this section were prepared as described in section 3.2.2. of this report. The height-time profile of the sulphuric acid-leached FMO slag at solid-liquid ratios of 5 wt% and 10 wt% is shown in Figure 30.

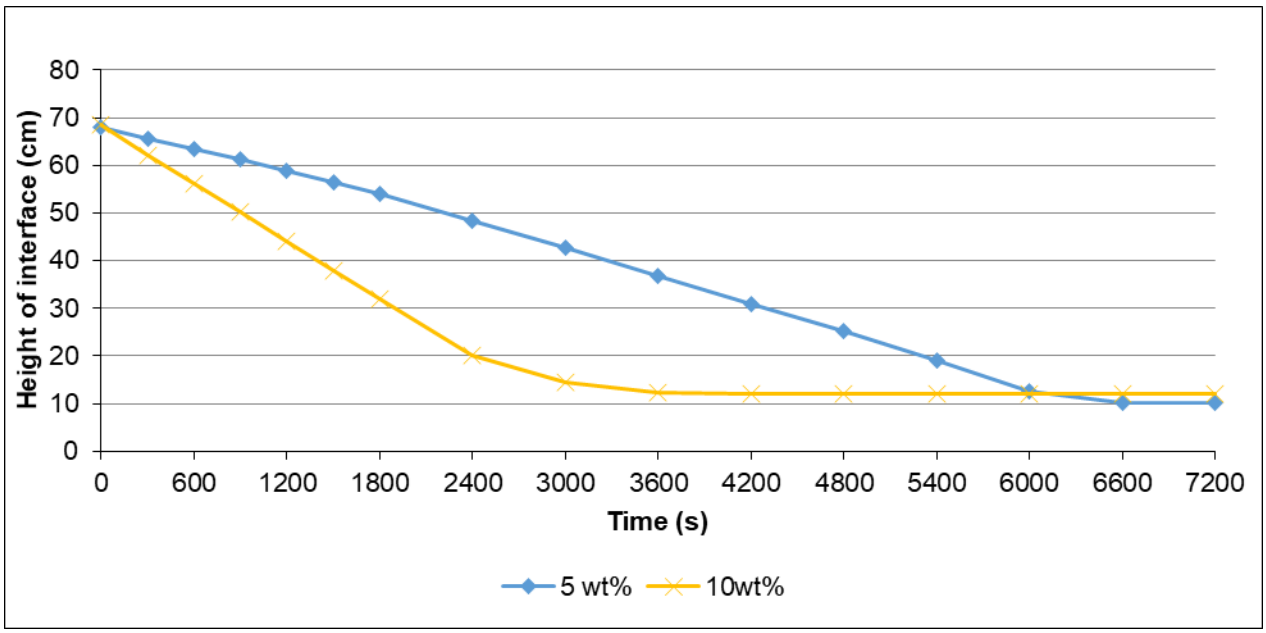

Figure 30: Height-time profile of sulphuric acid-leached FMO slag at 5 wt% and 10 wt%

As shown in Figure 30, the 10 wt% solid-liquid ratio slurry settled with the faster initial settling rate of 0.73 m/h compared to the 5 wt% slurry with an initial settling rate of 0.28 m/h. These findings are consistent with the initial findings from the leaching test, section 4.3.2. of this report, where the 10 wt% slurry also showed superior settling compared to the 5 wt% slurry. Changes in density, viscosity, particle shape, particle size, chemical composition, ionic strength or surface charge account for the significant decrease in settling rate observed by first leaching the slag with sulphuric acid.

4.4.3 Settling after leaching in the presence of a flocculant (pre-thickener)

Similar to the previous section, leached FMO slag was settled, but with the addition of a pre-determined flocculant and dosage. Before settling, the 5 wt% and 10 wt% solid-liquid ratio slurries were dosed with 25 g/ton of flocculant K310A. This data indicates the expected settling performance under operating conditions with a flocculant. It also helps to directly size the pre-thickener to separate the pregnant leach solution from the thickened slurry after the leaching phase. The height-time profile of sulphuric acid leached FMO slag with flocculant at solid-liquid ratios of 5 wt% and 10 wt% is shown in Figure 31. The corresponding flux-concentration plots of

the 10 wt% and 5 wt% solid-liquid ratio slurries are presented in Figure 32 and Figure 33, respectively.

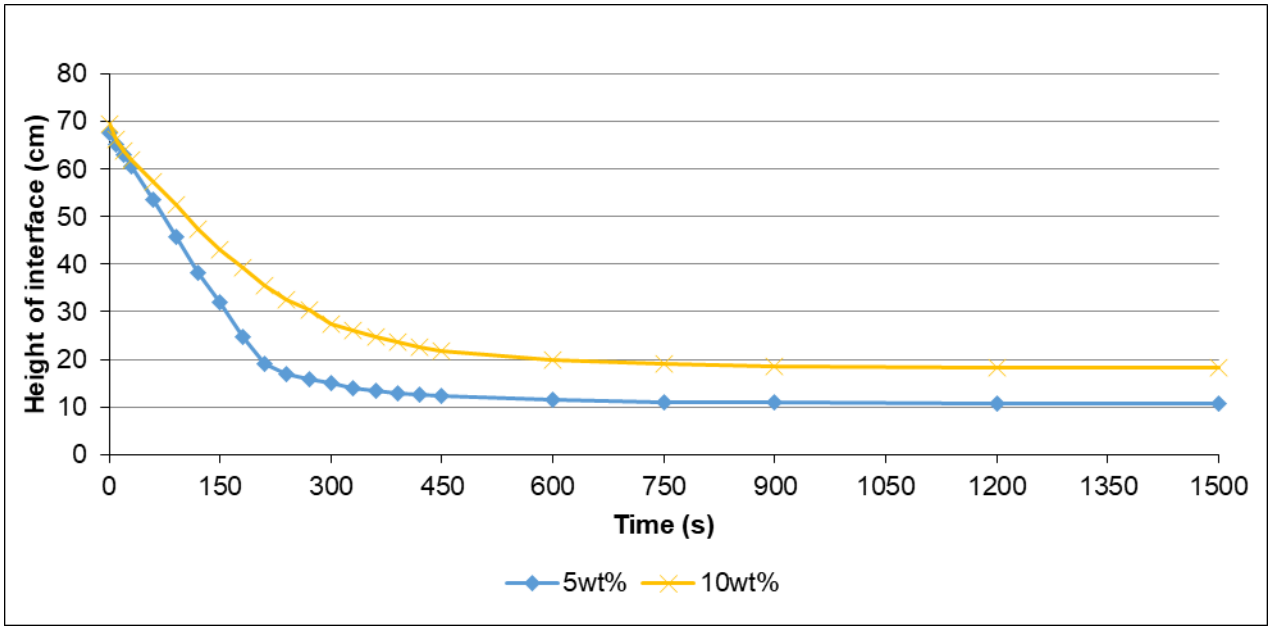

Figure 31: Height-time profile of sulphuric acid-leached FMO slag with flocculant at 5 wt% and 10 wt%

As shown in Figure 31, adding a flocculant significantly enhanced the settling rate for both the 5 wt% and 10 wt% samples, with initial settling rates of 8.52 m/h and 5.55 m/h, respectively, compared to the unflocculated experimental runs. The slurry with a 5 wt% solid-liquid ratio exhibited the fastest settling rate, indicating that the flocculant was particularly effective at this lower solid concentration. These results align with the initial findings from the leaching test, section 4.3.2. of this report, where the 5 wt% slurry also demonstrated a superior settling rate compared to the 10 wt% slurry when flocculated.

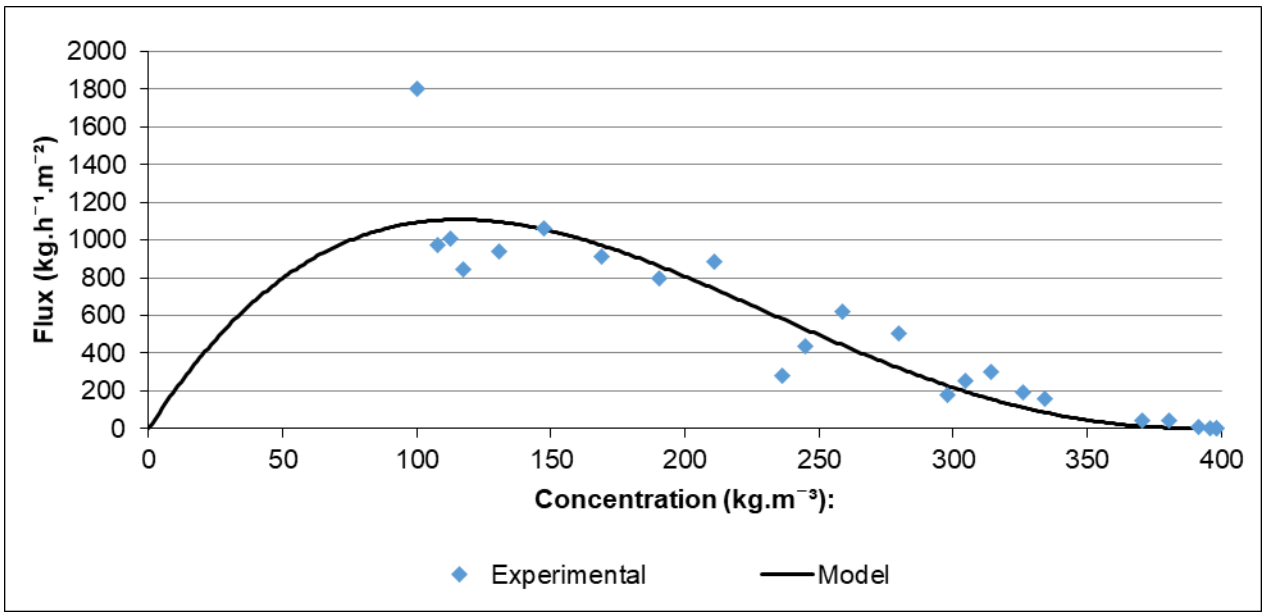

Figure 32: Flux-concentration plot for sulphuric acid-leached FMO slag with flocculant at 10 wt%: Model and experimental data

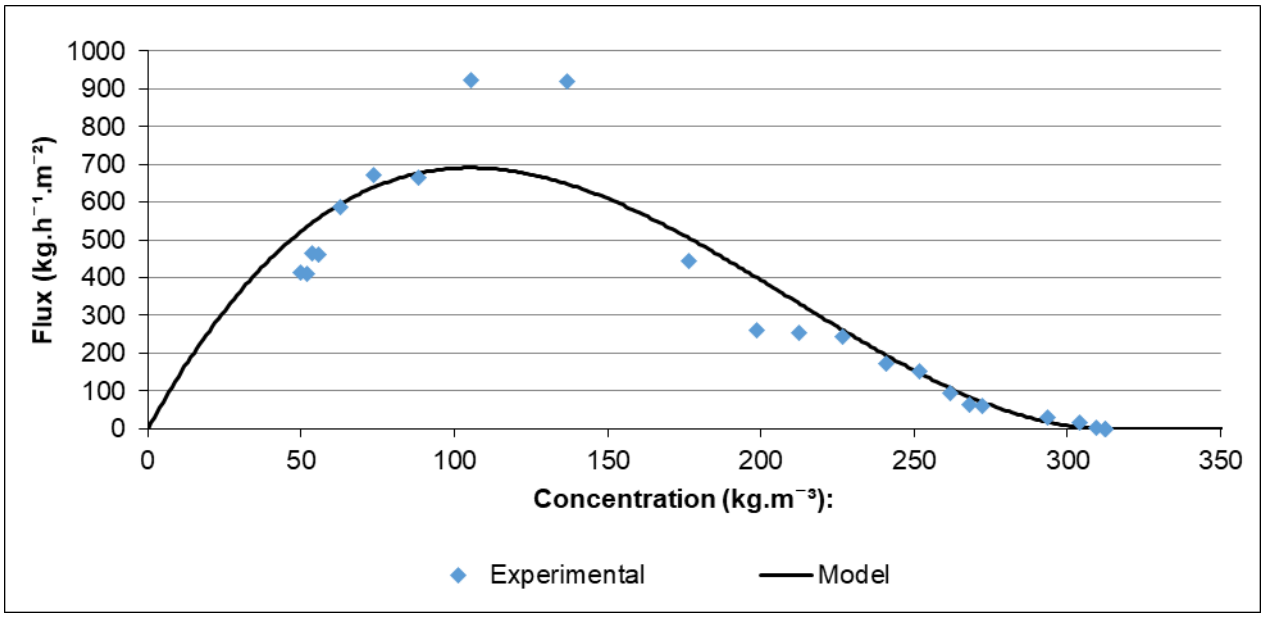

Figure 33: Flux-concentration plot for sulphuric acid-leached FMO slag with flocculant at 5 wt%: Model and experimental data

Flux-concentration curves were constructed using data from the height-time profile, and a model was fitted. Figure 32 and Figure 33 show that, using a model as a reference, the 5 wt% and 10 wt% slurries have maximum fluxes of 691 kg/h/m² and 1109 kg/h/m², respectively. The figures also indicate that the 5 wt% and 10 wt% slurries reach final maximum bed concentrations of 312 kg/m³ and 398 kg/m³, respectively. This data suggests that the 10 wt% slurry still exhibits superior settling characteristics, with higher maximum flux and final bed concentration, despite the faster

settling rate achieved by the 5 wt% slurry. The K and m values for these two runs are shown in Table 19.

Table 19: Model constants for settling runs of sulphuric acid-leached FMO slag with flocculant

Solid-liquid ratio	5 wt%	10 wt%
K	4608,68	8823,23
m	1,97	2,44

The K parameter determines the overall magnitude of the flux curve. A larger K value means that, for a given concentration, the system can sustain a higher settling flux. The m parameter influences the shape of the flux curve near high concentrations. A higher m value indicates that the flux drops more sharply as the concentration approaches the maximum solid concentration. From the K and m parameters shown in Table 19, it is concluded that the 10 wt% run has a significantly higher K value than the 5 wt% run and can produce a considerably larger flux. The 10 wt% run also has a higher m value than the 5 wt% run, which indicates that its flux decreases more sharply as the concentration approaches the maximum solid concentration.

Chapter 5: Settling at CCD conditions

This section presents and discusses the results obtained from settling leached products under CCD conditions. The experimental setup involved producing intermediate lixiviant and FMO slag samples. The intermediate products were then mixed and allowed to settle to simulate countercurrent flow within a CCD system. This method enables the simulation of a countercurrent system using batch processes. Three experiments were conducted, two at 10 wt% and one at 5 wt%. Three CCD stages were simulated for each experiment, and corresponding height-time profiles were gathered for each stage.

5.1 CCD washing efficiency

The washing efficiency of the CCD system is based on the recovery of entrained lixiviant from the slurry phase. The CCD settling runs were conducted so that each thickener produced a thickened 30 wt% slurry. The washing step efficiency of a three-stage CCD system operating at a starting solid-liquid ratio of 5 wt% and 10 wt% is shown in Table 20.

Table 20: Washing step recovery of a three-stage CCD at 5 wt% and 10 wt%

Solid-liquid ratio	Washing efficiency
5 wt%	99,65%
10 wt%	97,22%

As shown in Table 20, both the 5 wt% and 10 wt% solid-liquid ratio slurries have a theoretical washing efficiency that is highly efficient. Since a dilute sulfuric acid solution is used within the CCD system, leaching occurs. This additional leaching increases the manganese within Lix[3], decreasing the apparent washing efficiency.

5.2 CCD run with a solid-liquid ratio of 10 wt%

5.2.1 Settling

The height-time profile of the three CCD stages, tested by mixing and settling intermediate lixiviants and FMO slag samples, is displayed in Figure 34. The corresponding flux-concentration plots for the first, second, and third CCD stages are shown in Figure 35, Figure 36, and Figure 37, respectively. Each flux-concentration plot is constructed using data gathered from the height-time profiles and fitted with a model.

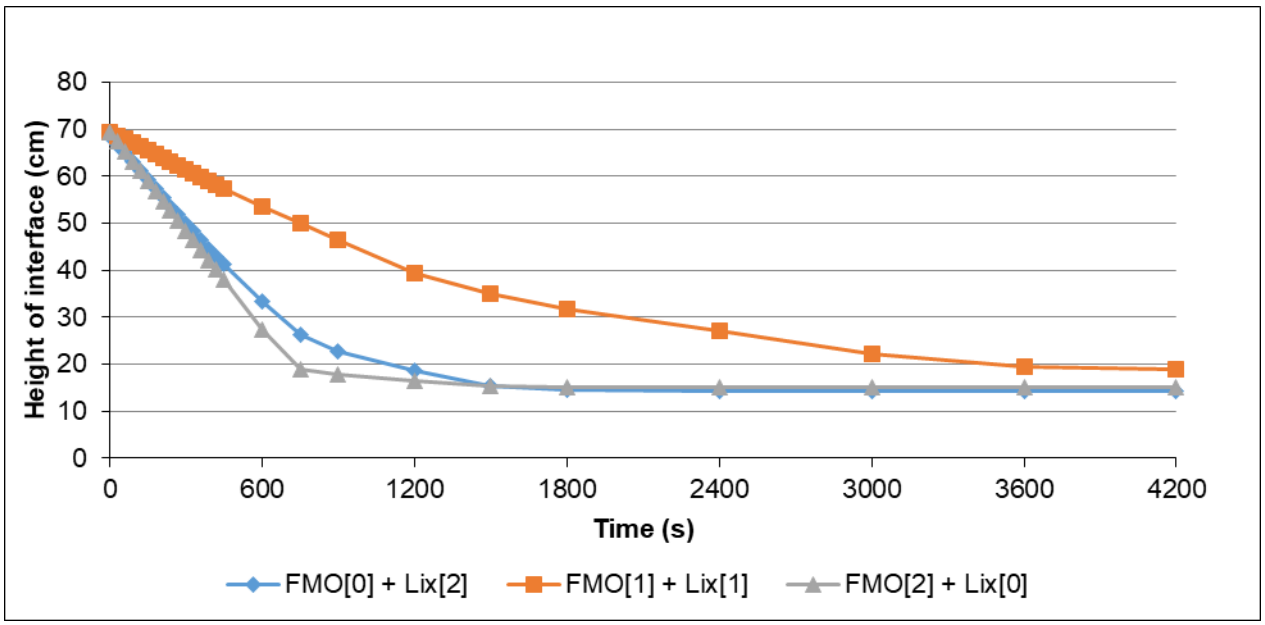

Figure 34: Height-time profile for the three stages of a CCD system for the first run at 10 wt%

The height-time profiles of the three CCD stages are shown in Figure 34. In the first CCD stage, using the intermediate products FMO[0] and Lix[2], the initial settling rate of 2.23 m/h is slower than the flocculated settling rate of 5.55 m/h performed in section 4.5.3. However, it remains significantly faster than the unflocculated settling rate of 0.73 m/h carried out in section 4.5.2. This suggests that the conditions in the first CCD stage hinder settling, yet the flocculant remains effective. In the second CCD stage, using the intermediate products FMO[1] and Lix[1], the initial settling rate of 0.96 m/h is significantly slower than the flocculated rate and is closer to the unflocculated rate. This indicates that conditions within the second CCD stage are hindered and that the flocculant is largely ineffective. In the third CCD stage, using the intermediate products FMO[2] and Lix[0], the initial settling rate of 2.52 m/h is slower than the flocculated performance. Still, it remains considerably faster than the unflocculated performance. This implies that the conditions within the third CCD stage hinder settling, but the flocculant remains effective. Overall, the settling performance of both the first and third CCD stages is quite similar, whereas settling is impeded in the second CCD stage.

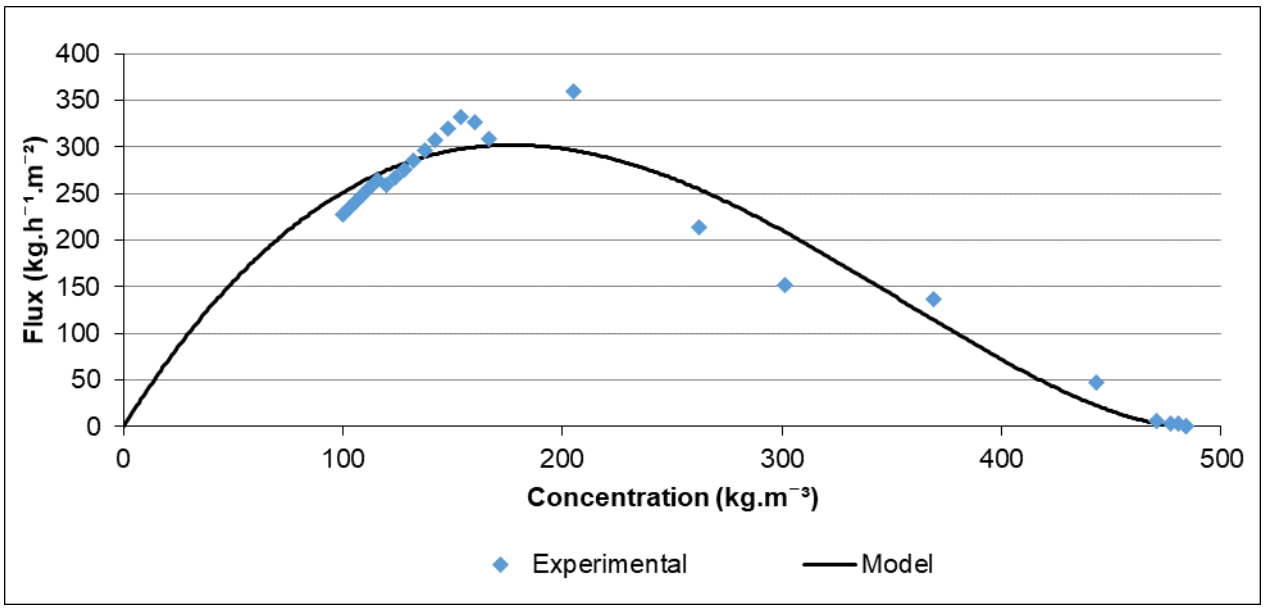

Figure 35: Flux-concentration plot for the first settling stage of a CCD system using intermediate products FMO[0] and Lix[2], for the first run at 10 wt%: Model and experimental data

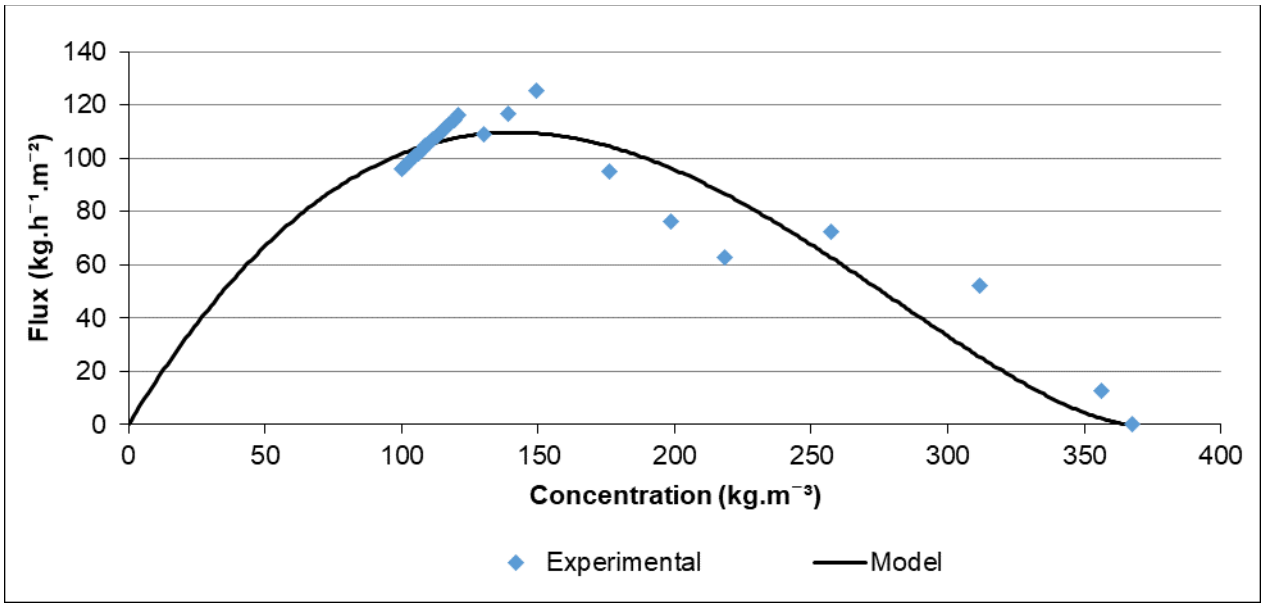

Figure 36: Flux-concentration plot for the second settling stage of a CCD system using intermediate products FMO[1] and Lix[1], for the first run at 10 wt%: Model and experimental data

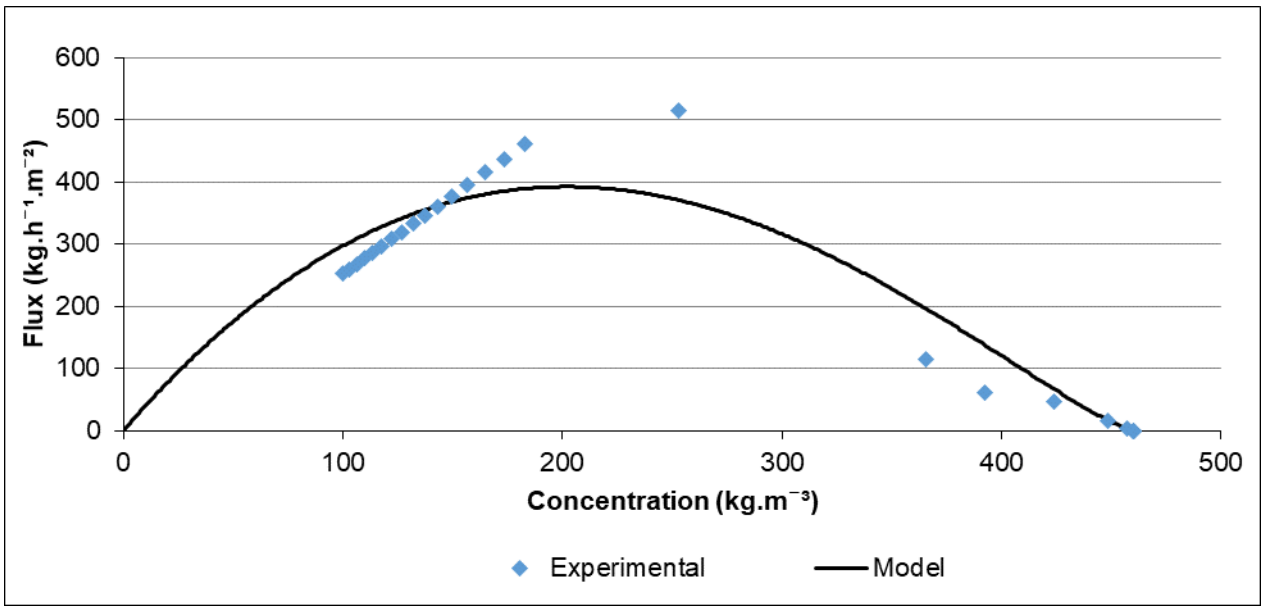

Figure 37: Flux-concentration plot for the third settling stage of a CCD system using intermediate products FMO[2] and Lix[0], for the first run at 10 wt%: Model and experimental data

As shown in Figure 35, Figure 36 and Figure 37, using a model as reference, the first, second and third CCD stages have maximum fluxes of 301.9 kg/h/m^2, 109.6 kg/h/m2 and 392.2 kg/h/m^2, respectively. The figures also indicate that the first, second and third CCD stages reach final maximum bed concentrations of 483.8 kg/m^3, 367.7 kg/m^3 and 460.3 kg/m^3, respectively. The K and m values for the three CCD stages are shown in Table 21.

Table 21: Model constants for the three CCD stages at 10 wt%

CCD stage	1	2	3
K	1817,52	623,56	1872,08
m	1,73	1,61	1,28

From the K and m parameters shown in Table 21, it is concluded that CCD 3 exhibits the highest K value, followed closely by CCD 1, while CCD 2 has the lowest K value. This indicates that CCD 3 and 1 can produce higher overall settling fluxes than CCD 2. CCD 1 and 2 also have higher m values than CCD 3, which indicates that their flux curves drop off more sharply as the concentration approaches the maximum solid concentration. The effects of K and m are evident in the flux-concentration curves. The physical phenomenon observed in stage two can be attributed to a lower ionic strength.

5.2.2 Lixiviant and slurry analysis

A lixiviant sample was collected before and after each of the three settling stages. Each sample represents a different stage of the CCD system. All samples were analysed for turbidity, viscosity,

density, and pH. The physicochemical properties of the lixiviants are summarised in Table 22. Slag samples were also collected at three stages: one before the leaching stage, another after the leaching stage, and the final after the CCD stage. Each slag sample was analysed for PSD and density. The PSD and density results summary is presented in Table 23, and the PSD is shown in Figure 38.

Table 22: Physicochemical properties of lixiviant from settling test in the first run at 10 wt%

Lixiviant	Turbidity (FTU)	Viscosity (mPa.s)	Density (g/cm^3)	pH
Lix[3]	33.4	0.9134	1.0094	4.06
Lix[2]	53	0.8919	1.0066	3.71
Lix[1]	121	0.9635	1.0061	3.50
Lix[0]	-	0.8919	0.9992	1.04

The four lixiviant properties, turbidity, viscosity, density, and pH, are shown in Table 22. The turbidity decreased from Lix[1] to Lix[3], indicating progressive clarification of the lixiviant as it moves through the CCD system. Since Lix[3] acts as the PLS produced by the CCD system, lower turbidity is a positive sign for downstream processing. Reduced turbidity will lessen the load on subsequent purification steps. The viscosity measurements did not reveal any consistent pattern of change between the lixiviant samples. Additionally, no significant variation in viscosity was observed, with the most notable change being an 8.03% increase in Lix[1] relative to the initial wash liquid, Lix[0]. This suggests that the concentration of dissolved metals in the lixiviants does not significantly affect fluid resistance to flow within the CCD range. The density of the lixiviants increased from Lix[0] to Lix[3], which is expected as more metal species dissolve from the slag into the lixiviant at each CCD stage. Consequently, the rise in dissolved metals contributes to increased lixiviant density. The pH of the lixiviant also increases from Lix[0] to Lix[3]. This rise in pH indicates the consumption of sulphuric acid as metal species are dissolved into the lixiviant. The most substantial pH increase occurs from Lix[0] to Lix[1], suggesting that most acid consumption occurs within the third CCD stage.

Table 23: PSD and density of FMO slag at different stages of the settling and leaching process in the first run at 10 wt%

Solid sample	PSD			Density
	d_{10} (µm)	d_{50} (µm)	d_{90} (µm)	(g/cm^3)
Slag	8.5	52	123	3.2895
FMO[0]	13.2	50.5	124	2.9997
FMO[3]	12.1	49.9	125	2.9347

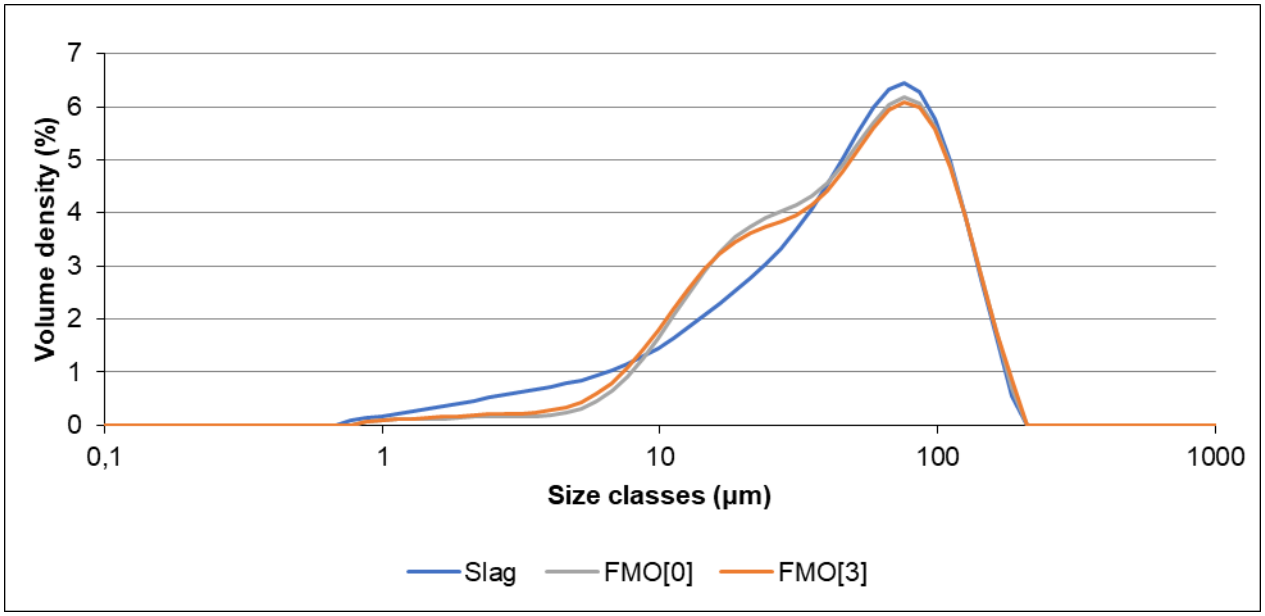

Figure 38: PSD of FMO slag at different stages of the settling and leaching process in the first run at 10 wt%

The density of the FMO slag at different stages is shown in Table 23. The density decreased from 3.2895 g/cm³ to 2.9997 g/cm³ during the leaching phase and dropped to 2.9347 g/cm³ during the CCD phase. This decline indicates the dissolution of denser components within the FMO slag, leaving behind the less dense materials.

The PSD, d_{10}, d_{50}, and d_{90} values of the FMO slag at different stages are listed in Table 23, and the PSD is shown in Figure 38. The d_{50} of the FMO slag decreased from 52 µm to 50.5 µm during the leaching phase and to 49.9 µm during the CCD phase. This suggests that the leaching and CCD stages effectively dissolved specific materials, resulting in smaller overall particle sizes. The d_{10} increased from 8.5 µm to 13.2 µm during the leaching phase, then slightly decreased to 12.1 µm during the CCD phase. This rise in d_{10} likely results from the complete dissolution of smaller particles, which increases the overall d_{10}. Conversely, the d_{90} grew from 123 µm to 124 µm during leaching and 125 µm during the CCD stage. This growth in d_{90} may be attributed to larger particles resisting dissolution or having less time to react chemically with lixiviants due to quicker settling.

From the PSD in Figure 38, it is clear that the leached slag, FMO[0], exhibits a smaller main peak, a secondary peak at a smaller particle size, and fewer fine particles below 10 µm, indicating a reduction in overall size and the complete dissolution of most finer particles. After completion of both leaching and CCD phases, the slag sample shows a slightly smaller main peak than the slag only subjected to leaching, along with a marginally smaller secondary peak and a slight increase in fine particles below 10 µm.

5.2.3 Leaching at 10 wt% solids

The intermediate and final lixiviant samples were also sent for ICP-OES analysis to determine recovery of major elements during the leaching and CCD stages. The ICP-OES analysis measured elemental concentrations in each lixiviant sample and enabled calculation of the total recovery for each component. The percentages and masses of dissolution achieved in the leaching and CCD stages are summarised in Table 24.

Table 24: Dissolution of element in the leaching and CCD stage for the first run at 10 wt%

	Mn		Si		Al	
Stage	**Mass dissolved (mg)**	**Dissolution (%)**	**Mass dissolved (mg)**	**Dissolution (%)**	**Mass dissolved (mg)**	**Dissolution (%)**
Leach	10784,8	33,47%	1385,2	3,38%	121,0	0,66%
CCD1	261,3	0,81%	-483,1	-1,18%	-269,9	-1,46%
CCD2	322,4	1,00%	-430,6	-1,05%	-245,6	-1,33%
CCD3	582,9	1,81%	1428,2	3,48%	853,7	4,63%
CCD total	1166,6	3,62%	514,6	1,25%	338,3	1,84%
Total	11951,4	37,09%	1899,8	4,63%	459,3	2,49%
	Ca		**Fe**		**Li**	
Stage	**Mass dissolved (mg)**	**Dissolution (%)**	**Mass dissolved (mg)**	**Dissolution (%)**	**Mass dissolved (mg)**	**Dissolution (%)**
Leach	1148,3	7,47%	65,5	1,86%	178,7	29,34%
CCD1	-18,2	-0,12%	16,4	0,47%	-0,7	-0,12%
CCD2	12,8	0,08%	28,6	0,81%	1,8	0,29%
CCD3	841,4	5,48%	81,6	2,31%	6,7	1,11%
CCD total	836,0	5,44%	126,6	3,59%	7,8	1,28%
Total	1984,3	12,92%	192,1	5,45%	186,5	30,62%
	Mg		**K**		**Na**	
Stage	**Mass dissolved (mg)**	**Dissolution (%)**	**Mass dissolved (mg)**	**Dissolution (%)**	**Mass dissolved (mg)**	**Dissolution (%)**
Leach	583,3	14,53%	304,0	18,67%	227,6	13,30%
CCD1	3,4	0,08%	36,0	2,21%	2,9	0,17%
CCD2	9,7	0,24%	28,9	1,77%	3,0	0,18%
CCD3	30,9	0,77%	-28,1	-1,73%	12,7	0,74%
CCD total	43,9	1,09%	36,8	2,26%	18,6	1,09%
Total	627,2	15,63%	340,8	20,92%	246,2	14,39%

**Dissolution (%) = Amount of element dissolved / Amount of element present in sample*

Table 24 displays the mass of each element dissolved during leaching, as determined by ICP-OES analysis. The percentage dissolution is calculated by normalising against the ICP-OES and microwave characterisation analysis. The leaching process preferentially dissolves certain

elements over others. Manganese showed the highest degree of dissolution of 33.47% (10,784.8 mg), closely followed by lithium at 29.34% (178.7 mg). These two elements, therefore, exhibited some selectivity in the leaching process. Potassium, magnesium, sodium and calcium also showed some degree of preferential dissolution, with dissolution of 18.67% (304,0 mg), 14.53% (583.3 mg), 13.30% (227.6 mg) and 7.47% (1,148.3 mg), respectively. However, the recovery of some elements was considerably lower. Silicon, iron, and aluminium showed recoveries of 3.38% (1,385.2 mg), 1,86% (65.5 mg), and 0.66% (121.0 mg), respectively. This result indicates that the leaching conditions were not aggressive enough to dissolve significant amounts of the silicon, iron, and aluminium phases within the FMO slag. The selectivity of manganese and lithium is a key finding, as it can be exploited to benefit downstream processes by reducing the number of impurities and leaving gangue components in the solid residue.

Table 24 also indicates that the overall dissolution of manganese in the CCD system is 3.62% (1,166.6 mg), with 0.81% (261.3 mg) in the first stage, 1.00% (322.4 mg) in the second stage, and 1.88% (582.9 mg) in the third stage. CCD3 displayed the highest manganese recovery, which is typical in a countercurrent flow system where the fresh lixiviant (Lix[0]) encounters the most washed slag (FMO[2]). Similarly, CCD2 showed the second-highest manganese recovery, while CCD1 had the lowest. Iron, magnesium, and sodium exhibited a pattern of dissolution similar to that of manganese during the CCD phase. The behaviour of aluminium, silicon, and calcium was more complex, involving both dissolution and precipitation. In CCD3, where fresh lixiviant enters the system, large quantities of these elements are leached from the solid residue, with 1428.2 mg of silicon, 853.7 mg of aluminium, and 841.4 mg of calcium. The leaching of these undesirable elements consumed a significant portion of the available sulphuric acid, resulting in a substantial decrease in pH from 1.04 to 3.50 as the lixiviant moved to CCD2. The solution chemistry shows a shift in stability, leading to the precipitation of these elements. This shift in stability is caused by a small pH change and a decrease in ionic strength. As the negative recovery values indicate, silicon and aluminium precipitated in CCD2 and CCD1. Calcium showed limited leaching in CCD2 before precipitating in CCD1. Lithium also demonstrated more complex behaviour, with dissolution of 1.11% (6.7 mg) in CCD3, 0.29% (1.8 mg) in CCD2, and precipitation of 0.12% (-0.7 mg) in CCD1.

The overall recovery of manganese in the CCD phase was insignificant, but this outcome was expected due to several factors contributing to the low recovery. The first factor concerns the initial leaching stage, where only 33.47% of the manganese is recovered at a solid-liquid ratio of 10 wt% and a sulfuric acid concentration of 1%. This result aligns with the leaching outcomes presented in section 4.3.1. of this report. The low recovery results in a large amount of manganese entering the CCD system. Another factor is the reduced amount of washing liquid used at a solid-

liquid ratio of 10 wt% solids; operating at a higher solid-liquid ratio inherently involves adding less washing liquid while maintaining a wash ratio of 1. Another factor is diffusion limitations; Table 24 shows that the initial leaching phase recovered 33.47% of the manganese present, whereas the CCD phase recovered only 3.62%. Other elements, including silicone, aluminium, and calcium, leached in much higher quantities during the CCD phase. This indicates that most of the surface manganese had already been leached during the initial phase, leaving manganese mainly in the centre of the particles. The final factor pertains to stoichiometric limitations; the H_2SO_4:Mn ratio within the CCD system is calculated to be 0.159:1. This ratio indicates that, even with complete reaction of sulphuric acid in the washing liquid, a maximum of 15.9% of the manganese could be recovered. However, the recovery is further limited as sulphuric acid reacts with other metals.

5.3 CCD run with a solid-liquid ratio of 5 wt%

5.3.1 Settling

The height-time profile of the three CCD stages, tested by mixing and settling intermediate lixiviants and FMO slag samples, is shown in Figure 39. The corresponding flux-concentration plots for the first, second, and third CCD stages are shown in Figure 40, Figure 41, and Figure 42, respectively. Each flux-concentration plot is constructed using data gathered from the height-time profiles and fitted with a model.

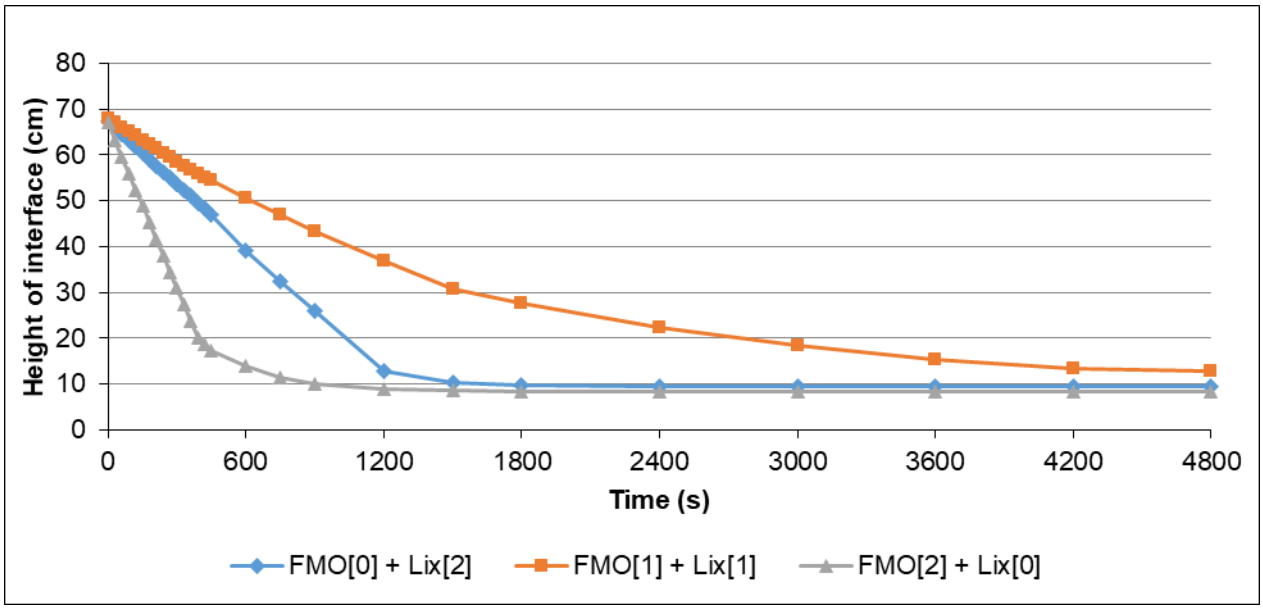

Figure 39: Height-time profile for the three stages of a CCD system for the run at 5 wt%

The height-time profiles of the three CCD stages are shown in Figure 39. In the first CCD stage, using the intermediate products FMO[0] and Lix[2], the initial settling rate of 1.64 m/h is slower than the flocculated settling rate of 8.52 m/h performed in section 4.5.3. However, it remains

significantly faster than the unflocculated settling rate of 0.28 m/h carried out in section 4.5.2. This suggests that the conditions in the first CCD stage hinder settling, yet the flocculant remains effective. Similarly, in the second CCD stage, using the intermediate products FMO[1] and Lix[1], the initial settling rate of 1.14 m/h is slower than the flocculated rate and faster than the unflocculated settling rate. In the third CCD stage, using the intermediate products FMO[2] and Lix[0], the initial settling rate of 4.332 m/h is slower than the flocculated performance. Still, it remains considerably faster than the unflocculated performance. This implies that the conditions within the third CCD stage hinder settling, but the flocculant remains effective. Overall, the settling performance of both the first and second CCD stages is quite similar, whereas settling is much less impeded in the third CCD stage.

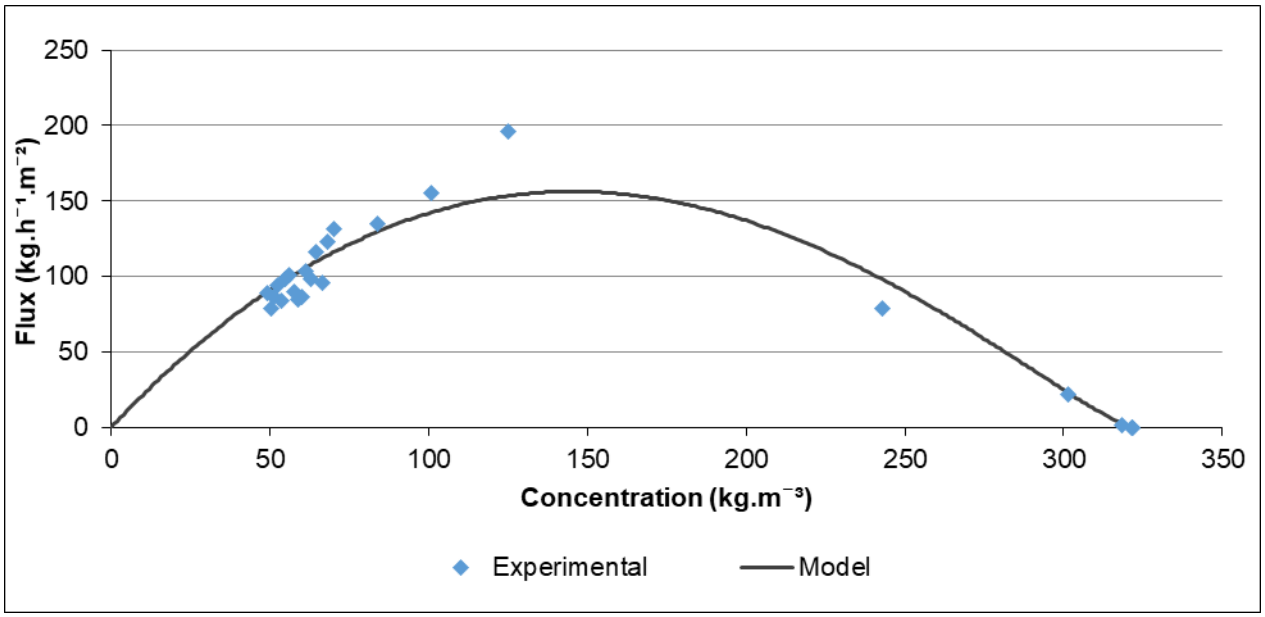

Figure 40: Flux-concentration plot for the first settling stage of a CCD system using intermediate products FMO[0] and Lix[2], for the run at 5 wt%: Model and experimental data

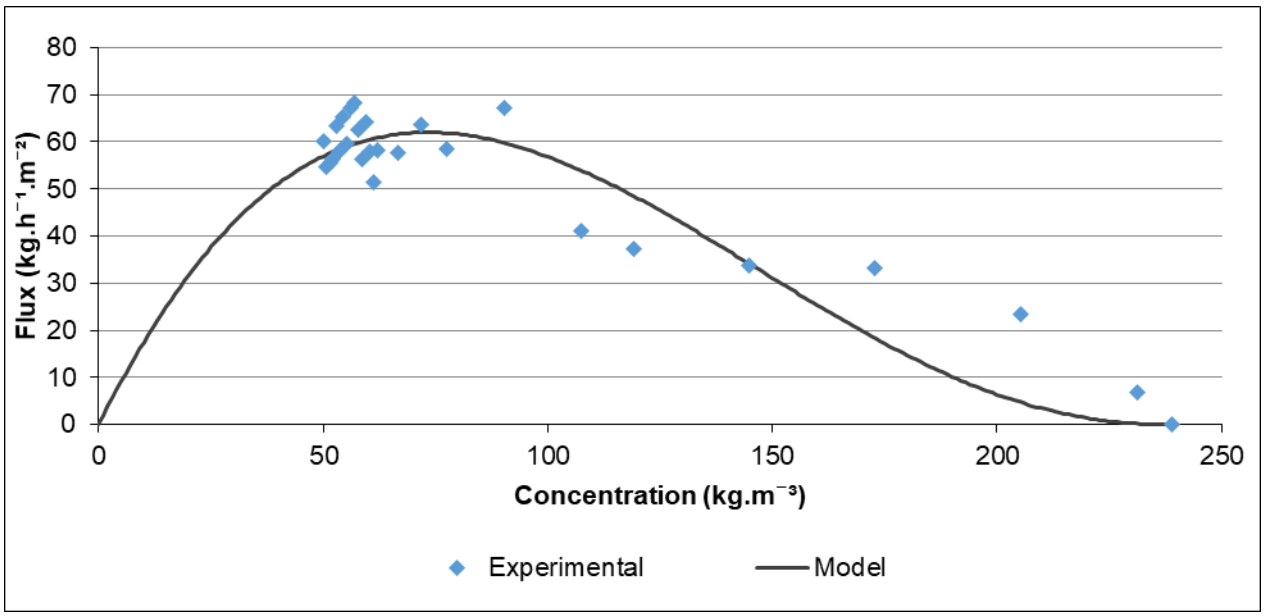

Figure 41: Flux-concentration plot for the second settling stage of a CCD system using intermediate products FMO[1] and Lix[1], for the run at 5 wt%: Model and experimental data

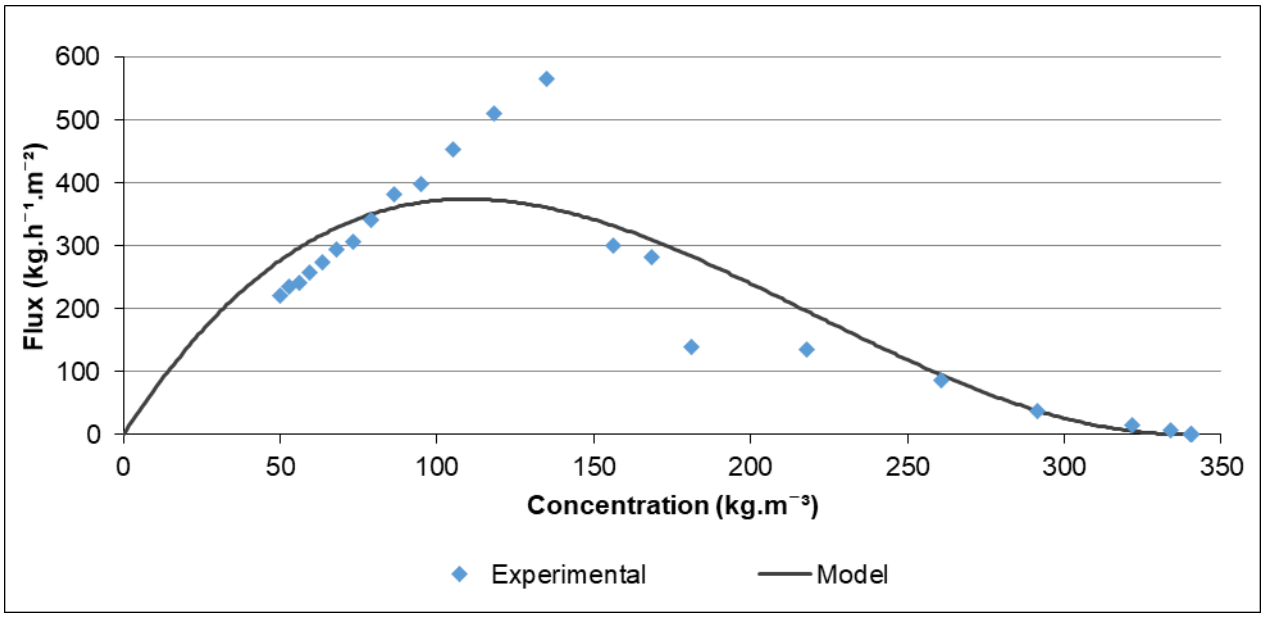

Figure 42: Flux-concentration plot for the third settling stage of a CCD system using intermediate products FMO[2] and Lix[0], for the run at 5 wt%: Model and experimental data

As shown in Figure 40, Figure 41, and Figure 42, using a model as a reference, the first, second, and third CCD stages have maximum fluxes of 155.8 kg/h/m^2, 62.0 kg/h/m^2, and 374.5 kg/h/m^2, respectively. The figures also indicate that the first, second and third CCD stages reach final maximum bed concentrations of 321.4 kg/m^3, 239.0 kg/m^3 and 340.6 kg/m^3, respectively. The K and m values for the three CCD stages are shown in Table 25.

Table 25: Model constants for the three CCD stages at 10 wt%

CCD stage	1	2	3
K	716,82	462,99	2634,77
m	1,21	2,26	2,10

From the K and m parameters shown in Table 25, it is observed that CCD 3 has the highest K value, followed by CCD 1, while CCD 2 has the lowest K value. This indicates that CCD 3 generates the highest overall settling flux, with CCD 1 moderate and CCD 2 the lowest. CCD 2 and 3 also have higher m values than CCD 1, which indicates that their flux decreases more sharply as the concentration approaches the maximum solids concentration. The effects of K and m are evident in the flux-concentration curves. The physical phenomenon observed in stage two can be attributed to a lower ionic strength.

Some conclusions can be drawn by comparing the 5 wt% solid-liquid ratio run with the 10 wt% solid-liquid ratio run in section 5.1.1 of this report. The initial settling rate in each CCD stage follows the same pattern. In both solid-liquid ratios, the third CCD stage had the fastest settling rate, followed by the first CCD stage, and finally, the second CCD stage had the slowest settling rate. The maximum flux in each of the CCD stages follows the same pattern. In both solid-liquid ratios, the third CCD stage had the highest settling flux, followed by the first CCD stage, and finally, the second CCD stage had the lowest settling flux. As expected, the 10 wt% solid-liquid ratio had the highest settling flux for all three stages despite having slower initial settling rates.

5.3.2 Lixiviant and slurry analysis

A lixiviant sample was collected before and after each of the three settling stages. Each sample represents a different stage of the CCD system. All samples were analysed for turbidity, viscosity, density, and pH. The physicochemical properties of the lixiviants are summarised in Table 26. Slag samples were also collected at three stages: one before the leaching stage, another after the leaching stage, and the final after the CCD stage. Each slag sample was analysed for PSD and density. The PSD and density results summary is presented in Table 27, and the PSD is shown in Figure 43.

Table 26: Physicochemical properties of lixiviant from settling test in the run at 5 wt%

Lixiviant	Turbidity (FTU)	Viscosity (mPa.s)	Density (g/cm^3)	pH
Lix[3]	149	1.1058	1.0113	3.76
Lix[2]	208	0.9786	1.0080	3.62
Lix[1]	852	1.1067	1.0061	3.56
Lix[0]	-	0.9016	1.0016	1.20

The four lixiviant properties, turbidity, viscosity, density, and pH, are shown in Table 26. The turbidity decreased from Lix[1] to Lix[3], indicating progressive clarification of the lixiviant as it moves through the CCD system. Since Lix[3] acts as the PLS produced by the CCD system, lower turbidity is a positive sign for downstream processing. Reduced turbidity will lessen the load on subsequent purification steps. The viscosity measurements did not reveal any consistent pattern of change between the lixiviant samples. The most significant change in viscosity occurs between Lix[0] and Lix[1], with a 22.75% increase. Thus, there is a bigger viscosity change within the CCD system for the 5 wt% slurry than for the 10 wt% slurry. The density of the lixiviants increased from Lix[0] to Lix[3], which is expected as more metal species dissolve from the slag into the lixiviant at each CCD stage. Consequently, the rise in dissolved metals contributes to increased lixiviant density. The pH of the lixiviant also increases from Lix[0] to Lix[3]. This rise in pH indicates the consumption of sulphuric acid as metal species are dissolved into the lixiviant. The most substantial pH increase occurs from Lix[0] to Lix[1], suggesting that most acid consumption occurs within the third CCD stage.

Table 27: PSD and density of FMO slag at different stages of the settling and leaching process in the run at 5 wt%

Solid sample	PSD			Density
	d_{10} (µm)	d_{50} (µm)	d_{90} (µm)	(g/cm^3)
Slag	8.5	52	123	3.2895
FMO[0]	9.09	40.5	123	2.8134
FMO[3]	6.77	29.5	115	2.7563

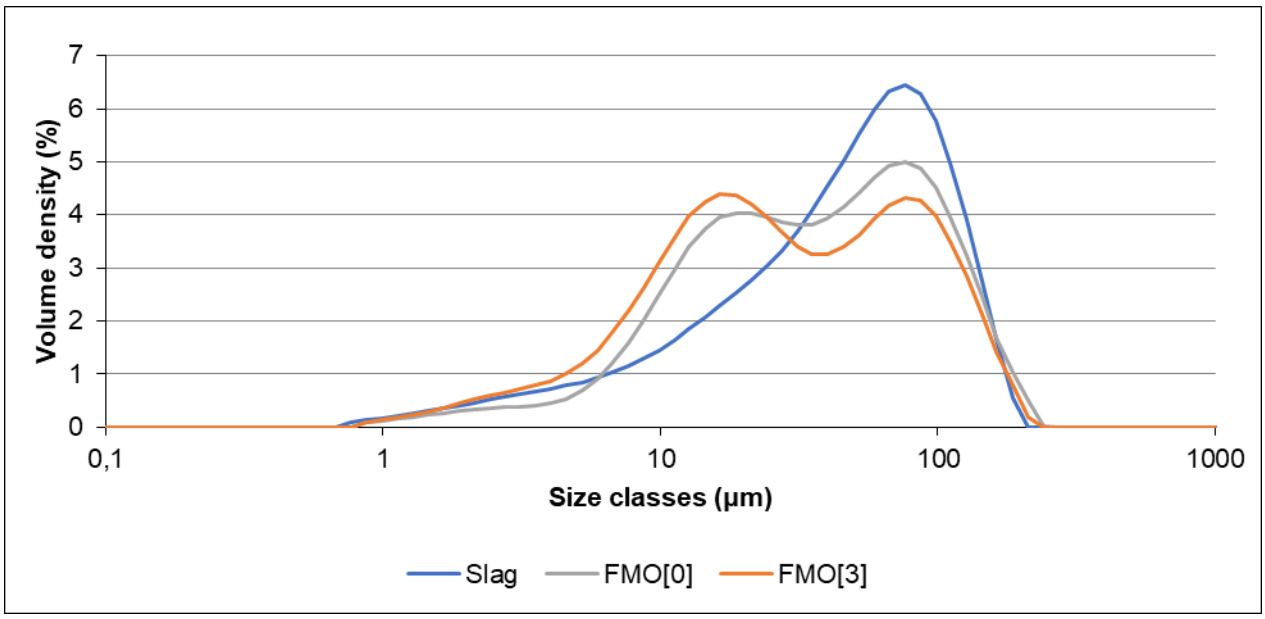

Figure 43: PSD of FMO slag at different stages of the settling and leaching process in the run at 5 wt%

The density of the FMO slag at different stages is shown in Table 27. The density decreased from 3.2895 g/cm³ to 2.8134 g/cm³ during the leaching phase and dropped to 2.7563 g/cm³ during the CCD phase. This decline indicates the dissolution of denser components within the FMO slag, leaving behind the less dense materials.

The PSD, d_{10}, d_{50}, and d_{90} values of the FMO slag at different stages are listed in Table 27, and the PSD is shown in Figure 43. The d_{50} of the FMO slag decreased from 52 µm to 40.5 µm during the leaching phase and to 29.5 µm during the CCD phase. This suggests that the leaching and CCD stages effectively dissolved specific materials, resulting in smaller overall particle sizes. The d_{10} slightly increased from 8.5 µm to 9.09 µm during the leaching phase, then decreased to 6.77 µm during the CCD phase. This rise in d_{10} during the leaching phase likely results from the complete dissolution of most smaller particles, thereby increasing the overall d_{10}. The d_{90} remained constant at 123 µm during the leaching stage, suggesting that larger particles were either less soluble or had less time to react chemically with lixiviants due to faster settling. The d_{90} decreased to 115 µm during the CCD stage.

From the PSD in Figure 43, it is clear that the leached slag, FMO[0], exhibits a smaller main peak, a secondary peak at a smaller particle size, and fewer fine particles below 10 µm, indicating a reduction in overall size and the complete dissolution of most finer particles. After completion of both leaching and CCD phases, the slag sample shows a smaller main peak than the slag only subjected to leaching, along with a larger secondary peak and a slight increase in fine particles below 10 µm.

5.3.3 Leaching at 5 wt% solids

Similarly, to the 10 wt% solid-liquid experiment, intermediate and final lixiviant samples were sent for ICP-OES analysis to determine recovery of major elements during the leaching and CCD stages. The ICP-OES analysis measured elemental concentrations in each lixiviant sample and enabled calculation of the total recovery for each component. The percentages and masses of dissolution achieved in the leaching and CCD stages are summarised in Table 28.

Table 28: Dissolution of element in the leaching and CCD stage for the run at 5 wt%

	Mn		Si		Al	
Stage	Mass dissolved (mg)	Dissolution (%)	Mass dissolved (mg)	Dissolution (%)	Mass dissolved (mg)	Dissolution (%)
Leach	12604,5	78,24%	1933,0	9,42%	221,3	2,40%
CCD1	70,4	0,44%	-1026,9	-5,01%	-207,6	-2,25%
CCD2	12,1	0,08%	411,9	2,01%	-59,5	-0,65%
CCD3	135,4	0,84%	1808,1	8,81%	1483,0	16,09%
CCD total	217,9	1,35%	1193,1	5,82%	1216,0	13,20%
Total	12822,4	79,59%	3126,1	15,24%	1437,3	15,60%
	Ca		**Fe**		**Li**	
Stage	Mass dissolved (mg)	Dissolution (%)	Mass dissolved (mg)	Dissolution (%)	Mass dissolved (mg)	Dissolution (%)
Leach	1295,0	16,86%	432,9	24,55%	192,7	63,28%
CCD1	-52,8	-0,69%	4,6	0,26%	1,4	0,46%
CCD2	12,8	0,17%	2,0	0,12%	0,1	0,04%
CCD3	1003,3	13,06%	21,6	1,22%	1,8	0,58%
CCD total	963,2	12,54%	28,2	1,60%	3,3	1,08%
Total	2258,2	29,40%	461,0	26,15%	196,0	64,37%
	Mg		**K**		**Na**	
Stage	Mass dissolved (mg)	Dissolution (%)	Mass dissolved (mg)	Dissolution (%)	Mass dissolved (mg)	Dissolution (%)
Leach	667,3	33,25%	478,9	58,81%	246,1	28,77%
CCD1	6,3	0,31%	37,0	4,54%	15,0	1,75%
CCD2	4,4	0,22%	14,0	1,72%	1,0	0,12%
CCD3	3,1	0,15%	14,5	1,79%	0,5	0,06%
CCD total	13,7	0,68%	65,5	8,05%	16,5	1,93%
Total	681,0	33,93%	544,5	66,86%	262,7	30,70%

**Dissolution (%) = Amount of element dissolved / Amount of element present in sample*

Table 28 shows the mass of each element dissolved during leaching, as determined by ICP-OES analysis. The dissolution percentage is calculated by normalising against the ICP-OES and microwave characterisation analysis. The leaching process preferentially dissolves certain

elements over others. Manganese exhibited the highest dissolution at 78.24% (12,604.5 mg), closely followed by lithium and potassium at 63.28% (192.7 mg) and 58.81% (478.9 mg), respectively. These three elements, therefore, demonstrated some selectivity during leaching. Magnesium, sodium, iron, calcium, and silicon also showed some degree of preferential dissolution, with dissolution degrees of 33.25% (667.3 mg), 28.77% (246.1 mg), 24.55% (432.9 mg), 16.86% (1,295.0 mg), and 9.42% (1,922.0 mg), respectively. However, aluminium recovery was considerably lower, at 2.4% (221.3 mg). This indicates that the leaching conditions were not sufficiently aggressive to dissolve significant amounts of aluminium phases within the FMO slag. The selectivity of manganese and lithium is a key finding, as it could be exploited to benefit downstream processes by reducing impurities and leaving gangue components in the solid residue.

Table 28 also indicates that the overall dissolution of manganese in the CCD system is 1.35% (217.9 mg), with 0.44% (70.4 mg) in the first stage, 0.08% (12.1 mg) in the second stage, and 0.84% (135.4 mg) in the third stage. CCD3 displayed the highest manganese recovery, which is typical in a countercurrent flow system where the fresh lixiviant (Lix[0]) encounters the most washed slag (FMO[2]). Iron and lithium exhibited a pattern of dissolution similar to that of manganese during the CCD phase. The behaviour of aluminium, silicon, and calcium was more complex, involving both dissolution and precipitation. In CCD3, where fresh lixiviant enters the system, large quantities of these elements are leached from the solid residue, with 1808.1 mg of silicon, 1483.0 mg of aluminium, and 1003.3 mg of calcium. The leaching of these undesirable elements consumed a significant portion of the available sulphuric acid, causing the acidity to decrease substantially from a pH of 1.20 to 3.56 as the lixiviant moved to CCD2. The solution chemistry shows a shift in stability, leading to the precipitation of these elements. As the negative recovery values indicate, aluminium precipitated in CCD2 and CCD1. Silicone and calcium showed limited leaching in CCD2 before precipitating in CCD1.

The overall recovery of manganese and lithium in the CCD system was insignificant, but this outcome was expected due to several factors contributing to the low recovery. The first factor involves diffusion limitations; Table 28 shows that the initial leaching phase recovered 78.24% of the manganese present, whereas the CCD phase only recovered 1.35%. And other elements, including silicone, aluminium, and calcium, leached out in much higher quantities during the CCD phase, indicating that most of the surface manganese was already leached during the initial leaching phase, leaving manganese mainly in the centre of the particles.

5.4 Summary of 5 wt% and 10 wt% CCD leaching and settling experiments

- At a solid-liquid ratio of 5 wt%, the actual washing efficiency exceeds that at a 10 wt% ratio, with 97.98% compared to 84.22%.
- It is clear that manganese and lithium can be leached selectively regardless of the solid-liquid ratio, but diffusion limitations hinder the complete dissolution.
- Operating at a lower solid-liquid ratio of 5 wt% improves the leaching of these target metals.
- Overall, operating at a lower solid-liquid ratio of 5 wt% did not improve the target metal recovery within the CCD system. An additional 1.35 wt% of the target metal is dissolved at a solid-liquid ratio of 5 wt% compared to 3.62% at 10 wt%.

Chapter 6: Conceptual design of CCD system

This section outlines the conceptual design of a demonstration model CCD system with a throughput of 100 kg/h of FMO slag. The design utilises experimental data from the CCD settling tests conducted in Section 5 of this report, employing a batch settling approach to design and size a continuous process. The 5 wt% solid-liquid experiment is a reference for designing the conceptual CCD system. This section is divided into five parts: assumptions based on experimental findings, plug flow diagram, conceptual mass balance, conceptual thickener sizing and design conclusion.

6.1 Assumptions based on experimental findings

The conceptual design is based on the following assumptions and experimental findings:

- Leaching stage efficiency: The initial leaching phase achieves a manganese recovery of 64.2%, with the remaining manganese entering the CCD system in solid form. This value takes into account both the manganese entering the CCD system through the remaining slag and the PLS not removed.
- Solid-liquid separation: The parameters for thickener sizing are based on the observed settling rate at each CCD stage during batch settling tests.
- Lixiviant properties: The lixiviant characteristics, including pH, turbidity, viscosity, and density within the CCD system, are assumed to be the same as observed during the batch settling tests.
- Slurry properties: The slurry characteristics, such as density and PSD in the CCD system, are assumed to be identical to those observed in the batch settling tests.
- Number of CCD stages: A three-stage CCD circuit is selected, consistent with the batch settling tests performed.
- Fixed flow rates: The flow rates in the overflow and underflow of the thickener are assumed to be consistent across all stages.
- Steady state: The system is assumed to function at steady state.
- Perfect mixing: The CCD system is presumed to be perfectly mixed, resulting in identical concentrations of water, acid, and dissolved metal in the vessel, as well as in the overflow and underflow lixiviants.
- Process conditions: The CCD system is assumed to operate at a steady temperature of 25 °C and atmospheric pressure.
- Material balances: No material loss is assumed within the CCD system.
- Solid flow: It is assumed that no solids are present in any of the overflow streams

6.2 Process flow diagram (PFD)

The PFD functions as a visual illustration of the proposed CCD system, demonstrating the main unit operations and material streams. A PFD for the proposed CCD system is illustrated in Figure 44.

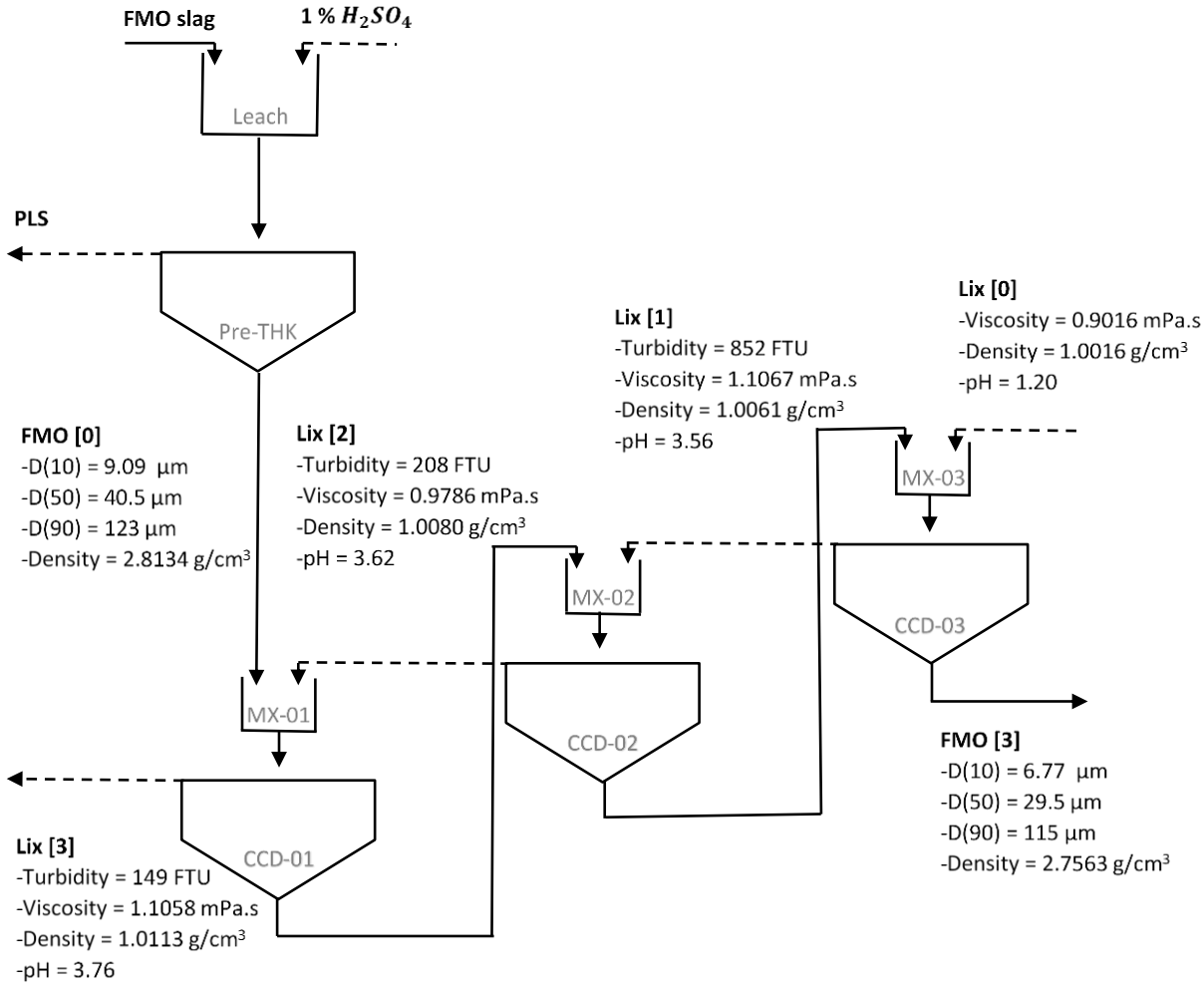

Figure 44: Process flow diagram of the proposed CCD system at a 5 wt% solid-liquid ratio

The main unit operations include one leaching tank, one pre-thickener, three CCD thickeners, and three mixing tanks.

1. Leaching and pre-thickening
    - Leaching tank: FMO slag and a 1% H_2SO_4 solution are combined in the leaching tank to create a mixture with a 5 wt% solid-liquid ratio.

- Pre-thickener: After leaching, the slurry is pumped to the pre-thickener, where the FMO slag settles, forming a thickened bed of solid-liquid ratio 30 wt% and a clear PLS. The thickened slurry is pumped to MX-01, and the PLS is sent for further downstream processing.

2. CCD washing
   - MX-01: In the first mixer, the thickened slurry (FMO[0]) is combined with lixiviant (Lix[2]) and then pumped to CCD-01.
   - CCD-01: In CCD-01, the slurry mixture settles, forming a thickened bed with a solid-liquid ratio of 30 wt% (FMO[1]), and the final washing step lixiviant (Lix[3]). The thickened slurry is pumped to MX-02, and Lix[3] is sent for further downstream processing.
   - MX-02: In the second mixer, the thickened slurry (FMO[1]) is combined with lixiviant (Lix[1]) and then pumped to CCD-02.
   - CCD-02: In CCD-02, the slurry mixture settles, forming a thickened bed with a solid-liquid ratio of 30 wt% (FMO[2]), and washing step lixiviant (Lix[2]). The thickened slurry is pumped to MX-03, and Lix[2] is pumped to MX-01.
   - MX-03: In the third mixer, the thickened slurry (FMO[2]) is combined with lixiviant (Lix[0]) and then pumped to CCD-03.
   - CCD-03: In CCD-03, the slurry mixture settles, forming a thickened bed with a solid-liquid ratio of 30 wt% (FMO[3]), and washing step lixiviant (Lix[1]). The thickened slurry is removed as a waste product, and Lix[1] is pumped to MX-02.

6.3 Conceptual mass balance

The conceptual mass balance monitors the flow of materials throughout the entire process. This section is divided into three main parts: unit processes, CCD system, and overall mass balance. The overall mass balance covers the leaching, pre-thickening, and CCD stages, while the CCD mass balance focuses only on the CCD system. All metals of interest are tracked within the mass balance, but only the two target metals, manganese and lithium, and the three major impurities, silicone, aluminium and calcium, are discussed.

6.3.1 Conceptual mass balance over the unit processes

Figure 45 shows the boundaries for each unit process where a mass balance is conducted.

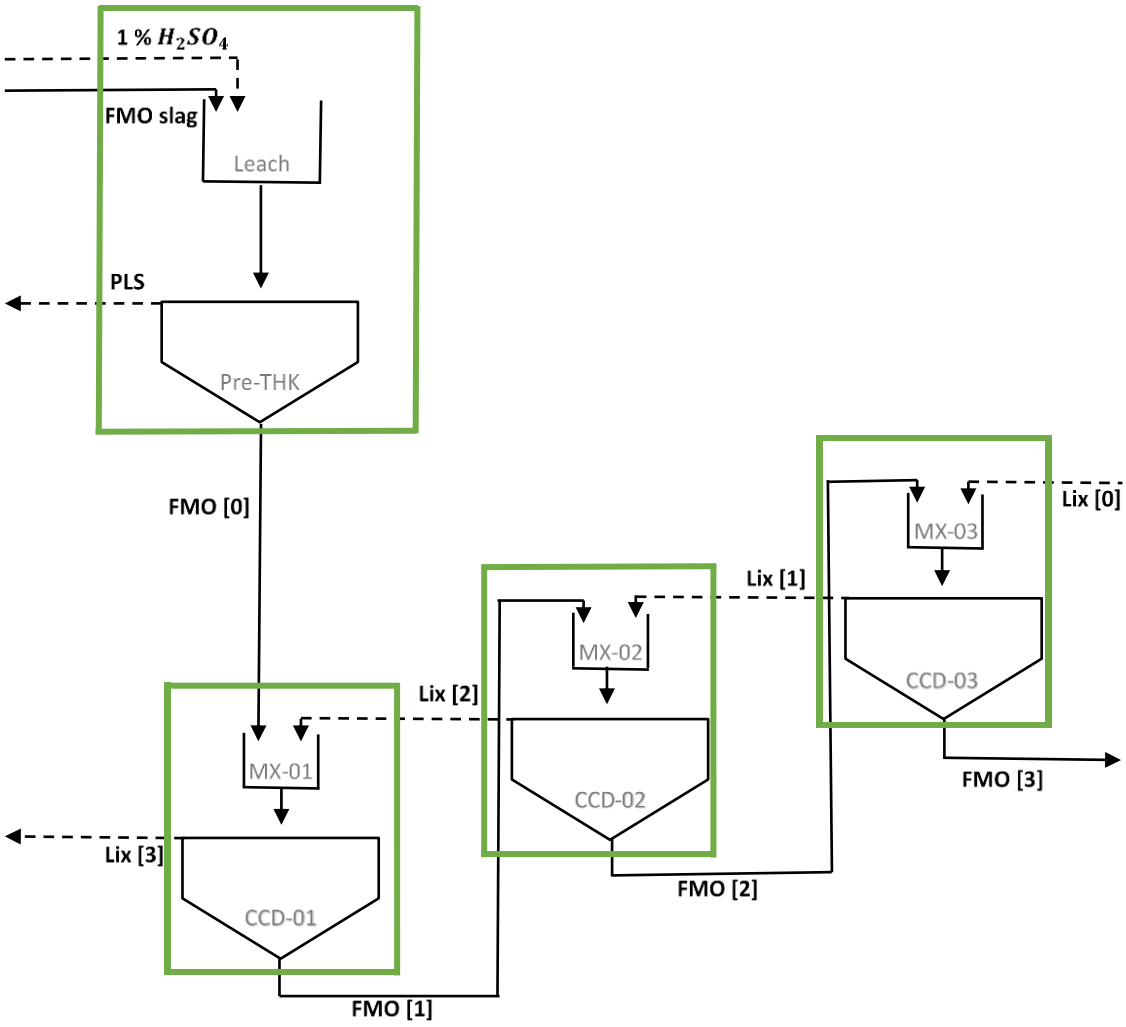

Figure 45: PFD indicating the unit process mass balance boundaries

The mass balance quantifies the movement of each element and whether it is in the solid or liquid phase. The mass balance is closed as the sum of the input streams of each component equals the output streams. The change in mass of the liquid and solid phases is due to the dissolution and precipitation of metals. The overall mass flow, including both the liquid and solid phases, remains constant.

The CCD system functions as a washing process that removes dissolved target metals from the slurry mixture into a lixiviant. The CCD washing liquid consists of a dilute sulphuric acid solution intended to dissolve and recover more target metals within the CCD system.

6.3.1.1 Mass balance over the leaching stage

The mass balance over the leaching stage consists of two input and two output streams.

Input streams:

- FMO slag – FMO slag crushed to -125 µm is added to the leaching stage
- 1% H_2SO_4 - Fresh lixiviant solution with a 1% sulphuric acid concentration is added to the leaching stage

Output streams:

- FMO[0] – Thickened slurry mixture consisting of leached FMO slag and PLS removed by the underflow of the pre-thickener
- PLS – Leach solution removed as overflow from the pre-thickener

Table 29: Conceptual mass balance over the leaching stage

Streams		Input streams		Output streams	
		1% H_2SO_4	FMO slag	PLS	FMO[0]
Mass flow rate (kg/h)		1986,05	100	1691,09	394,95
Solid flow (kg/h)		0	100	0	81,93
Liquid flow (kg/h)		1986,05	0	1691,09	313,02
Sulphuric acid (kg/h)		36,05	0	30,42	5,63
Water (kg/h)		1950,00	0	1645,43	304,57
Total dissolved solids (kg/h)		0	0	15,25	2,82
Element mass in liquid (kg/h)	Mn	0	0	10,636	1,969
	Si	0	0	1,631	0,302
	Al	0	0	0,187	0,035
	Ca	0	0	1,093	0,202
	Fe	0	0	0,365	0,068
	Li	0	0	0,163	0,030
	Mg	0	0	0,563	0,104
	K	0	0	0,404	0,075
	Na	0	0	0,208	0,038
Element mass in solid (kg/h)	Mn	0	16,110	0	3,505
	Si	0	20,513	0	18,580
	Al	0	9,215	0	8,994
	Ca	0	7,682	0	6,387
	Fe	0	1,763	0	1,330
	Li	0	0,305	0	0,112
	Mg	0	2,007	0	1,340
	K	0	0,814	0	0,335
	Na	0	0,856	0	0,609

Table 29 presents a detailed conceptual mass balance over the leaching stage for a system with an initial FMO slag feed rate of 100 kg/h. The mass balance is closed as the sum of the input

streams (1% H_2SO_4 and FMO slag) for each element equals the output streams (PLS and FMO[0]).

Of the 16.110 kg/h of target metal, manganese entering the leaching stage, 12.605 kg/h (78.24%) is dissolved during the leaching process. Out of this, 10.636 kg/h of dissolved manganese reports to the overflow of the pre-thickener and is sent for further downstream processing. The remaining 1.969 kg/h of dissolved manganese reports to the pre-thickener underflow and is sent to the CCD system for washing. The remaining 3.505 kg/h of manganese remains in the solid phase and also reports to the underflow of the pre-thickener.

Similarly, of the 0.305 kg/h target metal, lithium enters the leaching stage, 0.193 kg/h (63.28%) is dissolved during the leaching process. Out of this, 0.163 kg/h of dissolved manganese reports to the overflow of the pre-thickener. The remaining 0.030 kg/h of dissolved lithium reports to the pre-thickener underflow and is sent to the CCD system for washing. The remaining 0.112 kg/h of lithium remains in the solid phase and also reports to the underflow of the pre-thickener.

The major impurities, silicone, aluminium and calcium, mostly remain in the solid phase with a dissolution rate of 9.42%, 2.40%, and 16.86%.

6.3.1.2 Mass balance over the first CCD

The mass balance over the first CCD stage consists of two input and two output streams.

Input streams:

- FMO[0] – Thickened slurry mixture consisting of leached FMO slag and PLS removed by the underflow of the pre-thickener
- Lix[2] - Lixiviant solution moving counter currently from the overflow of the second CCD

Output streams:

- FMO[1] – Thickened slurry mixture consisting of leached FMO slag and leach solution removed by the underflow of the first CCD
- Lix[3] – Leach solution removed as overflow in the first CCD stage

Table 30: Conceptual mass balance over the first CCD stage

Streams		Input streams		Output streams	
		Lix[2]	FMO[0]	Lix[3]	FMO[1]
Mass flow rate (kg/h)		1675,40	394,96	1676,82	393,54
Solid flow (kg/h)		0	81,93	0	83,08
Liquid flow (kg/h)		1675,40	313,02	1676,82	310,46
Sulphuric acid (kg/h)		8,39	5,63	11,83	2,19
Water (kg/h)		1661,93	304,57	1659,36	307,15
Total dissolved solids (kg/h)		5,08	2,82	5,63	1,13
Element mass in liquid (kg/h)	Mn	0,537	1,969	2,150	0,430
	Si	2,074	0,302	1,125	0,225
	Al	1,324	0,035	0,959	0,192
	Ca	1,008	0,202	0,965	0,193
	Fe	0,037	0,068	0,091	0,018
	Li	0,008	0,030	0,033	0,007
	Mg	0,029	0,104	0,117	0,023
	K	0,052	0,075	0,136	0,027
	Na	0,012	0,038	0,054	0,011
Element mass in solid (kg/h)	Mn	0	3,505	0	3,431
	Si	0	18,580	0	19,606
	Al	0	8,994	0	9,201
	Ca	0	6,387	0	6,440
	Fe	0	1,330	0	1,326
	Li	0	0,112	0	0,110
	Mg	0	1,340	0	1,333
	K	0	0,335	0	0,298
	Na	0	0,609	0	0,595

Table 30 presents a detailed conceptual mass balance over the first CCD stage for a system with an initial FMO slag feed rate of 100 kg/h. The mass balance is closed as the sum of the input streams (Lix[2] and FMO[0]) for each element equals the output streams (Lix[3] and FMO[1]).

CCD 1 has a dissolved manganese feed rate of 1.969 kg/h from the FMO[0] slurry and 0.537 kg/h from the Lix[2] lixiviant, with an additional 0.074 kg/h dissolved. This results in 2.580 kg/h of dissolved manganese entering CCD 1. Of this, 2.150 kg/h reports to the overflow (Lix[3]) and is sent for further downstream processing. The remaining 0.430 kg/h of dissolved manganese reports to the underflow of CCD 1 and is pumped to CCD 2 for additional washing. The remaining 3.431 kg/h of manganese stays in the solid phase and also reports to the underflow of CCD 1.

Similarly, for lithium, CCD 1 has a dissolved lithium feed rate of 0.030 kg/h from the FMO[0] slurry and 0.008 kg/h from the Lix[2] lixiviant, with an additional 0.002 kg/h dissolved. This results in 0.040 kg/h of dissolved manganese entering CCD 1. Of this, 0.033 kg/h reports to the overflow

(Lix[3]) and is sent for further downstream processing. The remaining 0.007 kg/h of dissolved lithium reports to the underflow of CCD 1 and is pumped to CCD 2 for additional washing. The remaining 0.110 kg/h of lithium remains in the solid phase and also reports to the underflow of CCD 1.

The three major impurities, silicone, aluminium, and calcium, precipitate out in the first CCD stage.

6.3.1.3 Mass balance over the second CCD

The mass balance over the first CCD stage consists of two input and two output streams.

Input streams:

- FMO[1] – Thickened slurry mixture consisting of leached FMO slag and leach solution removed by the underflow of the first CCD
- Lix[1] - Lixiviant solution moving counter currently from the overflow of the third CCD

Output streams:

- FMO[2] – Thickened slurry mixture consisting of leached FMO slag and leach solution removed by the underflow of the second CCD
- Lix[2] – Lixiviant solution moving counter currently from the overflow of the second CCD

Table 31: Conceptual mass balance over the second CCD stage

Streams		Input streams		Output streams	
		Lix[1]	FMO[1]	Lix[2]	FMO[2]
Mass flow rate (kg/h)		1674,73	393,55	1675,40	392,88
Solid flow (kg/h)		0	83,08	0	82,68
Liquid flow (kg/h)		1674,73	310,46	1675,40	310,19
Sulphuric acid (kg/h)		7,75	2,19	8,39	1,55
Water (kg/h)		1662,41	307,15	1661,93	307,62
Total dissolved solids (kg/h)		4,57	1,13	5,08	1,02
Element mass in liquid (kg/h)	Mn	0,202	0,430	0,537	0,107
	Si	1,852	0,225	2,074	0,415
	Al	1,457	0,192	1,324	0,265
	Ca	1,004	0,193	1,008	0,202
	Fe	0,024	0,018	0,037	0,007
	Li	0,003	0,007	0,008	0,002
	Mg	0,007	0,023	0,029	0,006
	K	0,021	0,027	0,052	0,010
	Na	0,002	0,011	0,012	0,002
Element mass in solid (kg/h)	Mn	0	3,431	0	3,419
	Si	0	19,606	0	19,195
	Al	0	9,201	0	9,261
	Ca	0	6,440	0	6,427
	Fe	0	1,326	0	1,324
	Li	0	0,110	0	0,110
	Mg	0	1,333	0	1,329
	K	0	0,298	0	0,284
	Na	0	0,595	0	0,593

Table 31 presents a detailed conceptual mass balance over the second CCD stage for a system with an initial FMO slag feed rate of 100 kg/h. The mass balance is closed as the sum of the input streams (Lix[1] and FMO[1]) for each element equals the output streams (Lix[2] and FMO[2]).

CCD 2 has a dissolved manganese feed rate of 0.430 kg/h from the FMO[1] slurry and 0.202 kg/h from the Lix[1] lixiviant, with an additional 0.012 kg/h dissolved. This results in 0.644 kg/h of dissolved manganese entering CCD 2. Of this, 0.537 kg/h reports to the overflow (Lix[2]) and is sent to CCD 1. The remaining 0.107 kg/h of dissolved manganese reports to the underflow of CCD 2 and is pumped to CCD 3 for further washing. The remaining 3.419 kg/h of manganese remains in the solid phase and also reports to the underflow of CCD 2.

Similarly, for lithium, CCD 2 has a dissolved lithium feed rate of 0.007 kg/h from the FMO[1] slurry and 0.003 kg/h from the Lix[1] lixiviant. This results in 0.010 kg/h of dissolved manganese entering CCD 2. Of this, 0.008 kg/h reports to the overflow (Lix[2]) and is sent to CCD 3. The remaining 0.002 kg/h of dissolved lithium reports to the underflow of CCD 2 and is pumped to CCD 3 for further washing. The remaining 0.110 kg/h of lithium stays in the solid phase and also reports to the underflow of CCD 2.

Two of the major impurities in the FMO slag, silicone and calcium, are dissolved into the lixiviant, while the other major impurity, aluminium, precipitates out.

6.3.1.4 Mass balance over the third CCD

The mass balance over the first CCD stage consists of two input and two output streams.

Input streams:

- FMO[2] – Thickened slurry mixture consisting of leached FMO slag and leach solution removed by the underflow of the second CCD
- Lix[0] - Fresh lixiviant solution with a 0.25% sulphuric acid concentration added to the third CCD stage

Output streams:

- FMO[3] – Waist product consisting of leached FMO slag and lixiviant removed from the third CCD stage
- Lix[1] – Lixiviant solution moving counter currently from the overflow of the third CCD

Table 32: Conceptual mass balance over the third CCD stage

Streams		Input streams		Output streams	
		Lix[0]	FMO[2]	Lix[1]	FMO[3]
Mass flow rate (kg/h)		1670,13	392,88	1674,73	388,27
Solid flow (kg/h)		0	82,68	0	78,21
Liquid flow (kg/h)		1670,13	310,19	1674,73	310,06
Sulphuric acid (kg/h)		7,63	1,55	7,75	1,43
Water (kg/h)		1662,50	307,62	1662,41	307,71
Total dissolved solids (kg/h)		0	1,02	4,57	0,91
Element mass in liquid (kg/h)	Mn	0	0,107	0,202	0,040
	Si	0	0,415	1,852	0,370
	Al	0	0,265	1,457	0,291
	Ca	0	0,202	1,004	0,201
	Fe	0	0,007	0,024	0,005
	Li	0	0,002	0,002	0,001
	Mg	0	0,006	0,007	0,001
	K	0	0,010	0,021	0,004
	Na	0	0,002	0,002	0,000
Element mass in solid (kg/h)	Mn	0	3,419	0	3,284
	Si	0	19,195	0	17,386
	Al	0	9,261	0	7,778
	Ca	0	6,427	0	5,424
	Fe	0	1,324	0	1,302
	Li	0	0,110	0	0,109
	Mg	0	1,329	0	1,326
	K	0	0,284	0	0,270
	Na	0	0,593	0	0,593

Table 32 presents a detailed conceptual mass balance over the second CCD stage for a system with an initial FMO slag feed rate of 100 kg/h. The mass balance is closed as the sum of the input streams (Lix[0] and FMO[2]) for each element equals the output streams (Lix[1] and FMO[3]).

CCD 3 has a dissolved manganese feed rate of 0.107 kg/h from the FMO[2] slurry and 0 kg/h from the Lix[0] lixiviant, with an additional 0.135 kg/h dissolved. This results in 0.242 kg/h of dissolved manganese entering CCD 3. Of this, 0.202 kg/h reports to the overflow (Lix[1]) and is sent to CCD 2. The remaining 0.040 kg/h of dissolved manganese reports to the underflow of CCD 3 and is removed as a waste product from the washing step. The remaining 3.284 kg/h of manganese stays in the solid phase and also reports to the underflow of CCD 3.

Similarly, for lithium CCD 3 has a dissolved lithium feed rate of 0.002 kg/h from the FMO[2] slurry and 0 kg/h from the Lix[0] lixiviant, with an additional 0.001 kg/h dissolved. This results in 0.003

kg/h of dissolved manganese entering CCD 3. Of this, 0.002 kg/h reports to the overflow (Lix[1]) and is sent to CCD 2. The remaining 0.001 kg/h of dissolved lithium reports to the underflow of CCD 3 and is removed as a waste product from the washing step. The remaining 0.109 kg/h of lithium stays in the solid phase and also reports to the underflow of CCD 3.

The three major impurities within the FMO slag, silicone, aluminium, and calcium, are dissolved into the lixiviant.

6.3.2 Conceptual mass balance for the overall system and CCD system

Figure 46 shows the boundaries for the CCD system and the overall mass balance.

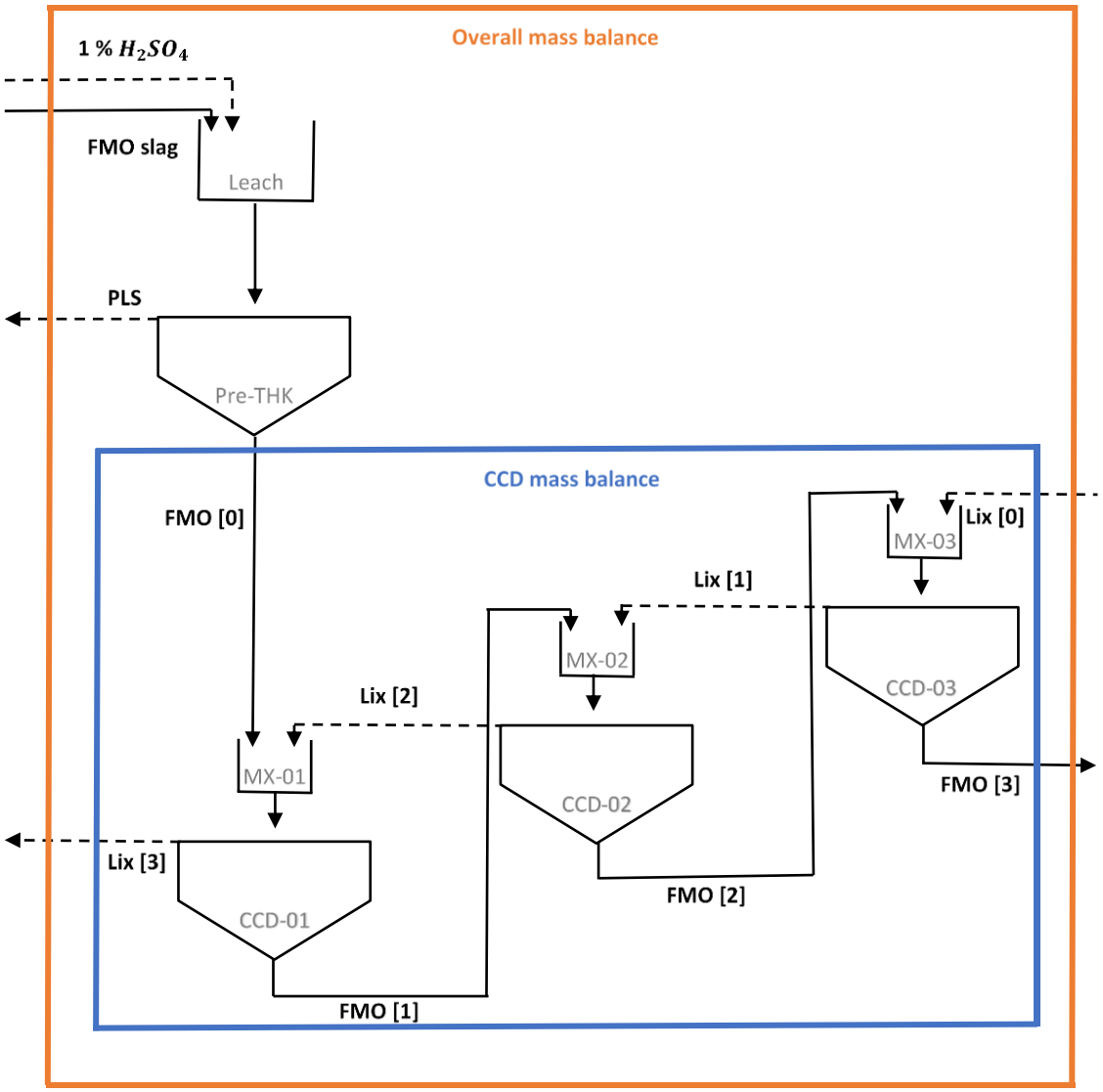

Figure 46: PFD indicating the overall and CCD mass balance boundaries

6.3.2.1 CCD mass balance

The CCD mass balance consists of two input streams and two output streams.

Input streams:

- FMO[0] – Slurry mixture of leached FMO slag and remaining PLS added to the first CCD stage
- Lix[0] - Fresh lixiviant solution with a 0.25% sulphuric acid concentration added to the third CCD stage

Output streams:

- FMO[3] – Waist product consisting of leached FMO slag and lixiviant removed from the third CCD stage
- Lix[3] – Leach solution removed as overflow in the first CCD stage

Table 33: Conceptual mass balance over the CCD system

Streams		Input streams		Output streams	
		Lix[0]	FMO[0]	Lix[3]	FMO[3]
Mass flow rate (kg/h)		1670,13	394,96	1676,82	388,27
Solid flow (kg/h)		0	81,93	0	78,21
Liquid flow (kg/h)		1670,13	313,02	1676,82	310,06
Sulphuric acid (kg/h)		7,63	5,63	11,83	1,43
Water (kg/h)		1662,50	304,57	1659,36	307,71
Total dissolved solids (kg/h)		0	2,82	5,63	0,91
Element mass in liquid (kg/h)	Mn	0	1,969	2,150	0,040
	Si	0	0,302	1,125	0,370
	Al	0	0,035	0,959	0,291
	Ca	0	0,202	0,965	0,201
	Fe	0	0,068	0,091	0,005
	Li	0	0,030	0,032	0,001
	Mg	0	0,104	0,117	0,001
	K	0	0,075	0,136	0,004
	Na	0	0,038	0,054	0,000
Element mass in solid (kg/h)	Mn	0	3,505	0	3,284
	Si	0	18,580	0	17,386
	Al	0	8,994	0	7,778
	Ca	0	6,387	0	5,424
	Fe	0	1,330	0	1,302
	Li	0	0,112	0	0,109
	Mg	0	1,340	0	1,326
	K	0	0,335	0	0,270
	Na	0	0,609	0	0,593

Table 33 presents a detailed conceptual mass balance for the entire CCD system, starting with an initial FMO slag feed rate of 100 kg/h. The mass balance is closed as the sum of the input streams (Lix[0] and FMO[0]) for each element equals the output streams (Lix[3] and FMO[3]).

The CCD system has a dissolved manganese feed rate of 1.969 kg/h from the FMO[0] slurry and 0 kg/h from the Lix[0] lixiviant, with an additional 0.221 kg/h dissolved. This results in 2.190 kg/h of dissolved manganese entering the CCD system. Of this, 2.150 kg/h reports to the overflow (Lix[3]) and is sent for further downstream processing. The remaining 0.040 kg/h of dissolved manganese reports to the underflow of CCD 3 and is removed as a waste product from the washing step. The remaining 3.284 kg/h of manganese stays in the solid phase and also reports to the underflow of CCD 3.

Similarly, for lithium, the CCD system has a dissolved lithium feed rate of 0.030 kg/h from the FMO[0] slurry and 0 kg/h from the Lix[0] lixiviant, with an additional 0.003 kg/h dissolved. This results in 0.033 kg/h of dissolved lithium entering the CCD system. Of this, 0.032 kg/h reports to the overflow (Lix[3]) and is sent for further downstream processing. The remaining 0.001 kg/h of dissolved lithium reports to the underflow of CCD 3 and is removed as a waste product from the washing step. The remaining 0.109 kg/h of manganese stays in the solid phase and also reports to the underflow of CCD 3.

The CCD system therefore achieves washing efficiencies of 97.98% for manganese and 98.16% for lithium, accounting for the additional leaching during the CCD stages.

6.3.2.2 Overall mass balance

The overall mass balance consists of three input streams and three output streams.

Input streams:

- FMO slag – Raw slag added at 100 kg/h to the leaching stage
- 1% H_2SO_4 – Fresh lixiviant solution with a 1% sulphuric acid concentration added to the leaching stage
- Lix[0] – Fresh lixiviant solution with a 0.25% sulphuric acid concentration added to the CCD stage

Output streams:

- PLS – pregnant leach solution removed as overflow in the pre-thickening stage
- Lix[3] – Leach solution removed as overflow in the CCD system
- FMO[3] – Waist product consisting of leached FMO slag and lixiviant

Table 34: Conceptual mass balance over the overall system

Streams		Input streams			Output streams		
		1% H_2SO_4	FMO slag	Lix[0]	PLS	FMO[3]	Lix[3]
Mass flow rate (kg/h)		1986,05	100	1670,13	1691,09	388,27	1676,82
Solid flow (kg/h)		0	100	0	0,00	78,21	0,00
Liquid flow (kg/h)		1986,05	0	1670,13	1691,09	310,06	1676,82
Sulphuric acid (kg/h)		36,05	0	7,631	30,42	1,43	11,83
Water (kg/h)		1950,00	0	1662,50	1645,43	307,71	1659,36
Total dissolved solids (kg/h)		0	0	0	15,25	0,91	5,63
Element mass in liquid (kg/h)	Mn	0	0	0	10,636	0,040	2,150
	Si	0	0	0	1,631	0,370	1,125
	Al	0	0	0	0,187	0,291	0,959
	Ca	0	0	0	1,093	0,201	0,965
	Fe	0	0	0	0,365	0,005	0,091
	Li	0	0	0	0,163	0,001	0,033
	Mg	0	0	0	0,563	0,001	0,117
	K	0	0	0	0,404	0,004	0,136
	Na	0	0	0	0,208	0,000	0,054
Element mass in solid (kg/h)	Mn	0	16,110	0	0	3,284	0
	Si	0	20,513	0	0	17,386	0
	Al	0	9,215	0	0	7,778	0
	Ca	0	7,682	0	0	5,424	0
	Fe	0	1,763	0	0	1,302	0
	Li	0	0,305	0	0	0,109	0
	Mg	0	2,007	0	0	1,326	0
	K	0	0,814	0	0	0,270	0
	Na	0	0,856	0	0	0,593	0

Table 34 presents a detailed conceptual mass balance for the overall system, starting with an initial FMO slag feed rate of 100 kg/h. The mass balance is closed as the sum of the input streams (1% H_2SO_4, FMO slag, and Lix[0]) for each element equals the output streams (PLS, FMO[3], and Lix[3]).

The overall system has a manganese feed rate of 16.110 kg/h from the FMO slag. Of this, 12.826 kg/h is dissolved into the lixiviant and 12.786 kg/h is recovered for further processing. The remaining 3.284 kg/h of manganese remains in the solid phase. It is removed from the system as a waste product, along with a lixiviant containing the remaining 0.040 kg/h of dissolved manganese, as stream FMO[3].

Similarly, the overall system has a feed rate of 0.305 kg/h of lithium from the FMO slag. Out of this, 0.196 kg/h dissolves into the lixiviant, and 0.0195 kg/h is recovered for further processing. The remaining 0.109 kg/h of lithium remains in the solid phase. It is removed from the system as

a waste product, with some lixiviant containing the remaining 0.001 kg/h of dissolved lithium as stream FMO[3].

The overall system achieves manganese recovery of 79.37% and lithium recovery of 64.26% by considering both leaching and wash efficiencies.

6.4 Conceptual thickener sizing

The CCD demonstration model is initially sized using data collected from the batch settling tests in Section 5 of this report and the desired FMO slag feed rate of 100 kg/h. Two methods are employed to size the thickeners. The first is the Talmage-Fitch method, based on the Kynch theory, and the second is the Wilhelm-Naide method, based on the Yoshioka-Hassett method.

The Talmage-Fitch method uses the batch settling curve to identify the critical time for calculating the unit area of a thickener. Two approaches are used to find this critical time: the bi-section method, the original approach established by Talmage-Fitch, and the Oltman method, a newer and less conservative approach. The Oltman method, proposed by Fitch and Stevenson, was introduced because the bi-section method often produces thicker area values that exceed experimental results. The Wilhelm-Naide model determines the unit area by calculating total thickener, settling, and withdrawal fluxes. This approach is generally more robust and better suited for settling with modern flocculants, addressing the over- and under-sizing problems encountered with the Kynch and Talmage-Fitch methods. The resulting thickener diameter, based on a FMO slag feed of 100 kg/h for all three methods, is detailed in Table 35 and the calculations are presented in Appendix C.4.

Table 35: Thickener diameter for each settling stage determined by three different methods

	Diameter (m)			
Method	Pre-thickener	CCD 1	CCD 2	CCD 3
Bi-section	0,62	1,21	1,91	0,87
Oltman	0,47	1,12	1,37	0,66
Wilhelm-Naide	0,69	1,25	1,47	0,74

Based on the thickener diameter results in Table 35, the Wilhelm-Naide method yields more conservative outcomes than the Oltman method, but less conservative than the bi-section method. Since the Wilhelm-Naide method is specifically designed for systems with modern flocculants and is known to overcome the size limitations of Kynch-based methods, it has been selected as the basis for the conceptual design. The largest thickener diameter calculated with this method is 1.47 m for CCD 2. Therefore, a standard diameter of 1.5 m is chosen for all three

thickeners in the CCD circuit to simplify design and construction. This approach ensures uniform sizing across all stages while ensuring the largest required thickener is not undersized.

6.5 Summary of design

- The conceptual design shows that batch laboratory-scale experiments can be used to develop a functional CCD system.
- The PFD clearly illustrates the CCD circuit and the characteristics of each stream.
- The mass balance calculations for all unit operations and the overall system verify conservation of materials.
- The conceptual thickener sizing using the Wilhelm-Naide method offers a robust and modern approach, preventing over- and under sizing.

Chapter 7: Conclusion, evaluation and recommendations

The main conclusions regarding the leaching and settling of FMO slag for the conceptual design of a CCD process are summarised in this section. Recommendations for further research are also provided.

7.1 Conclusion and evaluation

The conclusion and evaluation below are derived from the results of this study, aligned with the objectives outlined in section 1.2 of this project:

1. According to the flocculant study using flocculants and methods provided by Marlyn Laboratory, the anionic flocculant K310A at a 25 g/ton dosage was identified as the best. This flocculant and dosage achieved a high settling rate and low lixiviant turbidity without causing over-flocculation. Based on the baseline settling tests, it's clear that the settling rate decreased after leaching due to changes in slurry chemistry, particle surface charge, and particle size distribution. Adding flocculant K310A at a 25 g/ton dosage significantly improves the settling rate and reduces the final bed solid concentration.
2. The leaching study found that the acid concentration and solid-liquid ratio highly influence the efficiency of leaching FMO slag. It was concluded that leaching with 1% sulphuric acid at a solid-liquid ratio of 5 wt% provided the best balance between target metal recovery and settling performance. The leaching study also found that Mn and Li exhibited preferential dissolution, whereas Si and Al resisted dissolution, indicating the selective leaching potential of Mn and Li in FMO slag.
3. The EDX analysis of the various settling layers confirms that almost all Mn dissolves in finer particles within the particle size distribution. Larger particles show only partial dissolution of Mn. This suggests that diffusion limitations hinder the selective dissolution of Mn in FMO slag.
4. Settling under CCD conditions demonstrated that the settling performance across the three CCD stages varied considerably. All three stages exhibited reduced flocculant effectiveness and slower settling rates compared to the baseline tests, with the second stage showing the most notable decline. This decline in settling rate can be attributed to solution chemistry that hinders the flocculant's effectiveness under those conditions. Settling under CCD conditions also demonstrated the evolution of the lixiviant through the CCD stages. The lixiviants' density and pH increased as the lixiviant moved from one CCD stage to the next, indicating ongoing metal dissolution and acid consumption. The most significant rise in density and pH is observed in the third CCD stage, where fresh lixiviant contacts FMO slag washed in the two previous CCD stages.

5. The conceptual design indicates that batch laboratory-scale experiments can be used to develop a functional CCD system. The data collected from the CCD batch settling experiments enables the setup of a PFD, a conceptual mass balance, and the preliminary sizing of the thickeners. The combined washing and leaching CCD step results in an observed washing efficiency of 97.98% for manganese and 98.16% for lithium at a solid-liquid ratio of 5 wt%. An overall manganese recovery of 79.37% and lithium recovery of 64.26% are achieved, considering both leaching and washing efficiencies at 5 wt%.
6. This project investigated the settling behaviour of a ferrous metal oxide slag at various CCD stages using intermediate products to mimic the continuous nature of a CCD process, and the settling data obtained was used to design a CCD demonstration plant conceptually.

7.2 Recommendations

The following recommendations are provided for further research on FMO slag settling:

1. Investigate pre-treating FMO slag to lower the calcium, silicon, and aluminium content, which consume acid and precipitate during the CCD process.
2. Investigate the use of silica polymerisation inhibitors that disrupt the gel formation observed during leaching at acid concentrations exceeding 1% H_2SO_4.
3. Investigate the use of a coagulant such as DEHSCOFIX SC 12, produced by Innospec, to remove colloidal silica by promoting agglomeration of the particles.
4. Conduct additional research on multi-stage leaching before CCD washing to improve Mn and Li recovery without excess acid use and the dissolution of unwanted elements.
5. Conduct further research for each CCD stage to identify the most suitable flocculant type and dosage, accounting for different slurry chemistries and variations in flocculant effectiveness.
6. Repeat the process used to produce intermediate leached slag and intermediate loaded lixiviants once more to ensure the intermediate products more accurately reflect operation within a continuous system.
7. Validate the CCD performance at a demonstration scale using continuous flow to confirm assumptions derived from batch testing and refine operational parameters.
8. Use the demonstration model to monitor the recovery of the target metal and impurity levels to determine a more effective wash ratio and residence time.
9. Assess the recovery of the target metal using a CCD system with varying numbers of CCD stages, considering operational and construction costs.
10. Assess reusing the lixiviant overflow from the CCD system in the upstream leaching stage, increasing the target metal concentration within the PLS and decreasing the volume of lixiviant sent for further downstream processing.

Bibliography

[1] Y. Ghorbani, J. Franzidis and J. Petersen, “Heap leaching technology—current state, innovations, and future directions: a review,” *Mineral Processing and Extractive Metallurgy Review,* vol. 37, no. 2, pp. 73-119, 2016.

[2] A. Tripathy, S. Behera, B. Marandi, P. Sahu, A. Sheik, V. Aishvarya, I. Bhattacharya and K. Sanjay, “Towards Solving the Complexity Associated with Continuous Countercurrent Decantation (CCD) System in Solid–Liquid Separation Processes,” *Journal of The Institution of Engineers (India): Series D,* vol. 105, no. 2, pp. 1223-1229, 2024.

[3] M. Mulligan and L. Bradford, “Soluble metal recovery improvement using high density thickeners in a CCD circuit: Ruashi II case study,” *Journal of the Southern African Institute of Mining and Metallurgy,* vol. 109, no. 11, pp. 665-669, 2009.

[4] M. Nicol, Hydrometallurgy: Theory, Elsevier, 2022.

[5] J. Karageorgos, S. Davies, E. Broers and J. Goh, “Current trends in countercurrent decantation and thickener circuit operability and control.,” *In Preprints Tenth Mill Operators' Conference ,* pp. 255-260, 2009.

[6] A. Ray, Leaching. In Coulson and Richardson's Chemical Engineering, Butterworth-Heinemann, 2023, pp. 727-756.

[7] M. Fuerstenau and K. Han, Principles of mineral processing, SME, 2003.

[8] N. Piatak, M. Parsons and R. Seal II, “Characteristics and environmental aspects of slag: A review,” *Applied Geochemistry,* vol. 57, pp. 236-266, 2015.

[9] H. Van Oss, “Slag, Iron and Steel: U.S. Geological Survey,” *Minerals Yearbook,* vol. 1, p. 69.1–69.9, 2013.

[10] S. Sobanska, B. Ledésert, D. Deneele and A. Laboudigue, “Alteration in soils of slag particles resulting from lead smelting.,” *Comptes Rendus de l'Academie des Sciences-Series IIA-Earth and Planetary Science,* vol. 331, no. 4, pp. 271-278, 2000.

[11] B. Gorai and R. Jana, “Characteristics and utilisation of copper slag—a review.,” *Resources, conservation and recycling,* vol. 39, no. 4, pp. 299-313, 2003.

[12] E. Matinde and J. Steenkamp, Metallurgical overview and production of slags., 2021.

[13] H. Kokal and M. Ranade, “Metallurgical Uses—Fluxes for Metallurgy,” *Ind. Miner. Rocks,* vol. 15, pp. 661-675, 1994.

[14] T. Rosenqvist, Principles of extractive metallurgy., Tapir academic press, 2004.

[15] I. Yildirim and M. Prezzi, “Chemical, mineralogical, and morphological properties of steel slag,” *Advances in civil engineering,* vol. 2011, no. 1, p. 463638, 2011.

[16] A. Cottrell, An introduction to metallurgy, CRC Press, 2019.

[17] M. Tossavainen, F. Engstrom, Q. Yang, N. Menad, M. Larsson and B. Bjorkman, “Characteristics of steel slag under different cooling conditions,” *Waste management,* vol. 27, no. 10, pp. 1335-1344, 2007.

[18] A. Rai, J. Prabakar, C. Raju and R. Morchalle, “Metallurgical slag as a component in blended cement,” *Construction and Building Materials,* vol. 16, no. 8, pp. 489-494, 2002.

[19] D. Lewis, “Resource conservation by use of iron and steel slags,” ASTM International., 1982, pp. 31-42.

[20] B. Lim, M. Aylmore and R. Alorro, “Technospheric mining of critical and strategic metals from non-ferrous slags,” *Metals,* vol. 14, no. 7, p. 804, 2024.

[21] I. Suh, Y. Waseda and A. Yazawa, “Some interesting aspects of non-ferrous metallurgical slags,” *High Temperature Materials and Processes,* vol. 8, no. 1, pp. 65-88, 1988.

[22] K. Reddy, A. Gopakumar and J. Chetri, “Critical review of applications of iron and steel slags for carbon sequestration and environmental remediation,” *Reviews in Environmental Science and Bio/Technology,* vol. 18, no. 1, pp. 127-152, 2019.

[23] C. Gahan, M. Cunha and Å. Sandström, “Comparative study on different steel slags as neutralising agent in bioleaching,” *Hydrometallurgy,* vol. 95, no. 3-4, pp. 190-197, 2009.

[24] C. Barca, C. Gérente, D. Meyer, F. Chazarenc and Y. Andrès, “Phosphate removal from synthetic and real wastewater using steel slags produced in Europe,” *Water research,* vol. 46, no. 7, pp. 2376-2384, 2012.

[25] L. Bowden, A. Jarvis, P. Younger and K. Johnson, “Phosphorus removal from waste waters using basic oxygen steel slag,” *Environmental science & technology,* vol. 43, no. 7, pp. 2476-2481, 2009.

[26] Y. Dhoble and S. Ahmed, “Review on the innovative uses of steel slag for waste minimization,” *Journal of Material Cycles and Waste Management,* vol. 20, no. 3, pp. 1373-1382, 2018.

[27] M. Maslehuddin, A. Sharif, M. Shameem, M. Ibrahim and M. Barry, “Comparison of properties of steel slag and crushed limestone aggregate concretes,” *Construction and building materials,* vol. 17, no. 2, pp. 105-112, 2003.

[28] A. Hadjsadok, S. Kenai, L. Courard, F. Michel and J. Khatib, “Durability of mortar and concretes containing slag with low hydraulic activity,” *Cement and Concrete Composites,* vol. 34, no. 5, pp. 671-677, 2012.

[29] A. Shibayama, Y. Takasaki, T. William, A. Yamatodani, Y. Higuchi, S. Sunagawa and E. Ono, “Treatment of smelting residue for arsenic removal and recovery of copper using pyro–hydrometallurgical process,” *Journal of hazardous materials,* vol. 181, no. 1-3, pp. 1016-1023, 2010.

[30] H. Shen and E. Forssberg, “An overview of recovery of metals from slags,” *Waste management,* vol. 23, no. 10, pp. 933-949, 2003.

[31] M. Shamsuddin and TMS., Physical chemistry of metallurgical processes, Wiley, TMS, 2016.

[32] A. Mular, D. Halbe and D. Barratt, Mineral processing plant design, practice, and control: proceedings (Vol. 1)., SME, 2002.

[33] G. Stokes, “On the effect of the internal friction of fluids on the motion of pendulums,” 1851.

[34] A. Foust, L. Wenzel, C. Clump, L. Maus and L. Andersen, Principles of unit operations, John Wiley & Sons, 2008.

[35] B. Amarasinghe, Sedimentation Behaviour of Complex Polydisperse Suspension, United Kingdom: The University of Manchester, 1990.

[36] F. Concha, Solid-liquid separation in the mining industry, Springer International Publishing, 2014.

[37] J. Richardson and W. Zaki, “Sedimentation and fluidisation: Part I,” *Chemical Engineering Research and Design,* vol. 75, pp. S82-S100, 1997.

[38] J. Richardson and W. Zaki, “The sedimentation of a suspension of uniform spheres under conditions of viscous flow,” *Chemical Engineering Science,* vol. 3, no. 2, pp. 65-73, 1954.

[39] G. Kynch, “Theory of Sedimentation,” *Trans. Farady Soc.,* vol. 48, pp. 66-176, 1952.

[40] F. Concha and A. Barrientos, “A critical review of thickener design methods,” *KONA Powder and Particle Journal,* vol. 11, pp. 79-104, 1993.

[41] H. Coe and G. Clevenger, “Methods for determining the capacities of slime settling tanks,” *Transactions American Institute of Mining Engineerring,* vol. 55, pp. 356-384, 1916.

[42] M. Bustos, Sedimentation and thickening: Phenomenological foundation and mathematical theory, Springer Science & Business Media, 1999.

[43] R. Bürger, M. Bustos and F. Concha, “Settling velocities of particulate systems: 9. Phenomenological theory of sedimentation processes: numerical simulation of the transient behaviour of flocculated suspensions in an ideal batch or continuous thickener,” *International journal of mineral processing,* vol. 55, no. 4, pp. 267-282, 1999.

[44] M. Miller, “Thickener design, control and development,” Perth, Austral-ia., 2018.

[45] L. Wang and M. Maxey, “Settling velocity and concentration distribution of heavy particles in homogeneous isotropic turbulence,” *Journal of fluid mechanics,* vol. 256, pp. 27-68, 1993.

[46] W. Talmage and E. Fitch, “Determining thickener unit areas,” *Industrial & Engineering Chemistry,* vol. 47, no. 1, pp. 38-41, 1955.

[47] J. Wilhelm and Y. Naide, “Sizing and operating continuous thickeners,” 1981.

[48] N. Yoshioka, “Continuous thickening of homogeneous flocculated slurries,” *Kagaku Kogaku,* vol. 21, pp. 66-74, 1957.

[49] F. Habashi, “A short history of hydrometallurgy,” *Hydrometallurgy,* vol. 79, no. 1-2, pp. 15-22, 2005.

[50] J. Petersen and P. Staden, “Heap Leaching: Process, Principles, and Practical Considerations,” *In Treatise on Process Metallurgy,* vol. 2B, pp. 333-345, 2025.

[51] J. Petersen, “Heap leaching as a key technology for recovery of values from low-grade ores–A brief overview,” *Hydrometallurgy,* vol. 165, pp. 206-212, 2016.

[52] L. Cope, “Vat leaching: An overlooked process,” *Engineering and Mining Journal,* vol. 200, no. 12, p. 17, 1999.

[53] F. Faraji, A. Alizadeh, F. Rashchi and N. Mostoufi, “Kinetics of leaching: a review,” *Reviews in Chemical Engineering,* vol. 38, no. 2, pp. 113-148, 2022.

[54] T. Zhao, M. Traversy, Y. Choi and A. Ghahreman, “A novel process for multi-stage continuous selective leaching of lithium from industrial-grade complicated lithium-ion battery waste,” *Science of The Total Environment,* vol. 909, p. 168533, 2024.

[55] R. Ghanem, H. Farag, Y. Eltaweel and M. Ossman, “Recovery of nickel from spent catalyst by single-and multi-stage leaching process,” *International Journal of Environment and Waste Management,* vol. 2, no. 6, pp. 540-548, 2008.

[56] A. Tripathy, S. Behera, B. Marandi, P. Sahu, A. Sheik, V. Aishvarya, I. Bhattacharya and K. Sanjay, “Towards Solving the Complexity Associated with Continuous Countercurrent Decantation (CCD) System in Solid–Liquid Separation Processes,” *Journal of The Institution of Engineers (India): Series D,* pp. 1-7, 2023.

[57] M. Doble, Perry’s chemical engineers’ handbook, New York, NY, USA: McGraw-Hill, 1984.

[58] B. Wills and J. Finch, Wills' mineral processing technology: an introduction to the practical aspects of ore treatment and mineral recovery, Butterworth-heinemann, 2015.

[59] J. Gregory and C. O'Melia, “Fundamentals of flocculation,” *Critical Reviews in Environmental Science and Technology,* vol. 19, no. 3, pp. 185-230, 1989.

[60] L. Zhang, H. Wang, A. Wu, K. Yang, X. Zhang and J. Guo, “Effect of flocculant dosage on the settling properties and underflow concentration of thickener for flocculated tailing suspensions,” *Water Science & Technology,* vol. 88, no. 1, pp. 304-320, 2023.

[61] G. Parsapour, M. Hossininasab, M. Yahyaei and S. Banisi, “Effect of settling test procedure on sizing thickeners,” *Separation and Purification Technology,* vol. 122, pp. 87-95, 2014.

[62] A. Labiosa, “Dynamic simulation of red mud washers used in aluminum industries.,” 2010.

[63] F. Schoenbrunn, J. Rajala and C. McCleary, “Design and Operation of the Kupol Project Counter-Current Decantation Circuit Using Deep Cone Thickeners.,” in *Proceedings of the Twelfth International Seminar on Paste and Thickened Tailing*, 2009.

[64] L. Hudson, Alumina Production, in ed by A.R. Burkin Production of Aluminium and Alumina, Chichester: J. Wiley, 1987, p. 11–46.

[65] J. Seader, E. Henley and D. Roper, Separation Process Principles, Chemical and Biochemical Operations, 3rd edn, Hoboken: Wiley, 2011.

[66] M. Wadsworth and J. Miller, Hydrometallurgical processes. In Rate processes of extractive metallurgy, Boston, MA: Springer US., 1979, pp. 133-244.

[67] B. Ersoy, “Effect of pH and polymer charge density on settling rate and turbidity of natural stone suspensions,” *International Journal of Mineral Processing,* vol. 75, no. 3-4, pp. 207-216, 2005.

[68] T. Riba, “Liberation of ferrometal remnants from an oxide slag - breakage characteristics,” *[Unpublished],* 2024.

[69] M. Campos-M and R. Campos-C, “Applications of quartering method in soils and foods,” *Int. J. Eng. Res. Appl,* vol. 7, no. 1, pp. 35-39, 2017.

[70] J. Kitchener, Flocculation in mineral processing. In The Scientific Basis of Flocculation, Springer Netherlands: Dordrecht, 1978, pp. 283-328.

[71] A. Balasubramanian, “Size reduction by crushing method.,” *University of Mysore,* pp. 1-10, 2017.

[72] D. Foszcz, D. Krawczykowski, T. Gawenda, E. Kasińska-Pilut and W. Pawlos, “September. Analysis of process of grinding efficiency in ball and rod mills with various feed parameters.,” in *In IOP Conference Series: Materials Science and Engineering* , 2018.

[73] J. Oberteuffer, “Magnetic separation: A review of principles, devices, and applications,” *IEEE Transactions on Magnetics,* vol. 10, no. 2, pp. 223-238, 1974.

[74] S. Xie, Z. Hu, D. Lu and Y. Zhao, “Dry permanent magnetic separator: Present status and future prospects,” *Minerals ,* vol. 12, no. 10, p. 1251, 2022.

[75] K. Arab-Tehrani, A. Colteu, I. Rasoanarivo and F. Michel-Sargos, “Design a new high intensity magnetic separator with permanent magnets for industrial applications,” *International Journal of Applied Electromagnetics and Mechanics,* vol. 32, no. 4, pp. 237-248, 2010.

[76] Y. Ghorbani, J. Franzidis and J. Petersen, “Heap leaching technology—current state, innovations, and future directions: a review,” *Mineral Processing and Extractive Metallurgy Review,* vol. 37, no. 2, pp. 73-119, 2016.

[77] J. Karageorgos, S. Davies, E. Broers and J. Goh, “Current trends in countercurrent decantation and thickener circuit operability and control.,” *In Preprints Tenth Mill Operators' Conference,* pp. 255-260, 2009.

[78] A. Boateng, Rotary Kiln Petroleum Coke Calcination Process: Some Design Considerations, Boston: Butterworth Heinemann: Boateng, A.A., ed. Rotary Kilns (Second Edition), 2016.

Annexure A: Full characterisation results

Table 36: XRF results for major elements present in FMO slag

Species	**%wt. of slag** [% g species/g total]
MnO	25.35
SiO_2	24.92
Al_2O_3	23.10
CaO	8.84
MgO	4.02
Fe_2O_3	2.65
SO_3	1.59
TiO_2	1.24
K_2O	0.95
Na_2O	0.26
V_2O_5	0.06
Cr_2O_3	0.03
Sum Major Elements	93.01
Sum Trace Elements	1.06
LOI	5.55
Total	99.62

Table 37: XRF results for major elements present in FMO slag

Sample		**1**	**2**	**3**
Na2O	(wt%)	0.260	0.260	0.256
MgO	(wt%)	3.959	4.002	4.101
Al2O3	(wt%)	22.950	22.973	23.369
SiO2	(wt%)	24.630	25.152	24.975
P2O5	(wt%)	0.000	0.000	0.000
SO3	(wt%)	1.387	1.675	1.697
K2O	(wt%)	0.946	0.951	0.962
CaO	(wt%)	8.769	8.795	8.944
TiO2	(wt%)	1.239	1.252	1.243
V2O5	(wt%)	0.060	0.058	0.058
Cr2O3	(wt%)	0.035	0.033	0.034
MnO	(wt%)	25.237	25.309	25.508
Fe2O3	(wt%)	2.586	2.734	2.616
Sum Major Elements	(wt%)	92.058	93.194	93.763
Sum Trace Elements	(wt%)	1.060	1.056	1.054
LOI	(wt%)	5.580	5.540	5.540
Total	(wt%)	98.698	99.790	100.357

Table 38: XRF analysis on both the ferrous metal oxide and magnetic material present in the slag

Element (%)	Samples	
	Ferrous metal oxide	Magnetic material
AL_2O_3	23.71	3.92
CaO	25.96	4.11
Cr_2O_3	0.00	0.12
Fe_2O_3	0.60	78.34
K_2O	0.26	0.18
MgO	1.08	0.20
MnO	28.11	8.89
Na_2O	0.55	0.13
P_2O_5	0.00	0.41
SiO_2	18.75	3.51
TiO_2	0.98	0.18

Table 39: ICP-MS analysis on both the ferrous metal oxide and magnetic materials present in the slag

Element (mg/kg)	Sample	
	Ferrous metal oxide	Magnetic material
Na	2983.81	1089.54
Mg	6582.29	1974.44
P	33.37	423.32
K	4436.44	2058.66
Ca	180217.49	66571.03
Al	117818.0	44617.2
Mn	211521.5	146971.3
Fe	3188.0	564717.6
Si	2711.8	1248.4
Element (ug/kg)	Sample	
	Ferrous metal oxide	Magnetic material
B	139214.7	41688.6
V	124466.3	312186.6
Cr	132430.2	1025019.3
Co	0.0	199737.0
Ni	4168.8	704030.1
Cu	3550.4	223161.5
Zn	7193.7	34371.5
As	2670.9	35652.4
Se	219.2	130.6
Sr	1117223.1	566978.2
Mo	49.7	6425.9
Cd	30.0	19.3
Sn	118.1	5937.1
Sb	20.5	4284.4
Ba	11121674.3	5308931.6

Hg	4.6	14.2
Pb	2803.7	13773.1
Sc	41716.4	17789.0
Y	92823.3	39106.2
La	103057.1	44474.9
Ce	229042.8	96626.9
Pr	27935.0	11692.6
Nd	104717.2	44729.6
Sm	21180.4	8926.9
Eu	4563.8	1969.9
Gd	20512.6	8705.4
Tb	3075.0	1303.7
Dy	18478.4	7748.1
Ho	3681.0	1533.5
Er	10831.6	4478.1
Tm	1500.1	609.6
Yb	9456.1	3920.0
Lu	1476.5	605.9
Th	21495.0	8578.7
U	5548.7	2287.2

Annexure B: Equipment

Equipment	Photo
Osborn Coalequip Engineering (Pty) Ltd 425 rpm jaw crusher	
Rod mill	
Riffler	

Laboratory scale	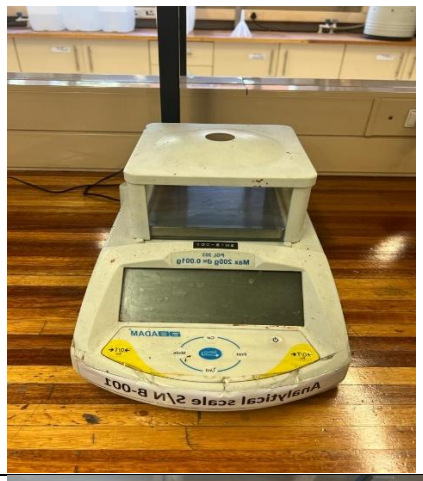
Backlight	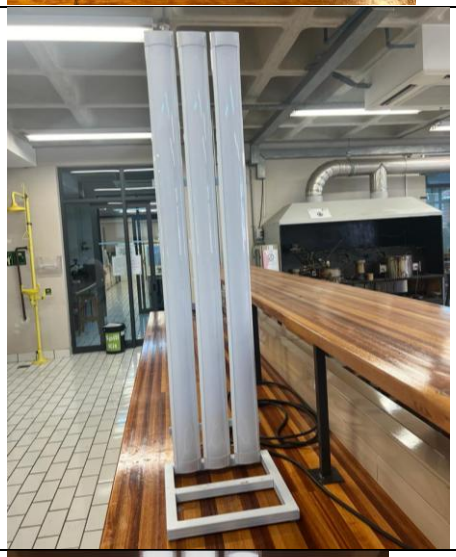
Sedimentation tubes	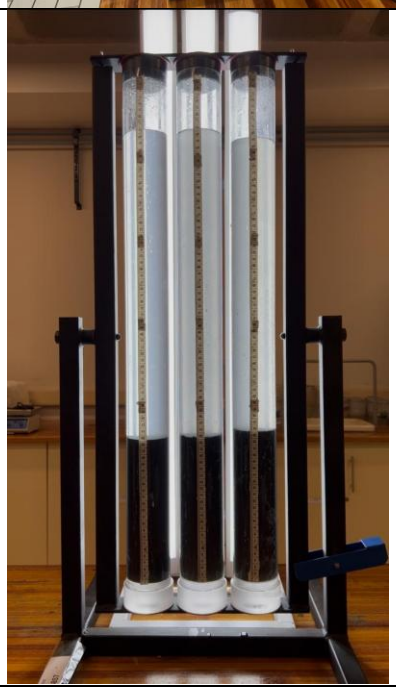

Vacuum flask		
HANNA HI5521 pH meter		
HATCH 2100Q portable turbidimeter		
EcoTherm Labotec Oven		

Annexure C: Complete results

C.1 Lixiviant pH measurements

Table 40: Intermediate lixiviant, final lixiviant and pregnant leach solution pH measurements for two 10 wt% and one 5 wt% CCD experiment

	pH		
Lixiviant	10 wt% (1)	10 wt% (2)	5 wt%
Lix'[1]	3,56	3,85	1,84
Lix'[2]	3,64	3,94	3,52
Lix'[3]	4,02	4,15	3,65
Lix[2]'	3,69	3,88	3,48
Lix[1]'	3,5	3,72	3,57
Lix[3]	4,06	4,29	3,76
Lix[2]	3,71	3,88	3,62
Lix[1]	3,5	3,65	3,56
Lix[0]	1,04	1,08	1,2
PLS[1]	5,46	4,95	3,94
PLS[2]	5,63	5,79	4,58
PLS[3]	5,58	5,77	4,56

C.2 CCD settling at solid-liquid ratio of 10 wt% second run

C.2.1 Settling

The height-time profile of the three CCD stages tested by mixing and settling intermediate lixiviants and FMO slag samples is displayed in Figure 47. The corresponding flux-concentration plots of the first, second and third CCD stages are shown in Figure 48, Figure 49 and Figure 50, respectively. Each flux-concentration plot is constructed using data gathered from the height-time profiles and fitted with a model.

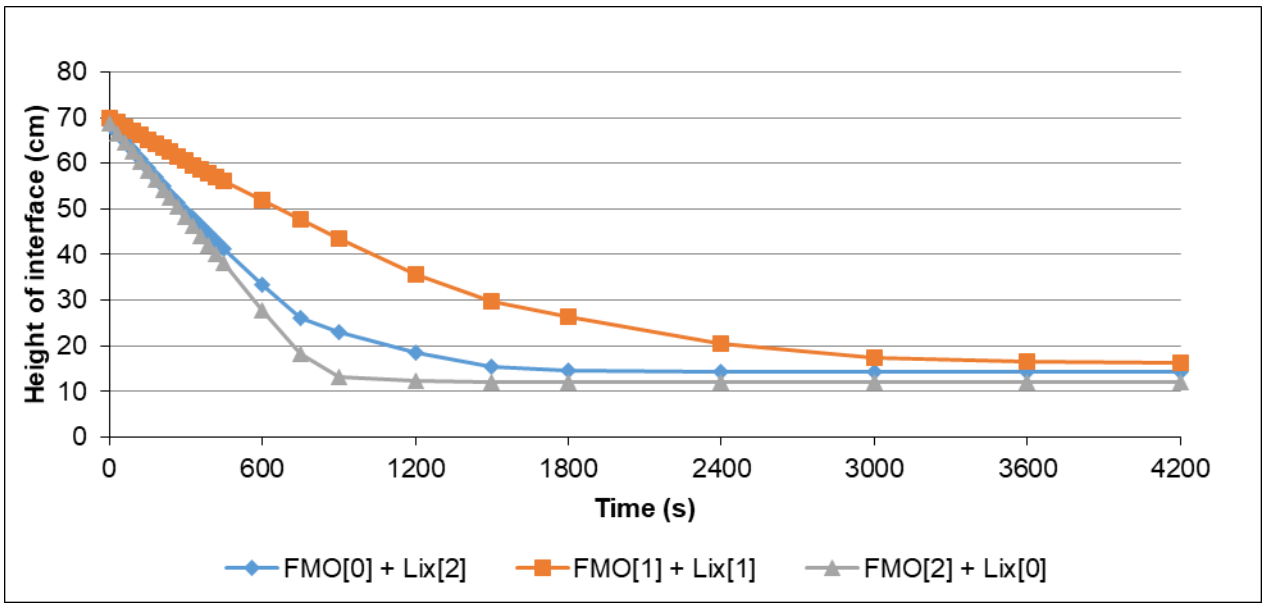

Figure 47: Height-time profile for the three stages of a CCD system for the second run at 10 wt%

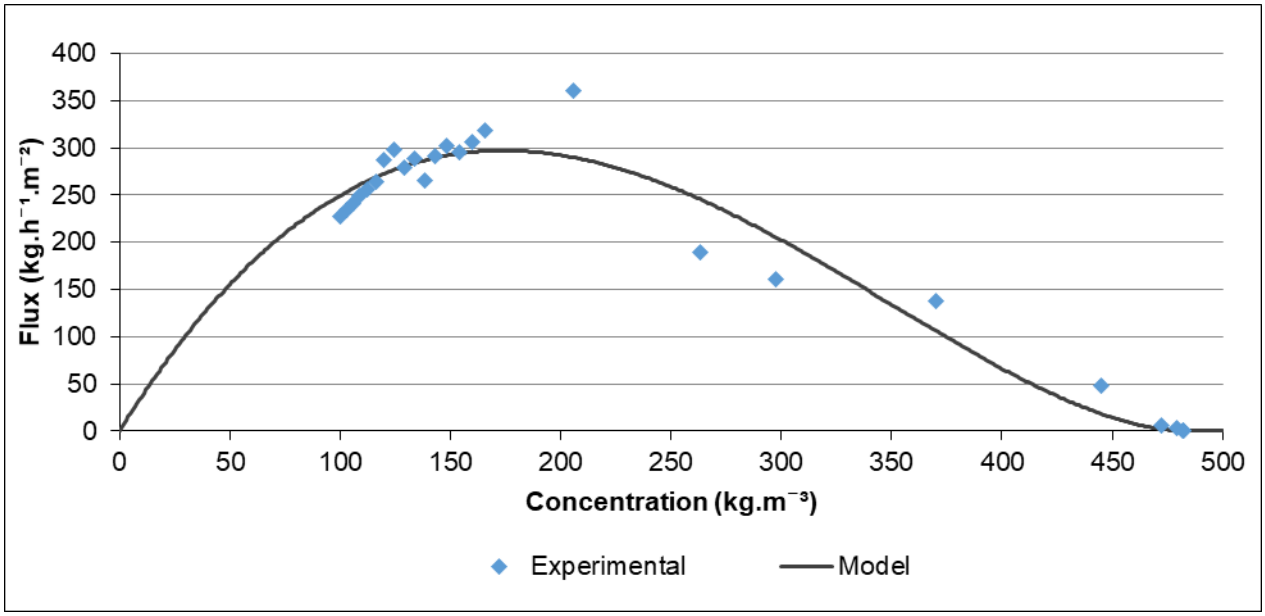

Figure 48: Flux-concentration plot for the first settling stage of a CCD system using intermediate products FMO[0] and Lix[2], for the second run at 10 wt%: Model and experimental data

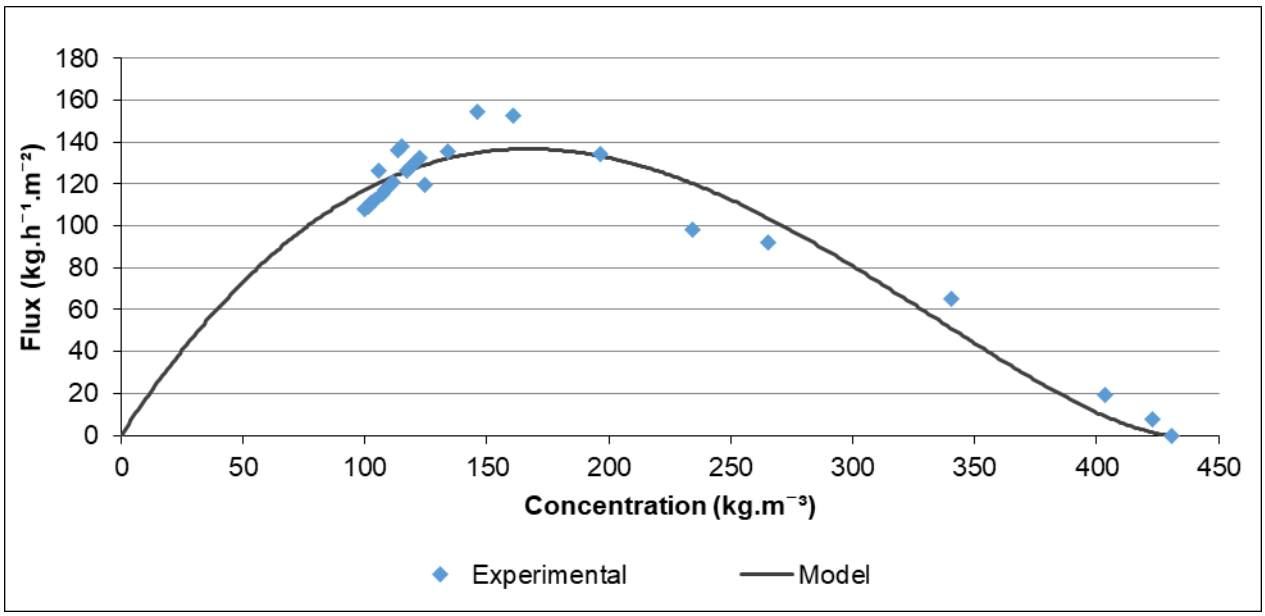

Figure 49: Flux-concentration plot for the second settling stage of a CCD system using intermediate products FMO[1] and Lix[1], for the second run at 10 wt%: Model and experimental data

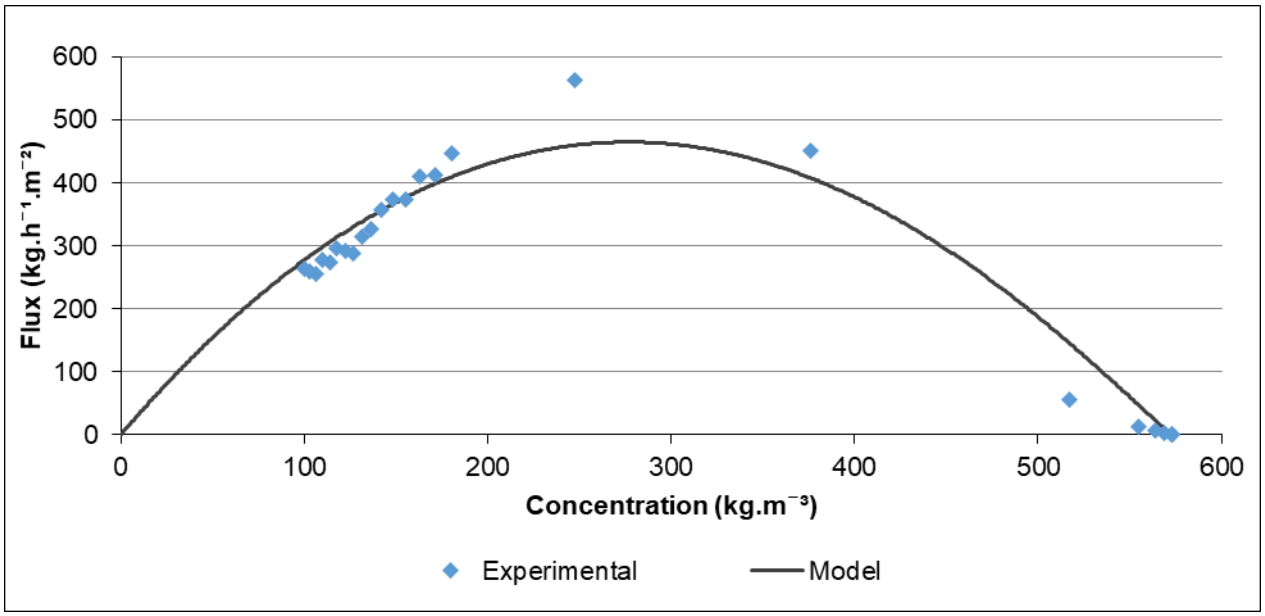

Figure 50: Flux-concentration plot for the third settling stage of a CCD system using intermediate products FMO[2] and Lix[0], for the second run at 10 wt%: Model and experimental data

Table 41: Model constants for the three CCD stages for the second run at 10 wt%

CCD stage	1	2	3
K	1817,51	767,36	1954,31
m	1,76	1,58	1,07

C.2.2 Lixiviant and slurry analysis

A lixiviant sample was taken before and after the three settling stages. Each sample represents a different stage of the CCD system. All samples were analysed for turbidity, viscosity, density, and pH. The physicochemical properties of the lixiviants are summarised in Table 42. Slag samples were also collected at three stages: one before the leaching stage, another after the leaching stage, and the final after the CCD stage. Each slag sample was analysed for PSD and density. The PSD and density results summary is presented in Table 43, and the PSD is shown in Figure 51.

Table 42: Physicochemical properties of lixiviant from settling test in the second run at 10 wt%

Lixiviant	Turbidity (FTU)	Viscosity (mPa.s)	Density (g/cm^3)	pH
Lix[3]	17.6	0.9137	1.0097	4.29
Lix[2]	137	0.8945	1.0074	3.88
Lix[1]	466	0.9529	1.0070	3.65
Lix[0]	-	0.8997	1.0016	1.08

Table 43: PSD and density of FMO slag at different stages of the settling and leaching process in the second run at 10 wt%

Solid sample	PSD			Density
	Dv(10) (µm)	Dv(50) (µm)	Dv(90) (µm)	(g/cm^3)
Slag	8.5	52	123	3.2895
FMO[0]	12.7	51.1	125	3.0017
FMO[1]	15.1	52.7	127	2.9910
FMO[2]	13.7	49.2	124	2.9414
FMO[3]	12.5	49.9	121	2.9396

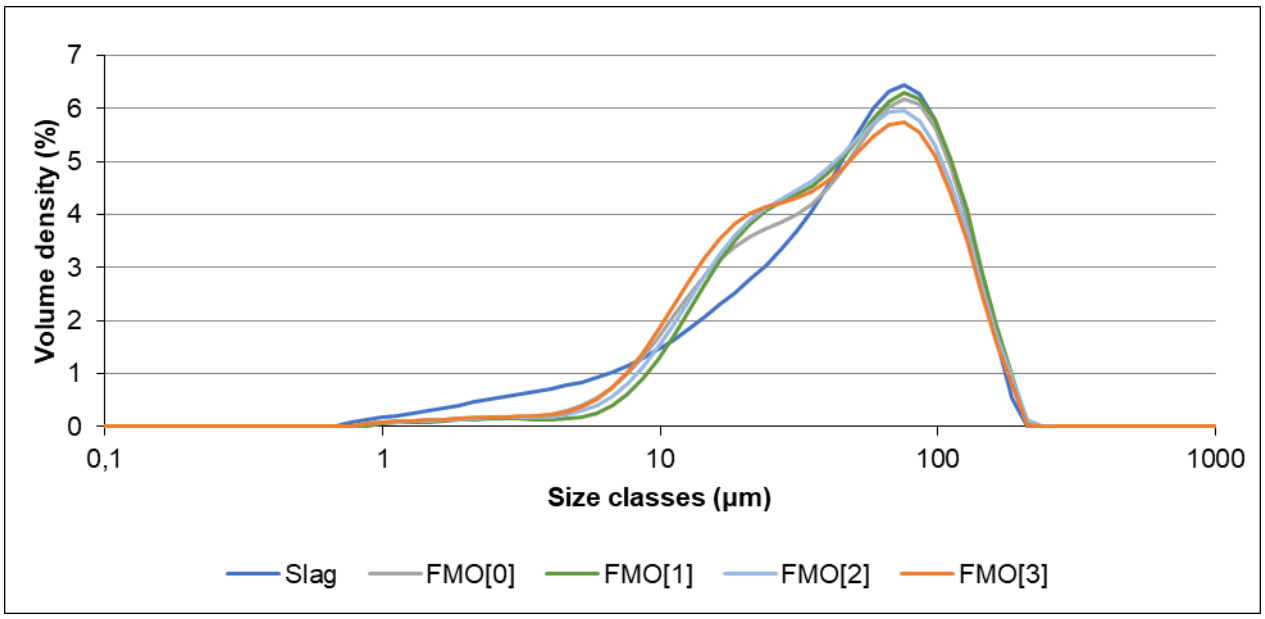

Figure 51: PSD of FMO slag at different stages of the settling and leaching process in the second run at 10 wt%

C.2.3 Leaching

Similarly, to the first 10 wt% solid-liquid experiment, the intermediate and final lixiviant samples were also sent for ICP-OES analysis to determine recovery of major elements during the leaching and CCD stages. The ICP-OES analysis measured the elemental concentration in each lixiviant sample and enabled the calculation of the total recovery of each component. The percentage and mass dissolution achieved in the leaching stage and CCD stage are summarised in Table 44.

Table 44: Dissolution of element in the leaching and CCD stage for the second run at 10 wt%

	Mn		Si		Al	
Stage	Mass dissolved (mg)	Dissolution (%)	Mass dissolved (mg)	Dissolution (%)	Mass dissolved (mg)	Dissolution (%)
Leach	10658,2	33,08%	1213,2	2,96%	118,5	0,64%
CCD1	323,5	1,00%	-468,1	-1,14%	-269,1	-1,46%
CCD2	317,7	0,99%	-213,5	-0,52%	-125,2	-0,68%
CCD3	575,1	1,78%	1283,1	3,13%	864,0	4,69%
CCD total	1216,3	3,77%	601,5	1,47%	469,8	2,55%
Total	11874,4	36,85%	1814,7	4,42%	588,3	3,19%
	Ca		**Fe**		**Li**	
Stage	Mass dissolved (mg)	Dissolution (%)	Mass dissolved (mg)	Dissolution (%)	Mass dissolved (mg)	Dissolution (%)
Leach	1156,4	7,53%	124,6	3,53%	180,7	29,66%
CCD1	-81,7	-0,53%	13,0	0,37%	-0,7	-0,11%
CCD2	61,8	0,40%	38,1	1,08%	2,7	0,45%
CCD3	875,9	5,70%	222,1	6,30%	6,1	1,00%
CCD total	856,0	5,57%	273,2	7,75%	8,2	1,34%
Total	2012,4	13,10%	397,8	11,28%	188,9	31,01%
	Mg		**K**		**Na**	
Stage	Mass dissolved (mg)	Dissolution (%)	Mass dissolved (mg)	Dissolution (%)	Mass dissolved (mg)	Dissolution (%)
Leach	588,1	14,65%	300,4	18,44%	231,7	13,54%
CCD1	0,9	0,02%	31,3	1,92%	-0,2	-0,01%
CCD2	7,7	0,19%	38,6	2,37%	1,4	0,08%
CCD3	28,5	0,71%	-29,6	-1,81%	11,0	0,64%
CCD total	37,1	0,92%	40,3	2,48%	12,2	0,71%
Total	625,2	15,58%	340,7	20,92%	243,9	14,25%

**Dissolution (%) = Amount of element dissolved / Amount of element present in sample*

C.2.4 Comparison between the first and second run at 10 wt%

In this section, the results obtained in each of the 10 wt% experiments are compared to determine the repeatability of the experiment.

C.2.4.1 Settling

Table 45: Settling comparison of the two CCD runs at 10 wt%

Stage	First run at 10 wt%			Second run at 10 wt%		
	Settling velocity (m/h)	Maximum flux ($kg/h/m^2$)	Final bed concentration (kg/m^3)	Settling velocity (m/h)	Maximum flux ($kg/h/m^2$)	Final bed concentration (kg/m^3)
FMO[0] + Lix[2]	2,23	301,9	483,8	2,28	291,8	482,4
FMO[1] + Lix[1]	0,96	109,6	367,7	1,1	136,7	430,9
FMO[2] + Lix[0]	2,52	392,2	460,3	2,45	465,1	573,3

C.2.4.2 Lixiviant and slurry analysis

Table 46: Lixiviant comparison of the two CCD runs at 10 wt%

Lixiviant	First run at 10 wt%				Second run at 10 wt%			
	Turbidity (FTU)	Viscosity (mPa.s)	Density (g/cm^3)	pH	Turbidity (FTU)	Viscosity (mPa.s)	Density (g/cm^3)	pH
Lix[3]	33,4	0,9134	1,0094	4,06	17,6	0,913672	1,00972	4,29
Lix[2]	53	0,8919	1,0066	3,71	137	0,894481	1,0074	3,88
Lix[1]	121	0,9635	1,0061	3,5	466	0,952937	1,00696	3,65
Lix[0]	-	0,8919	0,9992	1,04	-	0,899716	1,0016	1,08

Table 47: Slurry comparison of the two CCD runs at 10 wt%

Solid sample	First run at 10 wt%				Second run at 10 wt%			
	Dv(10)	Dv(50)	Dv(90)	Density (g/cm^3)	Dv(10)	Dv(50)	Dv(90)	Density (g/cm^3)
Slag	8,5	52	123	3,2895	8,48	52	123	3,2895
FMO(0)	13,2	50,5	124	2,9997	12,7	51,1	125	3,0017
FMO(3)	12,1	49,9	125	2,9347	12,5	46,3	121	2,9396

C.2.4.3 Leaching

Table 48: Leaching comparison of the two CCD runs at 10 wt%

Stage	First run at 10 wt% dissolution (%)					Second run at 10 wt% dissolution (%)				
	Mn	Si	Al	Ca	Li	Mn	Si	Al	Ca	Li
Leach	33,47%	3,38%	0,66%	7,47%	29,34%	33,08%	2,96%	0,64%	7,53%	29,66%
CCD1	0,81%	-1,18%	-1,46%	-0,12%	-0,12%	1,00%	-1,14%	-1,46%	-0,53%	-0,11%
CCD2	1,00%	-1,05%	-1,33%	0,08%	0,29%	0,99%	-0,52%	-0,68%	0,40%	0,45%
CCD3	1,81%	3,48%	4,63%	5,48%	1,11%	1,78%	3,13%	4,69%	5,70%	1,00%
CCD total	3,62%	1,25%	1,84%	5,44%	1,28%	3,77%	1,47%	2,55%	5,57%	1,34%
Total	37,09%	4,63%	2,49%	12,92%	30,62%	36,85%	4,42%	3,19%	13,10%	31,01%

C.2.4.3 Repeatability conclusion

These minor differences fall within the expected range of experimental variation for this type of experiment.

C.3 Process flow diagram of CCD experiments

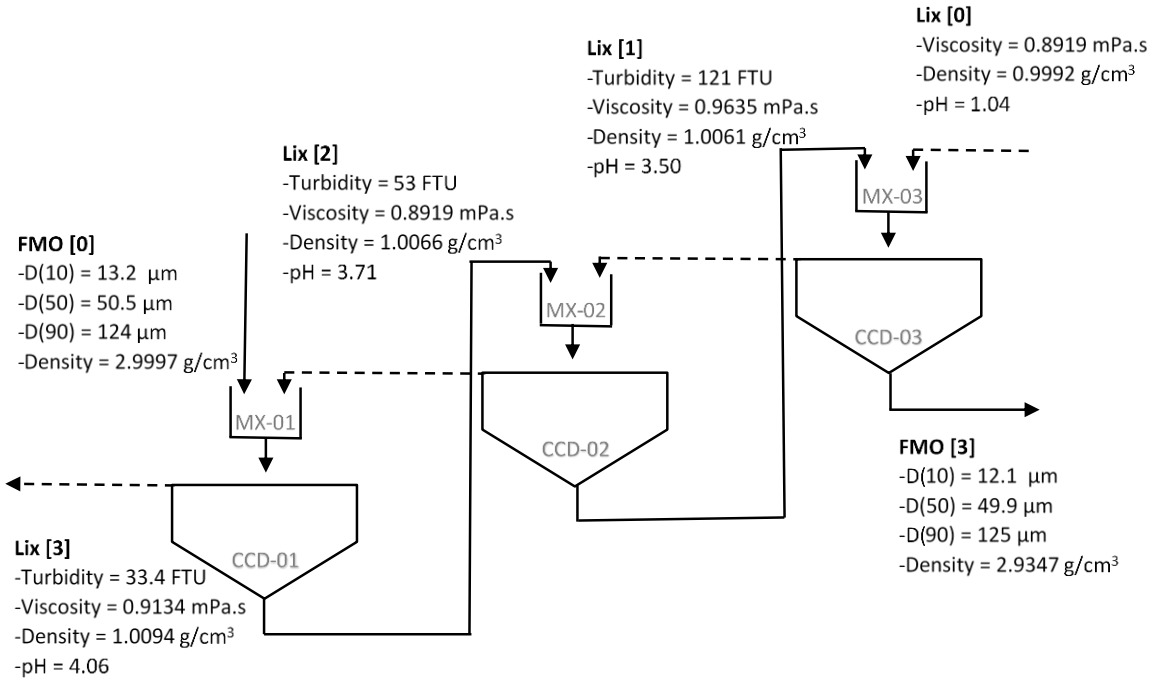

Figure 52: Process flow diagram of the first CCD experiment at 10 wt% solid-liquid ratio

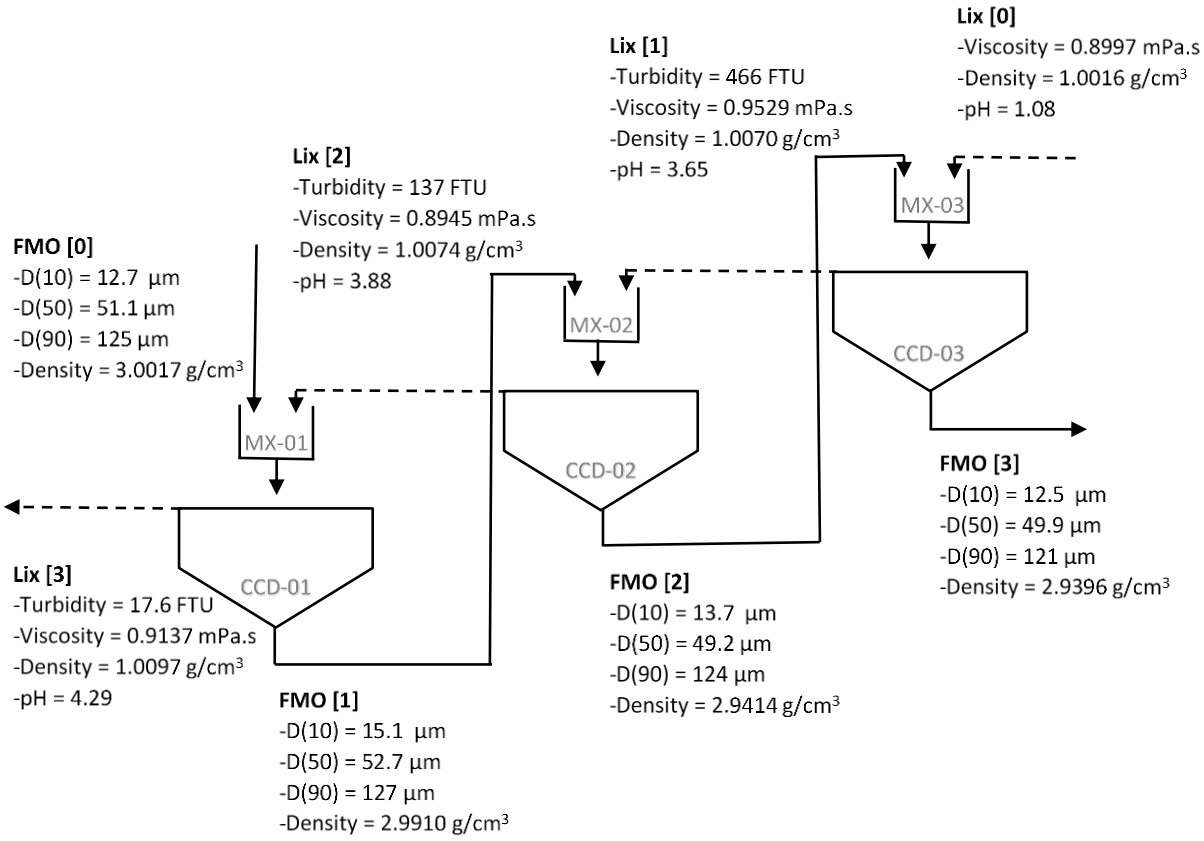

Figure 53: Process flow diagram of the second CCD experiment at 10 wt% solid-liquid ratio

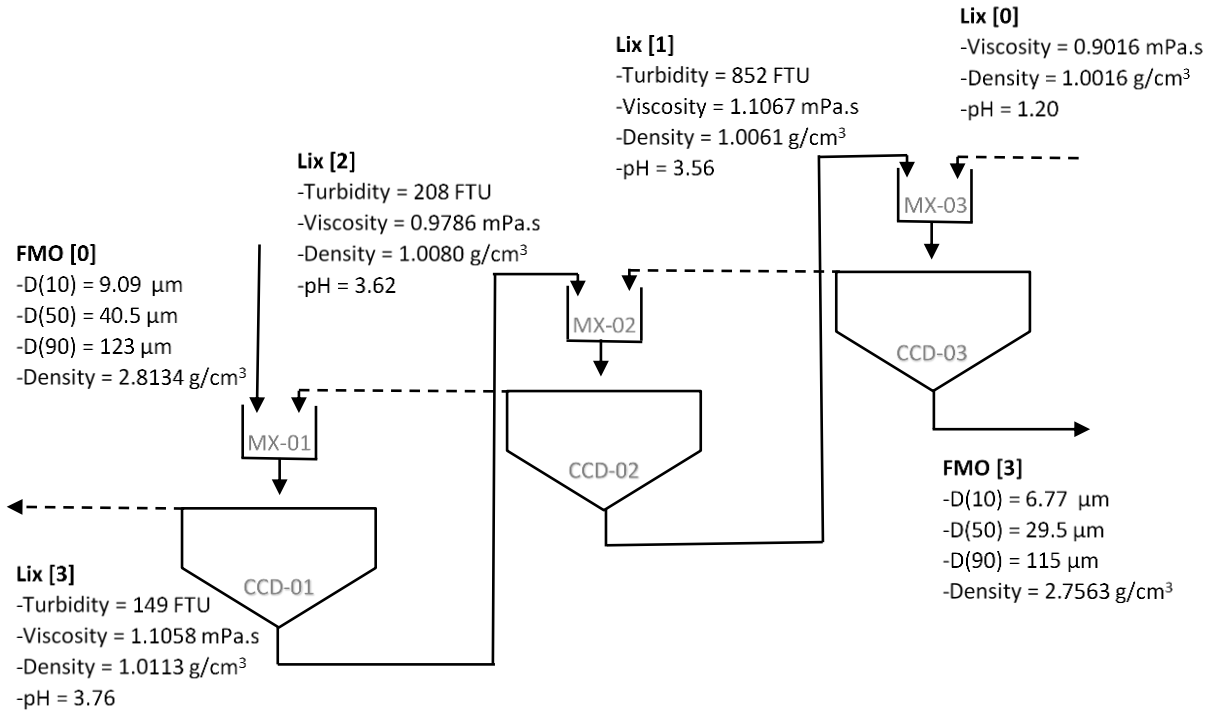

Figure 54: Process flow diagram of the CCD experiment at 5 wt% solid-liquid ratio

C.4 Thickener size calculations

C.4.1 Oltman and Bi-section method

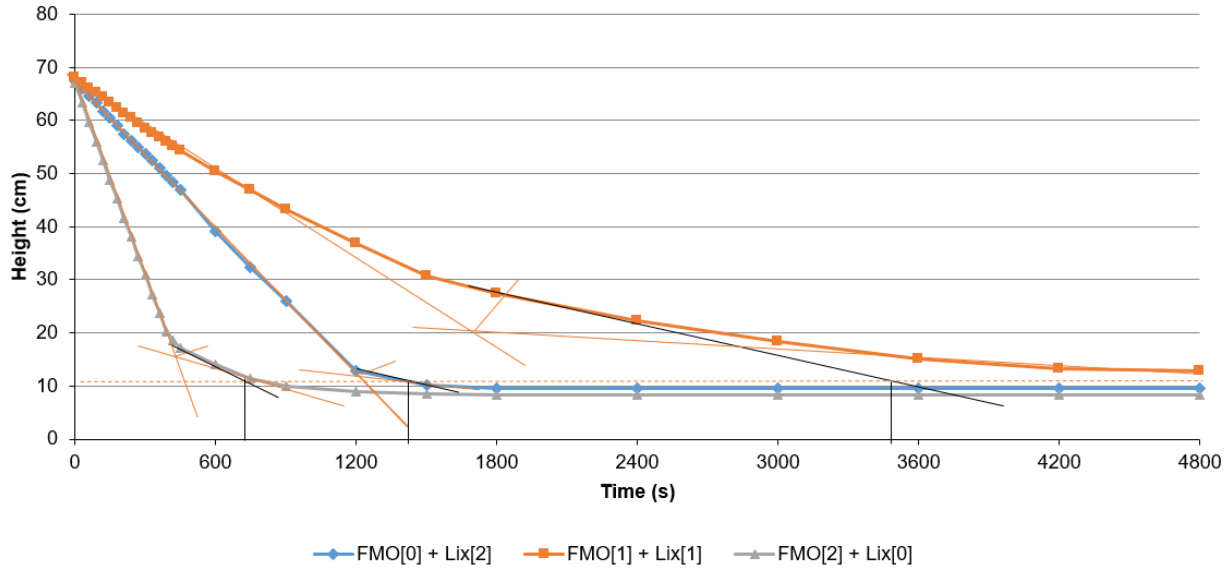

Figure 55: Oltman and Bi-section method construction of height vs time curve

From the graph, t_u is determined:

Table 49: Settling time determined from Oltman and Bi-section construction converted to days

	t_u (d)			
	Pre-thickener	CCD 1	CCD 2	CCD 3
Bi-section	0,004282	0,016204	0,040509	0,008333
Oltman	0,002431	0,013889	0,020833	0,004861

$$A = \frac{t_u}{C_0 H_0} \tag{8}$$

Where:

C_0 = 0.05 ton/m^3

H_0 = 0.68 m

Feed rate = 100 kg/h

Table 50: Unit areas calculated for Oltman and Bi-section methods

	Unit area (m^2/tpd)			
	Pre-thickener	CCD 1	CCD 2	CCD 3
Bi-section	0,126	0,477	1,191	0,245
Oltman	0,071	0,408	0,613	0,143

Table 51: Areas calculated for Oltman and Bi-section methods

	Area (m2)			
	Pre-thickener	CCD 1	CCD 2	CCD 3
Bi-section	0,302	1,144	2,859	0,588
Oltman	0,172	0,980	1,471	0,343

Table 52: Thickener diameters calculated for Oltman and Bi-section methods

	Diameter (m)			
	Pre-thickener	CCD 1	CCD 2	CCD 3
Bi-section	0,62	1,21	1,91	0,87
Oltman	0,47	1,12	1,37	0,66

C.4.2 Wilhelm-Naide method

$$A = \frac{(\frac{b-1}{b})^{b-1}}{ab} C_u^{b-1} \quad (9)$$

$$v = aC_0^{-b} \quad (10)$$

Table 53: Pre-thickener data for Wilhelm-Naide method

C (kg/m³)	F (kg/h/m²)	v (m/h)	log(ci)	log(v)
50,00	414,00	8,28	1,70	0,92
51,76	409,97	7,92	1,71	0,90
53,57	462,86	8,64	1,73	0,94
55,69	461,14	8,28	1,75	0,92
62,85	588,27	9,36	1,80	0,97
73,53	670,59	9,12	1,87	0,96
88,12	666,19	7,56	1,95	0,88
105,47	923,91	8,76	2,02	0,94
136,64	918,22	6,72	2,14	0,83
176,70	445,29	2,52	2,25	0,40
198,53	262,06	1,32	2,30	0,12
212,26	254,72	1,20	2,33	0,08
226,51	244,63	1,08	2,36	0,03
241,07	173,57	0,72	2,38	-0,14
251,87	151,12	0,60	2,40	-0,22
261,63	94,19	0,36	2,42	-0,44
267,86	64,29	0,24	2,43	-0,62
272,18	58,79	0,22	2,43	-0,67
293,48	28,17	0,10	2,47	-1,02
304,05	14,59	0,05	2,48	-1,32
309,63	3,72	0,01	2,49	-1,92

Table 54: CCD1 data for Wilhelm-Naide method

C (kg/m^3)	F ($kg/h/m^2$)	v (m/h)	log(ci)	log(v)
49,27	88,69	1,80	1,69	0,26
50,37	78,58	1,56	1,70	0,19
51,37	86,30	1,68	1,71	0,23
52,49	94,48	1,80	1,72	0,26
53,74	83,84	1,56	1,73	0,19
54,88	98,78	1,80	1,74	0,26
56,25	101,25	1,80	1,75	0,26
57,69	90,00	1,56	1,76	0,19
59,00	84,97	1,44	1,77	0,16
60,27	86,79	1,44	1,78	0,16
61,59	103,47	1,68	1,79	0,23
63,20	98,60	1,56	1,80	0,19
64,78	116,60	1,80	1,81	0,26
66,70	96,05	1,44	1,82	0,16
68,32	122,98	1,80	1,83	0,26
70,46	131,90	1,87	1,85	0,27
84,16	135,34	1,61	1,93	0,21
101,05	155,21	1,54	2,00	0,19
125,00	196,50	1,57	2,10	0,20
242,81	78,67	0,32	2,39	-0,49
301,34	21,70	0,07	2,48	-1,14
318,40	1,91	0,01	2,50	-2,22

Table 55: CCD2 data for Wilhelm-Naide method

C (kg/m^3)	F ($kg/h/m^2$)	v (m/h)	log(ci)	log(v)
50,00	60,00	1,20	1,70	0,08
50,73	54,78	1,08	1,71	0,03
51,40	55,51	1,08	1,71	0,03
52,09	56,26	1,08	1,72	0,03
52,80	63,36	1,20	1,72	0,08
53,61	57,90	1,08	1,73	0,03
54,36	65,23	1,20	1,74	0,08
55,22	59,64	1,08	1,74	0,03
56,02	67,22	1,20	1,75	0,08
56,93	68,32	1,20	1,76	0,08
57,88	62,51	1,08	1,76	0,03
58,75	56,40	0,96	1,77	-0,02
59,56	64,32	1,08	1,77	0,03
60,49	58,07	0,96	1,78	-0,02
61,34	51,52	0,84	1,79	-0,08
62,10	58,13	0,94	1,79	-0,03
66,73	57,66	0,86	1,82	-0,06
71,66	63,64	0,89	1,86	-0,05
77,56	58,63	0,76	1,89	-0,12
90,18	67,09	0,74	1,96	-0,13
107,38	41,24	0,38	2,03	-0,42
119,11	37,16	0,31	2,08	-0,51
144,81	33,89	0,23	2,16	-0,63
172,77	33,17	0,19	2,24	-0,72
205,29	23,40	0,11	2,31	-0,94
231,13	6,93	0,03	2,36	-1,52

Table 56: CCD3 data for Wilhelm-Naide method

C (kg/m^3)	F ($kg/h/m^2$)	v (m/h)	log(ci)	log(v)
50,00	222,00	4,44	1,70	0,65
52,84	234,62	4,44	1,72	0,65
56,03	242,03	4,32	1,75	0,64
59,52	257,11	4,32	1,77	0,64
63,47	274,18	4,32	1,80	0,64
67,98	293,69	4,32	1,83	0,64
73,19	307,40	4,20	1,86	0,62
79,08	341,63	4,32	1,90	0,64
86,22	382,80	4,44	1,94	0,65
95,03	399,12	4,20	1,98	0,62
105,20	454,46	4,32	2,02	0,64
118,21	510,68	4,32	2,07	0,64
134,90	566,59	4,20	2,13	0,62
156,36	300,22	1,92	2,19	0,28
168,63	283,29	1,68	2,23	0,23
181,05	139,05	0,77	2,26	-0,11
217,72	135,86	0,62	2,34	-0,20
260,61	87,56	0,34	2,42	-0,47
291,53	38,48	0,13	2,46	-0,88
321,50	15,43	0,05	2,51	-1,32
333,98	8,02	0,02	2,52	-1,62

Table 57: Diameter of thickener calculation using the Wilhelm-Naide method

	Pre-thickener	CCD 1	CCD 2	CCD 3
a	334811	7019	2111	68733
b	2,500	2,025	1,872	2,244
UA	0,004	0,012	0,017	0,004
A (m^2)	0,373	1,235	1,703	0,434
D (m)	0,689	1,254	1,472	0,744